Mean-field theory in magneto-hydrodynamics and the generation of magnetic flux concentrations

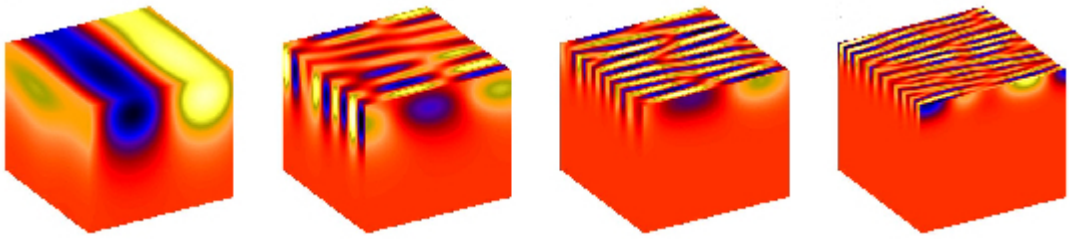

Koen Kemel
Nordita, Stockholm, Sweden
Department of Astronomy, Stockholm University, Sweden

Title page picture: magnetic structure formation by NEMPI for different values of q_s.

Department of Astronomy **Nordita**

Mean-field theory in magneto-hydrodynamics and the generation of magnetic flux concentrations

Licentiate Thesis

Koen Kemel

August 16, 2011

First Supervisor
Axel Brandenburg

Second Supervisor
Göran Scharmer

Mentor
Dhrubaditya Mithra

Abstract

The generally accepted view that a sunspot originates from a flux tube, emerging through the solar photosphere, after travelling coherently across the underlying convection zone, is being challenged. While the properties of an emerging flux tube appear to reproduce the observations, it is not clear if other mechanisms are possible as well. Furthermore, questions remain about the formation and coherent rise of such structures,which are currently strongly debated.

One of the objectives of the present work is to verify that it is possible to create coherent magnetic structures starting from a homogeneous background. The driving idea is to understand if and under what set of conditions, sunspots can form as near surface phenomena, as opposed to rising tachoclinic magnetic flux tubes.

In direct numerical simulations we found a reduction of the effective turbulent pressure in the presence of magnetic fields and stratification, as anticipated by earlier analytical calculations. A subsequent mean-field analysis incorporating this reduction suggests that this setup can become unstable and form magnetic flux concentrations under certain conditions.

Mean-field models are however degenerate in the sense that different closure models can be used, possibly giving different results. In the case above, the effect of turbulence was captured by modelling the Reynolds stress tensor. Rather than looking for higher order closure, one can also determine coefficients in a closure model from experiments or simulations. The test-field method is an example of the latter and has been successfully used for modelling the electromotive force in dynamo problems.

Closure models are approximations within a certain parameter regime (for example only for low magnetic Reynolds number) and as such suffer from a loss in generality. In this context we also investigate the validity of the astrophysical dynamo description for conditions more relevant to laboratory experiments, such as the reversed field pinch in plasma confinement experiments.

List of papers included in the thesis

I **Effect of stratified turbulence on magnetic flux concentrations**
Brandenburg, A., Kemel, K., Kleeorin, N., and Rogachevskii, I.
ApJ, submitted, May 2010 - second revision May 2011
arXiv:1005.5700

II **Properties of the negative effective magnetic pressure instability**
Kemel, K., Brandenburg, A., Kleeorin, N., and Rogachevskii, I.
A.N., submitted, July 2011
arXiv:1107.2752

III **Turbulent transport in stratified and/or rotating turbulence**
Brandenburg, A., Rädler, K.-H., and Kemel, K.
A&A, submitted, August 2011
arXiv:1108.2264

IV **A model of driven and decaying magnetic turbulence in a cylinder**
Kemel, K., Brandenburg, A., and Hantao, J.
Phys. Rev. E, submitted, June 2011
arXiv:1106.1129

Conference proceedings not included in the thesis

V **The negative magnetic pressure effect in stratified turbulence**
Kemel, K., Brandenburg, A., Kleeorin, N. and Rogachevskii, I.
submitted for conference proceedings IAU symposium 273 "Physics of Sun and Star Spots"
arXiv:1010.1659

VI **Turbulent magnetic pressure instability in stratified turbulence**
Kemel, K., Brandenburg, A., Kleeorin, N. and Rogachevskii, I.
Advances in Plasma Astrophysics, Proceedings of the International Astronomical Union, IAU Symposium, Volume 274, p. 473-475

Summary of the papers

Paper I introduces the physics behind the reduction of the effective turbulent pressure in the presence of a magnetic field. This paper gives results of the first stratified simulations and confirms that the pressure reduction effect works even if there is small-scale dynamo action.

Associated mean-field models show the formation of structures by an instability that is investigated in more detail in Paper II, where it is referred to as the negative effective magnetic pressure instability. Here it is shown that the break-up of the eigenmode into three-dimensional structures with variation along the direction of the mean field is only possible when there is also a negative effective tension force, although our direct simulations have show that the corresponding effect should be absent.

In Paper I, the test-field method was applied to determine the effect of turbulent pumping down the gradient of turbulent intensity. It was also shown that such pumping is absent if there is just density stratification. To investigate more rigorously turbulent transport in a stratified layer, we develop in Paper III a new test-field method for inhomogeneous and anisotropic turbulence in the presence of just one preferred direction. In that case, new effects emerge that are connected with the symmetric part of the gradient matrix of the mean magnetic field.

To examine whether mean-field effects can also be studied in laboratory experiments, we apply in Paper IV mean-field dynamo theory to a cylindrical geometry and determine the magnetic field evolution in the case where an axial magnetic field is applied together with an axial electric field. The mean field is essentially determined by the same feedback mechanism that would quench dynamo action in the astrophysical case of self-excited dynamos.

Contents

Chapter 1

Introduction

Our solar system's central star has long been a daily observed enigma. Since Galilei opened Pandora's box about 400 years ago with his publications on sunspot observations, a number of the Sun's mysteries have been cleared up, yet new ones emerge and plenty remain. One of them is the origin of those very sunspots.

The study of solar activity is not purely of academic interest. While short term space weather predictions are a faraway dream, improving our understanding of the long term solar cycle will support planning of space research activity and missions. More down to earth, effects of solar activity are related to magnetic storms interfering with power grids in polar regions and intercontinental aviation (high altitude, polar routes). There may also be effects on the Earthly climate due a correlation between solar activity and magnetic shielding of cosmic rays.

Sunspot observations and terrestrial tracers of solar activity contain our main longterm data source on the solar cycle. They play a key role in our current efforts to understand the physics of the Sun over extended temporal spans. And vice versa, numerical realisation of sunspot-like structures requires insight into the physical conditions inside the Sun.

1.1 Looking at sunspots

The first telescopes permitted early 17th century scientists a more detailed inspection of the celestial bodies. While Galileo Galilei was not the first person to notice sunspots, see Figure 1.1, he was the one who confronted the western world and its dogmatic Aristotelic world view (perfect spheres in circular orbit around the earth) with their existence. As their motions did not stroke with ellipsoid trajectories around the sun, Galilei reasoned that they might be the equivalent of terrestrial clouds on the solar surface. In his drawings he categorised the observed spots by shape.

As the Maunder minimum (1645-1715) literally offered very little to see (Eddy, 1976), most astronomers let their attention wander to other directions of the skies. Interest was regained half way into the 19th century, when Schwabe, in 1843, after an 18 year search for a planet closer to the sun than Mercury, noticed the cyclic behaviour ('a period of about 10 years') of the number of sunspots (Schwabe, 1844). Under an uninteresting title, this discovery kept went almost unnoticed until its publication in Kosmos by von Humboldt (1851). This sparked a new wave of that resulted in a large quest for phenomena with the same frequency, ranging from geophysical and atmospherical cycles to somewhat dubious demological trends (Westwood Oliver, 1883). In the wake of enthusiasm after this discovery, Carrington (1858) noticed and Spörer (1883) defined an equatorial migration of the sunspots

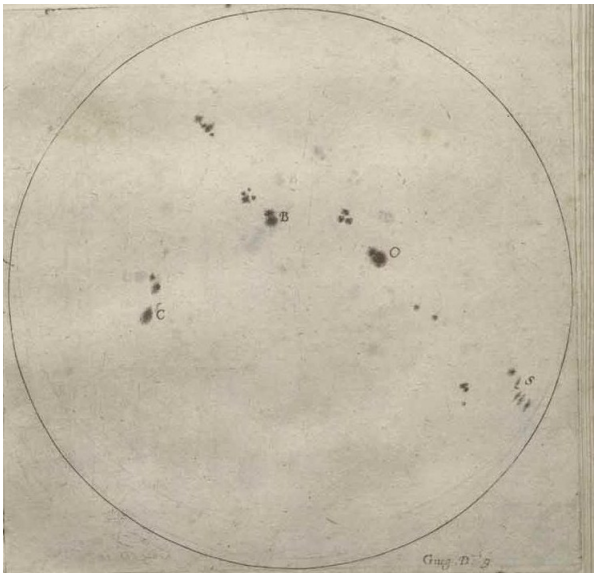

Figure 1.1: Observational sketches and classification of sunspots by shape, Galileo Galilei - Istoria e Dimostrazioni Intorno Alle Macchie Solari, 1613

during these 11 years, the latter also reported a time delay between the cycles of the two hemispheres (Spörer, 1888).

With the invention of the spectroscope (1814) and new insights on the origin of light at the end of the 19th century, new observational methods became available to astronomers. It was now possible to investigate physical properties of faraway objects by analysing their light. In 1896 Zeeman discovered atomic line splitting in a magnetic field (degeneracy of energy levels is broken by interaction of the magnetic field with the electron angular momentum), with the secondary lines ($m = \pm 1$ transitions) circularly polarised in opposite directions. The combination of a spectrometer and a polarimeter could now be used to measure a magnetic field: the wavelength separation of the lines gives a measure of the magnetic field. The next big step in the description of sunspots was the discovery of their magnetic nature by Hale (1908). Studying line splitting in Fe and Ti absorption lines, he found that sunspots exhibited very strong magnetic fields. In his continuing study of sunspots at the Mt Wilson observatory, Hale et al. (1919) found sunspot structures with opposite polarities on the northern and southern hemispheres. These polarities turned out to reverse at the end of the 11-year cycle, see Figure 1.2. This suggested that the true magnetic cycle is 22 years long, the 'Hale cycle', as opposed to the sunspot number cycle. In the same article Joy's observation regarding the latitudinal change in orientation of sunspots was published. Sunspots not the only magnetic structures appearing on the solar surface, which are generally denoted by 'magnetic active (surface) regions'.

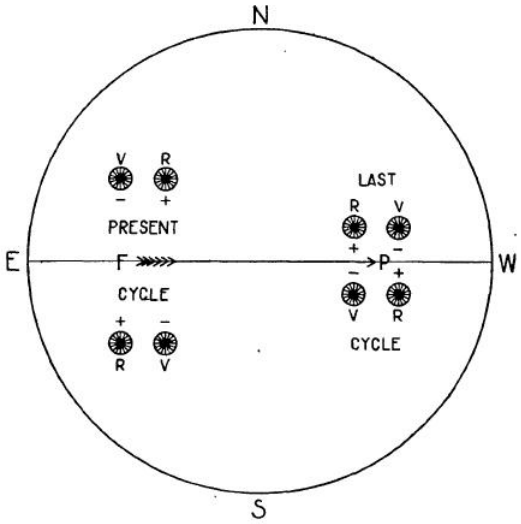

Figure 1.2: Illustration of the active region polarity reversal during consecutive 11-year solar cycles, G.E. Hale 1919

1.2 Developments in solar physics

Spectroscopic data revealed surface electromagnetic fields (Zeeman splitting), surface velocities (Doppler shift), constituent elements (absorption spectrum) and temperature and density estimates (line broadening, Stark effect, colour index and continuum assumption). Yet all of this is limited to the immediate photosphere, and until the second half of the previous century there was almost no information on the interior structure of the sun due to its opacity for electromagnetic radiation.

As both the understanding of theoretical physics and the amount of available data grew, different attempts were made to put these into a meaningful physical model.

A first mathematical model by Lane in 1870 (Tassoul & Tassoul, 2004) was based on the observation of low mass elements in a gaseous state by spectral analysis of the solar atmosphere. In this early model it was assumed that the Sun's interior was gaseous and chemically homogeneous throughout, and in a state of hydrostatic equilibrium, what would be called nowadays a 'polytropic model'. The hydrodynamical aspect of stellar structure was further developed in the beginning of the twentieth century by Eddington (1926): considering competition of radiative and convective energy transfer processes, today's picture of a radiative core and a convective envelope was established.

Unfortunately neither gravitational energy nor any other mechanism known at the time was sufficient to compensate for the radiative losses of the sun, and as such to explain its long life time (Eddington, 1920), as derived from independent geological estimates about the age of the Earth. The discovery of mass energy equivalence at the start of the 20th century lead to the development of nuclear physics , and soon the idea of thermonuclear reactions powering the Sun via fusion of hydrogen into helium (Chandrasekhar, 1939; Burbidge et al., 1957) was found to be the solution of the energetic problem.

While the questions about the structure of the Sun were slowly being solved, others arose with the observation of solar magnetic fields. In 1919 Joseph Larmor wrote a paper in which he proposed possible explanations for solar magnetic fields (Larmor, 1919), of which a self-excited dynamo based model, to *'maintain a permanent magnetic field from insignificant beginnings, at the expense of some of the energy of the internal circulation'*, seemed to him the only plausible explanation. However, Cowling (1933) proved the impossibility of axisymmetric dynamos and concluded his paper with *'The theory proposed by Sir Joseph Larmor, that the magnetic field of a sunspot is maintained by the currents it induces in moving matter, is examined and shown to be faulty; the same result also applies for the similar theory of the maintenance of the general field of Earth and Sun.'*

This discouraged further investigation, and the dynamo theory was left undeveloped, until it was picked up again by Elsasser (1946) in a description of the earth magnetic field. The solution to Cowling's 'antidynamo theorem' was found to be the intrinsic multidimensional nature of turbulence required to break the symmetry. In 1955, following the same lines, Parker reintroduced dynamos in solar physics (Parker, 1955).

The global dipole field and its reversal, observed in the 1950s by Babcock & Babcock (1955). This reversal showed that the solar magnetic field could not be due to permanent magnetism. A subsequent qualitative solar model by Babcock (1961), mathematically revised by Leighton (1969), introduced a global solar dynamo description. It is now clear that the solution to the origin of the solar magnetic field should involve a dynamo, but as yet we are still unable to reproduce from first principles its basic phenomenology.

Chapter 2

Mean-field theory and dynamos

2.1 Turbulence

The dynamical behaviour of fluids strongly depends on both initial and boundary conditions, and the presence of even small perturbations. In many circumstances these effects are so pronounced, that statements about the long term evolution of a flow, are, in general, true only in a statistical sense. This chaotic behaviour is often referred to as 'turbulence' and is due to the nonlinearity of the fluid equations.

Turbulence is characterised by a self similar energy transfer from larger to smaller scales. This can be visualised as large vortex structures, also called 'eddies', breaking up in smaller copies of themselves. This process continues eventually down to scales where dissipative energy losses dominate the behaviour of the flow. For isotropic homogeneous turbulence the energy contained in this cascade is distributed according to a power-law in wave number $k^{-5/3}$, as derived from dimensional arguments by Kolmogorov (1941). The exact value of the exponent can in principle be altered in the presence of anisotropy introduced either by gravity or magnetic fields.

The degree to which a flow is turbulent, can be characterised by the Reynolds number (Re), approximately the ratio between the nonlinear term and the dissipation term in the fluid equations. In fluid dynamics Re is customarily defined as $u \times l/\nu$, where l is a relevant length scale, u the local velocity and ν the viscosity. In magneto-hydrodynamics (MHD), it is possible to define a magnetic equivalent $Re_M = u \times l/\eta$, where the viscosity is substituted by the magnetic diffusivity η, and the ratio $Re_M/Re = \nu/\eta$ is called the magnetic Prandtl number(Pr_M).

2.2 Mean field theory

Physical phenomena observed on large spatial or temporal scales can be manifestations of processes happening on much smaller scales. Unfortunately it is computationally prohibitive to simultaneously compute and resolve the dynamics on all relevant scales. In the case of the Sun, the dynamical ranges are so large, that such an approach is virtually impossible. To realise global scale simulations, it is necessary to model the effects due to physics occurring on scales that are not resolved.

Two general formalisms exist: large eddy simulations (LES), where a spectral filtering is applied to distinguish between resolved and modelled scales, and mean field theory (in fluid dynamics also known as Reynolds averaged Navier-Stokes or RANS), where the distinction

is made between averaged ($\overline{X}$) and fluctuating (x) quantities, where

$$\mathbf{X} = \overline{\mathbf{X}} + \mathbf{x}. \tag{2.1}$$

Despite the resemblance of Equation (2.1) to a perturbation equation, mean-field theory does not make any assumption about the relative strength of the fluctuations, only that their average value is zero.

The averaging procedure must obey certain rules. These Reynolds averaging rules require that the average of the fluctuating component is zero and that the averaging operator must commute with respect to summation, derivation, multiplication with an averaged quantity:

$$\overline{f} = 0 \tag{2.2}$$
$$\overline{F+G} = \overline{F} + \overline{G} \tag{2.3}$$
$$\overline{\partial_s F} = \partial_s \overline{F} \tag{2.4}$$
$$\overline{\overline{F}G} = \overline{F}\,\overline{G} \tag{2.5}$$

While these rules seem natural, in practice they are not obeyed by many averaging procedures. An important exception are averages over periodic coordinate directions. Yet, for example, in spatial or time averaging, errors introduced by violations become negligible if the separation between the averaging scale and the scale over which the mean fields vary is large enough: integrating $F + f$ over a dimension with length L only returns F when variations in f average out to 0 over this scale L and deviations of F over scale L are still small.

Neither LES nor RANS leads to a closed system of equations, and consequently further assumptions need to be introduced. Both approaches are commonly used in fluid dynamics, however within the astrophysical MHD community their applicability has been questioned, in particular because behaviour at small scales is generally anisotropic (due to magnetic fields) and in violently turbulent flows it is very subjective to define a proper scale separation.

2.2.1 Example: induction equation

The time evolution of a magnetic field is described by the induction equation. In the non-relativistic limit, when temporal and spatial scales are larger than the plasma scales, it reads:

$$\partial_t \mathbf{B} = \nabla \times (\mathbf{U} \times \mathbf{B} - \eta\mu_0 \mathbf{J})\,. \tag{2.6}$$

To increase readability, in the rest of the text the units are chosen such that $\mu_0 = 1$. Using a Cartesian coordinate system, assuming the velocity field to be a simple shear flow (the flow direction is orthogonal to its gradient) $\mathbf{U} = Sx\mathbf{e}_y$, and a magnetic field such that $B_z = 0$ and B_x and B_y are only function of x, the evolution of the magnetic field becomes:

$$\partial_t B_y = B_x S + \eta \nabla^2 B_y \tag{2.7}$$
$$\partial_t B_x = \eta \nabla^2 B_x \tag{2.8}$$

It is evident that B_y can be generated by shearing of the B_x component, however, as no source seems available for the latter, the system will eventually just decay on a resistive timescale. This field generation by shear is referred to as the Ω-effect. The reason being that in rotating bodies (i.e. the solar interior), the shear generally corresponds to differential rotation.

After performing an averaging operation according to the rule of Reynolds averages, we split the involved quantities of Equation (2.8) into their mean and fluctuating parts. We can now separately consider the evolution of the mean components:

$$\partial_t \overline{B}_y = (\nabla \times \overline{\mathbf{u} \times \mathbf{b}})_y + \overline{B}_x S + \eta \nabla^2 \overline{B}_y \tag{2.9}$$

$$\partial_t \overline{B}_x = (\nabla \times \overline{\mathbf{u} \times \mathbf{b}})_x + \eta \nabla^2 \overline{B}_x \tag{2.10}$$

where an additional term compared to the total field equations, now occurs. This term is an average that depends on the correlation between magnetic and velocity fluctuations, and is called the mean electromotive force (EMF). The evolution equations for the fluctuating parts can be obtained by subtracting the mean from the total field equations, for the y-component this gives:

$$\partial_t b_y = \left(\nabla \times \left[\mathbf{u} \times \overline{\mathbf{B}} + \overline{\mathbf{U}} \times \mathbf{b} - \overline{\mathbf{u} \times \mathbf{b}}\right]\right)_y + b_x S + \eta \nabla^2 b_y \tag{2.11}$$

The simplest assumption one can make is that the EMF depends only on the local value of the mean quantities, and in particular on the local value of the mean magnetic field and its spatial derivatives:

$$\overline{\mathbf{u} \times \mathbf{b}}_i = \alpha_{ij} \overline{B}_j + \eta_{ijk} \partial_k \overline{B}_j = \overline{\mathcal{E}}_i, \tag{2.12}$$

where the turbulent transport coefficient tensors α and η themselves may depend on mean field quantities. If there is a non-zero α, it is possible to create B_x starting from a finite field in the y direction, this is the α-effect. The resulting generation of magnetic energy from kinetic energy is indicated by the term dynamo.

In the isotropic case the EMF expression reduces to

$$\overline{\mathcal{E}} = \alpha \overline{\mathbf{B}} - \eta_t \overline{\mathbf{J}} \tag{2.13}$$

where η_t can be interpreted as a turbulent diffusivity (Brandenburg & Subramanian, 2005).

2.2.2 The α-effect

It is possible to generate magnetic fields through turbulent motions. Following the formalism from Steenbeck et al. (1966), dynamo term linear in B is dubbed the α-effect. Note that while the isotropic part of the η_t-tensor term is associated with diffusive decay, its anisotropic components can give rise to a large scale field in the presence of a magnetic field gradient.

From the analysis Pouquet et al. (1976), it is clear that in the case where the effect of magnetic fields on the flow can not be neglected, the expression for α can be approximated by:

$$\alpha = -\frac{\tau}{3} \overline{\mathbf{u} \cdot \omega} + \frac{\tau}{3\rho} \overline{\mathbf{j} \cdot \mathbf{b}}. \tag{2.14}$$

The first term, combining the velocity ($\mathbf{u}$) and vorticity (ω) fluctuations and a timescale τ is indicated as the kinematic α-effect. Regarding if for, a certain flow, this term remains finite or becomes 0 in the limit of high Re_M, the resulting dynamo will be called respectively fast or slow. The second term, the mean value of scalar product of the fluctuating components of magnetic field ($\mathbf{b}$) and current density ($\mathbf{j}$) divided by the density (ρ), also called the 'current helicity' of the fluctuating fields, reduces the effect in the presence of strong magnetic fields. Because of this, the α-effect is 'quenched' and the dynamo saturates (Ivanova & Ruzmaikin, 1977). We can approximate this current helicity by magnetic helicity $\mathbf{a}\cdot\mathbf{b} \approx k^2\mathbf{j}\cdot\mathbf{b}$, where $\mathbf{a}$ is the fluctuating component of the magnetic vector potential and $1/k$ a length scale. Thus the magnetic quenching can be alleviated by a flux of magnetic helicity from the fluctuating fields out of the domain (Kleeorin et al., 2000; Blackman & Field, 2000).

Depending on the relative importance of the shearing term in Equation (2.10), dynamo systems are generally categorised as $\alpha\Omega$ or α^2 or $\alpha^2\Omega$ dynamo, in the latter case has both effects occur with a similar order of magnitude. Different mechanisms will also result in different field topology (Chabrier & Küker, 2006).

2.3 Closure models

The turbulent transport coefficients in the dynamo example above are an example of a closure model. They can be given (from measurements or estimates) or derived from other equations, for example an evolution equation for the EMF (Brandenburg et al., 2005), which eventually will introduce further unknowns (which have to be modelled).

These models generally have a certain parameter range for which they are valid, extrapolation to a different regime is not necessarily a good idea.

Unfortunately the model simplifications are based on perturbation assumptions, like low magnetic Reynolds number (dominant diffusion term) or small fluctuating fields (triple correlations can be neglected). In the astrophysical context these parameter domains are relatively uninteresting, but on the bright side, this domain is also accessible by DNS and the validity of these approaches can be tested for this regime.

2.3.1 Example: test-field method

An alternative approach is the measurement of transport coefficients in DNS. Being a diagnostic method, this concept has the drawback that one is restricted to flow conditions that can be produced in DNS. Also, in itself, this method has no predictive character (only by interpreting the findings in a model).

A promising technique is the 'test-field method' (Schrinner et al., 2005, 2007; Rheinhardt & Brandenburg, 2010): Through hydrodynamical calculations a turbulent flow is calculated. By adding a test (magnetic) field $\overline{\mathbf{B}}^{(q)}$, with a small amplitude to stay in the kinematic regime and a geometry that allows relatively simple numerical analysis, this turbulent system generates fluctuations $\mathbf{b}^{(q)}$:

$$\partial_t \mathbf{b}^{(q)} = \nabla \times [\overline{\mathbf{U}} \times \mathbf{b}^{(q)} + \mathbf{u} \times \overline{\mathbf{B}}^{(q)}] + \eta\nabla^2\mathbf{b}^{(q)} + \nabla \times [\mathbf{u} \times \mathbf{b}^{(q)} - \overline{\mathbf{u} \times \mathbf{b}^{(q)}}]. \qquad (2.15)$$

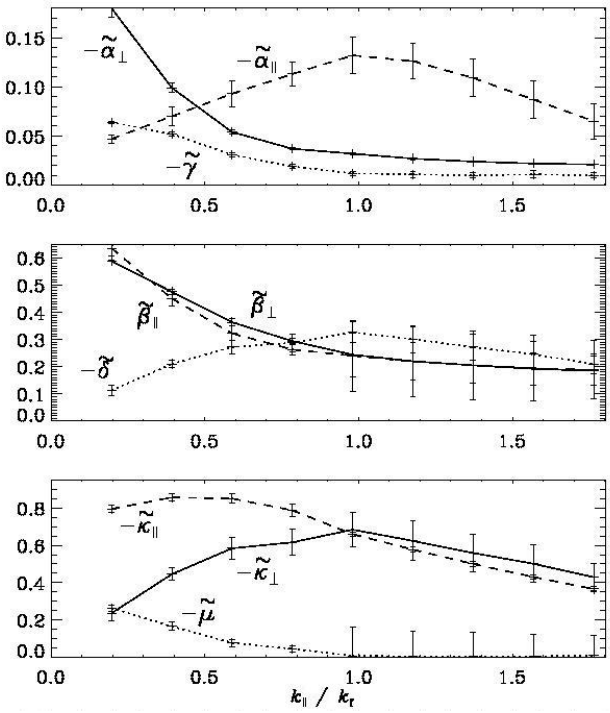

Figure 2.1: Effect of scale separation on transport coefficients for an axisymmetric turbulent flow in the presence of rotation and density stratification.

This feedback is used to calculate the EMF, which in turn allows us to determine the mean field coefficients for the given flow by solving.

$$\overline{\mathcal{E}}_i = \overline{\mathbf{u} \times \mathbf{b}^{(q)}}_i = \alpha_{ij} \overline{B}_j^{(q)} + \eta_{ijk} \partial_k \overline{B}_j^{(q)} \tag{2.16}$$

The validity of the method hinges on the assumption that the transport coefficients depend only on the flow ($\bar{\bar{\alpha}}\left(\overline{\mathbf{U}}, \mathbf{u}\right)$ and $\bar{\bar{\eta}}\left(\overline{\mathbf{U}}, \mathbf{u}\right)$). Hence it is exact in the kinematic regime, where the magnetic field is not strong enough to affect velocities, with fields varying linear in space. For stronger mean magnetic fields the numerical simulation should be full MHD instead of only hydrodynamical, however the formalism still holds through implicit $\overline{\mathbf{B}}$-dependence of $\overline{\mathbf{U}}$ and $\mathbf{u}$) and it is possible to obtain transport coefficients as a function of the average velocity and magnetic field. The method can be expected to break down when magnetic fluctuations affect the flow (the equations are no longer linear in the test-field).

As the validity of this method is still under some discussion, it is important to provide results which can be compared to the ones obtained through different methods or analytical calculations. In this context we studied in **Paper III** how measured turbulent transport coefficients depend on angular velocity and gravity in axisymmetric turbulence, i.e. turbulence that has only one preferred direction. The advantage of this setup is that due to symmetry, the amount of possible non-zero coefficients in Equation (2.16) reduces from $9+27 = 36$ to 9, which reduces the amount of computations and makes it easier to interpret

the physical origins and effects of the individual coefficients (competing pumping effects and (an)isotropic diffusion and magnetic field generation). The findings seem to support earlier predictions. In particular, in the absence of gravity and for weak rotation, as quantified by the Coriolis number $Co = 2\Omega/u_{\rm rms}k_f$, the only non-vanishing coefficients are $\beta_\perp$ and $\beta_\parallel$, which quantify contributions to the mean electromotive force proportional to the mean current density perpendicular and parallel to the preferred direction. As angular velocity increases, several new effects come into play, such as an effect proportional to $\Omega \times \overline{\mathbf{J}}$, also known as the Rädler-effect (Rädler, 1969), quantified by the coefficient δ, as well as effects perpendicular and parallel to a vector $\overline{\mathbf{K}}$, which is the projection of the symmetric part of the magnetic field gradient tensor along the proffered direction.

2.4 Observed dynamos

2.4.1 Experimental measurements

Liquid sodium experiments

Since its theoretical prediction, a number of experiments have been devised to demonstrate the existence of the α-effect and to verify and extend our current knowledge. Up until now successful generation of a magnetic field was obtained in a number of liquid sodium experiments in Karlsruhe (Müller & Stieglitz, 2002), Riga (Gailitis et al., 2004) and Cadarache (Monchaux et al., 2009). Sodium was used for its high conductivity and low mass density (among liquid metals), in order to be able to reach sufficiently high Re_M with reasonable power consumption. Liquid metal experiments are however limited in diagnostics, due to their electromagnetic opacity, as well as in accessible parameter range. Hopefully the plasma experiment under construction in Madison (Spence et al., 2009) will allow us to study the effect beyond the current limitations.

Reversed field pinch

In fact there are already plasma experiments where the α-effect is found to play an important role, namely in the reversed field pinch setup (RFP). This is a transformer-based magnetic confinement plasma experiment in the context of nuclear fusion research.

In the RFP experiment a current generates and heats a plasma in a toroidal vessel. This current is generated by a time dependent flux, confined in an iron core, through the conducting plasma ring, which essentially plays the role of the load in a transformer setup. The plasma is confined by magnetic pressure from, on one hand, an externally applied toroidal field (poloidal magnetic coils) and, on the other hand, a poloidal field generated by the toroidal current. The fact that the latter is of the same magnitude order as the applied field is one of the key differences compared to the tokamak setup. The observed toroidal magnetic field profile during operation shows a sign reversal near the edge, after which the device was named.

The experiment is used to study MHD phenomena that might be relevant for research in nuclear fusion, like turbulent transport and resistive wall instabilities Bodin (1983); Ortolani (1989). The RFP setup is currently not considered as a possible reactor option due to its high energy and particle losses.

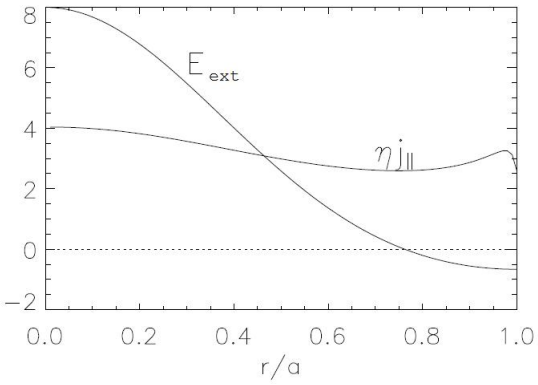

Figure 2.2: Toroidal component of current and electric field in the RFP, adapted from Ji & Prager (2002)

The presence of a dynamo in this context is apparent from the need for an EMF term to balance Ohm's law, shown in Figure 2.2:

$$\eta \overline{\mathbf{J}}_{\text{ext}} = \overline{\mathbf{E}} + \overline{\mathbf{E}}_{\text{ext}} + \overline{\mathbf{U}} \times \overline{\mathbf{B}} + \overline{\mathcal{E}}, \tag{2.17}$$

where we consider the externally applied electric field separately as a source term. The effect of the EMF is a flattening of the current profile by reduction of the current in the center and an increase near the edge. In terms of stability this means a reduction of current instabilities in the center and a reduction of kink instabilities (which are proportional to the field gradient), but also an increase of the wall instabilities and as such the presence of a dynamo does not solve the problem of poor confinement.

In **Paper IV** we attempt to describe the RFP dynamo in the context of Equations (2.13) and (2.14). This model is generally used in the astrophysical context where magnetic fields are generated from a small seed field by the α-term in the EMF. In the problem at hand, however, a strong magnetic field is already present and the result of the α-effect, generated from shearing instabilities, is a reduction of the field decay rate to resistive rather than turbulent time scales (Ji & Prager, 2002). In our simulations we find indeed this slowed decay as shown in Figure 2.3, however we generally do not find the field reversal, except when including helicity fluxes in the domain, see Figure 2.4. This last result appears to contradict earlier statements that the α effect would be responsible for the reversal (Bhattacharjee & Hameiri, 1986), although it may be possible that our current model is too simple.

2.4.2 Astrophysical dynamos

Dynamos are believed to be responsible for the major fraction of the large scale magnetic fields observed in the universe, from galaxies to the field of our own little planet. The need for dynamos is not always obvious. In galaxies, the Ohmic decay times exceed the age of the universe. However, the gas is turbulent (driven by supernova explosions) and the turbulent decay time is only some ten million years. Therefore, the field must be supplied

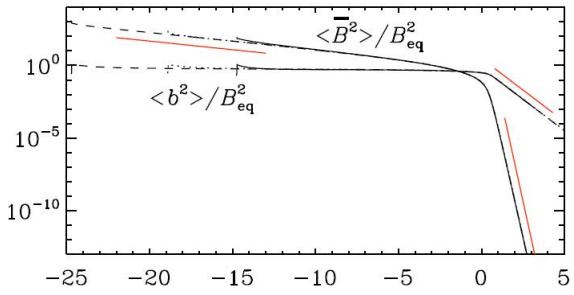

Figure 2.3: Time evolution of magnetic energy contained in the mean and fluctuating component, taken from **Paper IV**.

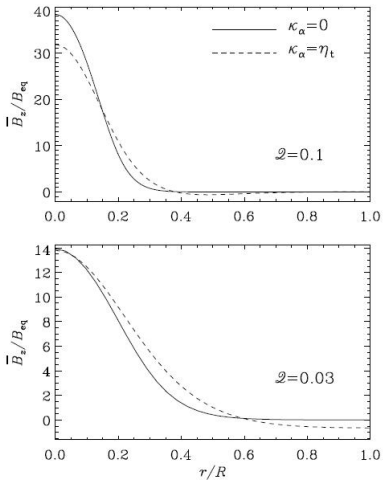

Figure 2.4: Radial profile of the toroidal component of the magnetic field with (dashed line) and without (full line) helicity fluxes for two different ratios of induced to applied field, taken from **Paper IV**.

by a dynamo. By contrast, in Earth's core, the Ohmic decay time is only of the order of ten thousand years, so the need for a dynamo is very obvious. In the Sun, the Ohmic decay time is again quite long, so a large scale magnetic field could survive in the radiative interior for long times, but it would be difficult to explain reversals on an 11 year time scale. The Sun's magnetic field will be addressed in more detail in the following chapter.

Chapter 3

Observed properties of sunspots

3.1 Sunspot statistics

3.1.1 22 year cycle

As mentioned before, the sunspot number count exhibits a cyclic behaviour with a period of, on average, 11 years with a magnetic polarity reversal across the equator in subsequent cycles, giving a 22 year magnetic cycle. During such a cycle one observes an equator-ward migration of active regions ('Spörers law') and a pole-ward migration of the mean surface magnetic field (Li et al., 2001).

3.1.2 Large scale time modulation

Sunspot data shows a modulation of maximum activity on longer timescales, see also Figure 3.1, down to a nearly total absence during 'grand minima'. Only one of the latter, the Maunder minimum, has occurred since the beginning of systematic observations. However, solar surface activity in pre-Galilean times can be estimated from isotopic ^{10}Be abundances in arctic ice (Beer et al., 1990), a comparison between sunspot count and ^{10}Be data is shown in Figure 3.2. The increased presence of this less stable isotope in an ice layer at a certain depth can be explained by a larger amount of incoming cosmic rays at the time of the corresponding ice formation due to a weaker shielding during periods of low solar activity.

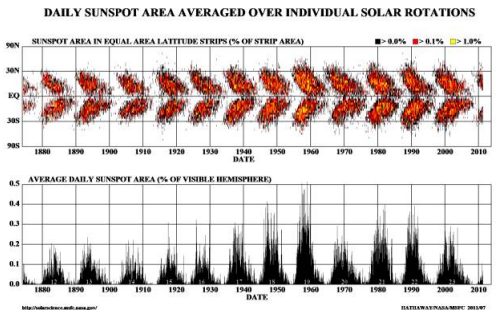

Figure 3.1: 'Butterfly diagram': evolution of the number of sunspots as a function of latitude and time, taken from the Marshall Space Flight Center website

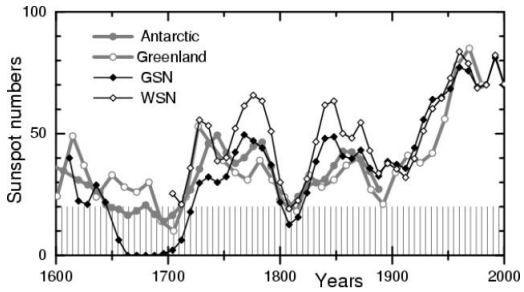

Figure 3.2: Comparison of sunspot observations (GSN/WSN) with the solar activity reconstructed from ^{10}Be abundance in arctic ice. Weak activity corresponds to lowered magnetic shielding and as such increased cosmic radiation, leading to formation of less stable isotopes (Usoskin et al., 2004).

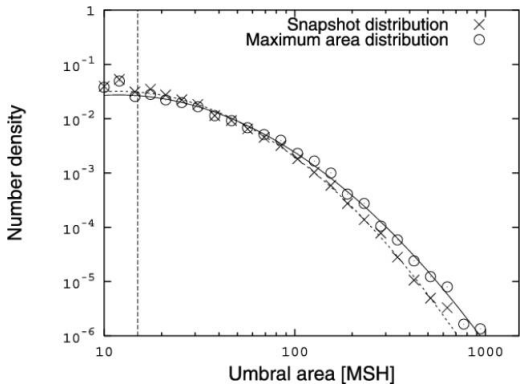

Figure 3.3: Sunspot size distribution (Baumann & Solanki, 2005), sunspot area given in MSH (millionth of a solar hemisphere).

3.2 Individual spots

3.2.1 Surface structure

By 'sunspot', early astronomers referred to a black area ('umbra' - not necessarily a single closed area and therefore sunspots are also referred to as 'active surface region'), covering a solar surface area of the order 10^7 - 10^9 square kilometer, see also Figure 3.3, and a relatively dark area surrounding it (penumbra), an observation is shown in Figure 3.4. The reduced observed radiation is caused by a suppression of the convective energy flux by magnetic pressure. The magnetic fields have a field strength of the order 2000-4000 Gauss in the darkest part of the umbra down to 700-1000 Gauss at the outer edge of the penumbra. Because of these strong magnetic fields, also the the temperature is reduced, by respectively 1000-1900K in umbra and 250-400K in penumbra (Solanki, 2003): the total pressure inside the spot has a large contribution of the magnetic pressure, thus radial pressure balance requires the gas pressure, and as such the temperature, inside to be much lower than outside. In addition, because of this temperature reduction, the optical depth reaches unity at much larger geometrical depth (order 500-1500 km), this apparent surface

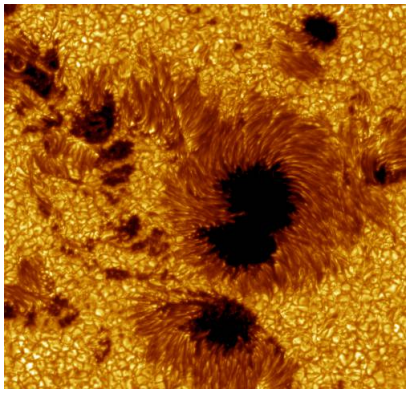

Figure 3.4: Sunspot observed by the Swedish Solar telescope, taken from the website from the Institute for Solar Physics.

depression was observed by Wilson in 1769 (Giovanelli, 1982). These fields have a field strength of the order 2000-4000 Gauss in the darkest part of the umbra down to 700-1000 Gauss at the outer edge of the penumbra. An active region usually exhibits a bipolar magnetic structure with a latitude dependent tilt with respect to the toroidal direction ('Joys law', Hale et al. (1919)). Sunspots have a larger rotation speed than the surrounding medium: at the equator the solar angular velocity is about 450nHz, for young sunspots this can be as high as 473 nHz , this velocity decreases as the sunspot ages and and is lower for sunspots in lower attitudes (Balthasar et al., 1986; Zappala & Zuccarello, 1991). The reason for this velocity difference has been sought in anchoring or the formation of sunspots deeper in the convection zone, where angular velocities are higher (Balthasar et al., 1982). Sunspots often have an internal rotation. Its origins are under discussion, but can be interpreted as the result of twist in an emerging flux tube (Longcope et al., 1999).

Local helioseismology has provided more information on the flow structure around sunspots, showing a rather shallow structure surrounded by strong convective motions (Kosovichev, 1996, 2002, 2004; Zhao et al., 2001), see Figure 3.5.

3.2.2 Emergence and decay

In the early stage of a sunspot we see the appearance of an umbral area and the subsequent growth of a penumbra (Schlichenmaier et al., 2011). Upon emergence there is a large spread on the tilt angle as anticipated by Joy's law with a relaxation period of the order of a few days (Howard, 1996; Kosovichev & Stenflo, 2008).

DNS can be seen as an experimental tool. The advantages of this type of experiment are: simple diagnostics and fully controlled boundary and initial conditions, the disadvantages are: limited parameter space (due to resolution) and uncertainty about physical relevance of the applied boundary and initial conditions.

Under certain initial conditions, by solving MHD and radiative transfer equations in DNS in the top of the convection zone it is now possible to produce sunspot-like structures very similar to observed ones (Rempel et al., 2009), see also Figure 3.6. This gives us the opportunity to investigate the physics behind observed surface effects, like the Evershed

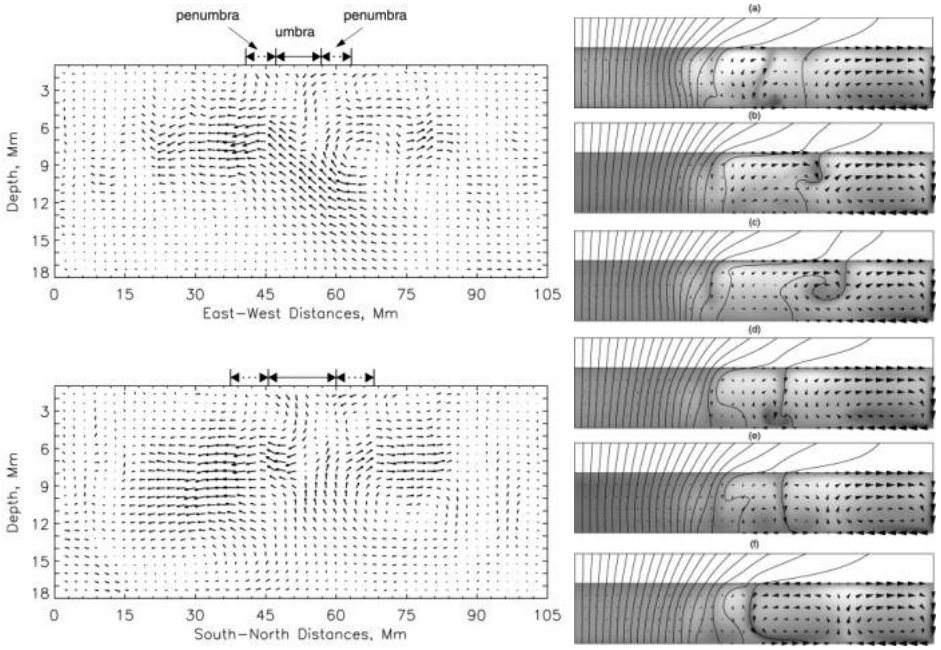

Figure 3.5: Flows around a sunspot from local helioseismology data (Zhao et al., 2001) and a corresponding model (Hurlburt & Rucklidge, 2000).

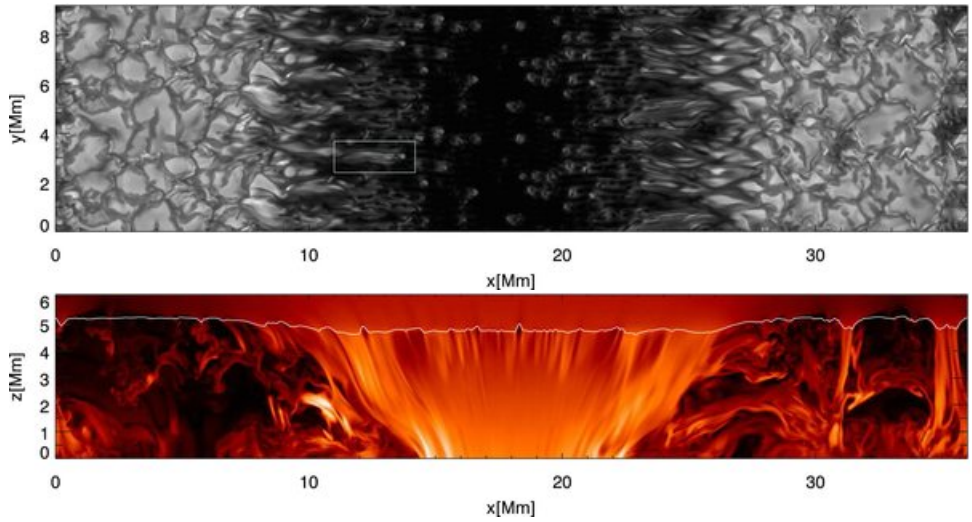

Figure 3.6: Sunspot simulation (Rempel et al., 2009), surface view (above) and depth profile (below).

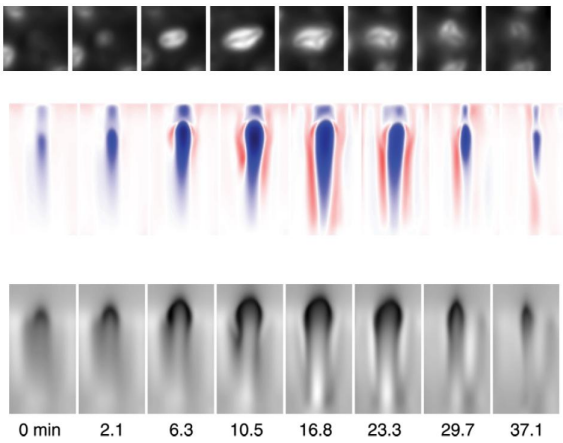

Figure 3.7: Evolution of bright umbral dots (Schüssler & Vögler, 2006).

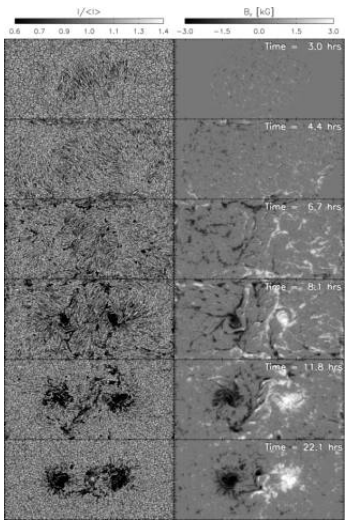

Figure 3.8: Sunspot emergence simulation (Cheung et al., 2010).

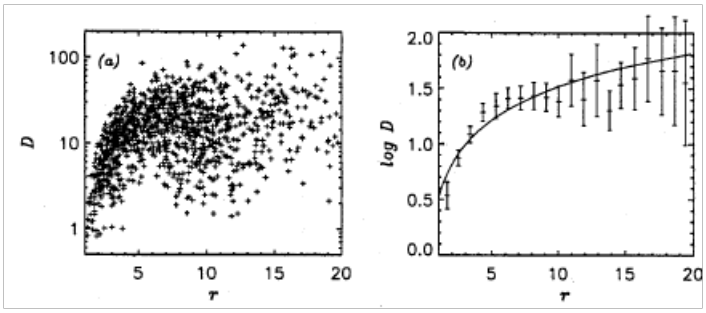

Figure 3.9: sunspot decay rate in function of radius (Petrovay & Van Driel-Gesztelyi, 1997).

effect (radial outflows along magnetic field lines, Scharmer et al. (2008)) and umbral spots (Schüssler & Vögler, 2006), see Figure 3.7.

Note however, that as one goes deeper into the convection zone, the uncertainty of the simulation grows significantly. An initial condition that has been used for simulating the emergence of sunspots is a magnetic flux tube at a depth of about 20 Mm (Cheung et al., 2010), which will then buoyantly rise. The acceptable realisation at the surface, as shown in Figure 3.8, does, however, not provide sufficient justification for the magnetic configuration assumed at that depth.

Decay of sunspots is well documented, but again the physical background is not sufficiently understood. Sunspot statistics appear to indicate a decrease of the area proportional to the sunspot radius (Petrovay & Van Driel-Gesztelyi, 1997), shown in Figure 3.9, which would indicate a decay process at the edge of the spot. Parker (1975) proposed a decay through MHD instabilities. However, the typical dynamical timescale involved would be only a few hours (radius divided by Alfvén speed). Meyer et al. (1977) found that if one has a sufficiently strong magnetic flux concentration, buoyancy is able to stabilise interchange instabilities.

An alternative would be decay through diffusion. The decay rate is much larger than what molecular diffusion would be able to sustain, but turbulent diffusion would be able provide such a fast decay (Krause & Rüdiger, 1975). In the latter case the diffusivity would be quenched in the center of the spot by the strong magnetic field. The decay rate found in this case is actually somewhat larger than the observed one (Rüdiger & Kitchatinov, 2000). If the magnetic profile is very steep, Petrovay & Moreno-Insertis (1997) argue that the diffusion would be dominated by erosion of the edge through turbulence outside the spot.

3.3 Solar interior

To understand the physics of sunspots we of course need information about the conditions in which they form. A hydrostatic solar model with a high degree of refinement has been developed in the previous century, yet limited information is available about the dynamics and magnetic fields in the Sun.

Naturally we have information about the surface magnetic field (see Figure 3.10) and

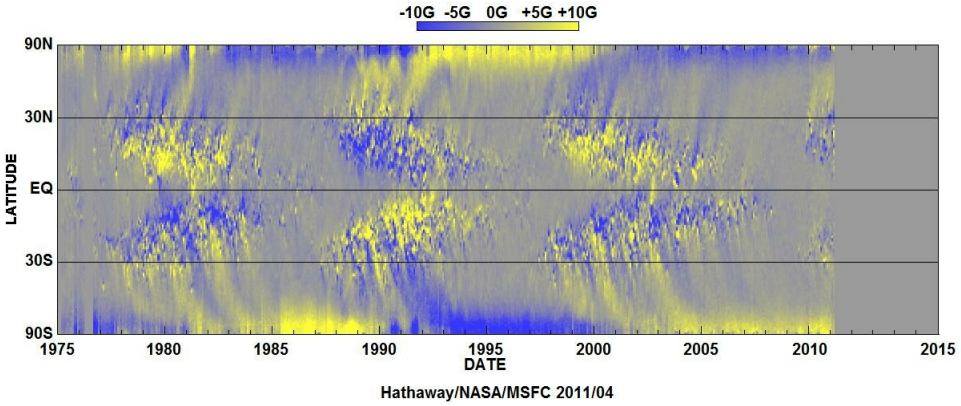

Figure 3.10: Latitude and time dependency of average solar surface magnetic fields, taken from the Nasa Marshall Space Flight Center website

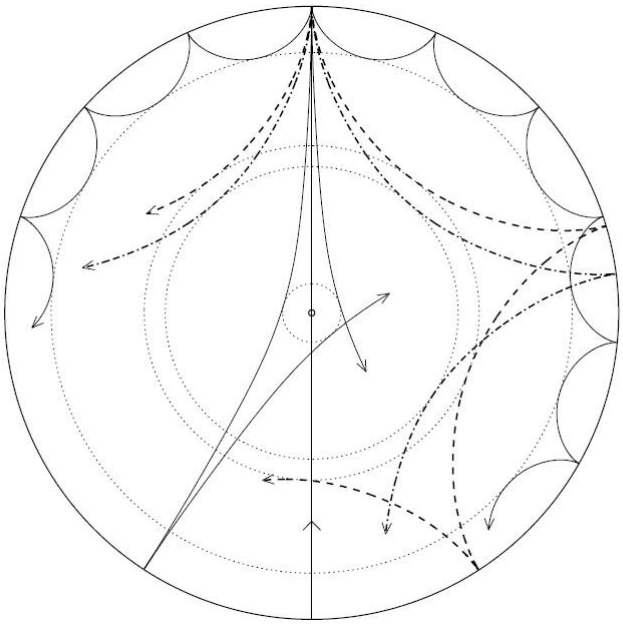

Figure 3.11: Propagation of rays of sound waves through a cross section of a solar model. The ray paths are bent by the increase with depth in sound speed until they reach the inner turning point, where the waves undergo total internal refraction (figure taken from by Lecture Notes on Stellar Oscillations by Christensen-Dalsgaard, 2003)

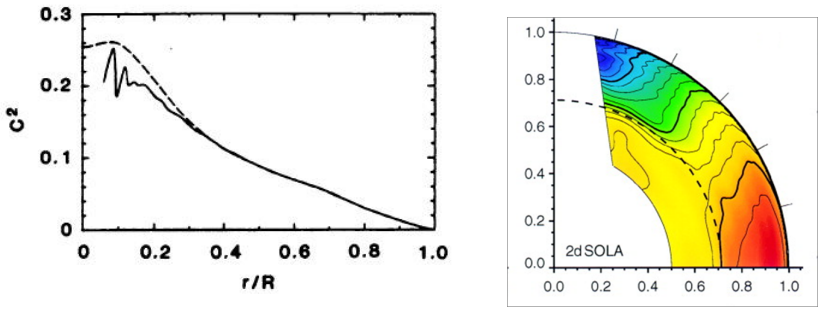

Figure 3.12: Radial profile of squared sound speed (Christensen-Dalsgaard et al., 1985) and toroidal velocity in the solar convection zone (Schou et al., 1998).

flows at our disposition. However, direct information about magnetic fields below the surface is inaccessible due to large opacities.

While electromagnetic waves are strongly damped in the sun, acoustic waves are not, although one has to distinguish between pressure and gravity waves as the latter only propagate in the stably stratified regions. The pressure waves (frequency typically a few mHz) can propagate in the solar convection zone and create patterns on the surface that depend directly on sound speed variations in the convection zone, illustrated in Figure 3.11. Inversion of this pattern allows to reconstruct radial profiles of velocity (advection of the acoustic waves) and temperature (combination of measured sound speed and a chemical composition inferred from a solar model). The study of acoustic wave propagation in the Sun is called 'Helioseismology' (Christensen-Dalsgaard et al., 1985; Kosovichev, 1996, 2002).

From the temperature and density profiles, one can calculate that between 0.713 solar radii (Christensen-Dalsgaard et al., 1991) and the photosphere, the entropy gradient is negative, so the sun is unstable to convection and this region is thus dubbed 'convection zone'. The location of the bottom of the convection zone is also identified in the radial dependence of the sound speed, see the left hand panel of Figure 3.12. 'Convection' indicates turbulent heat transport without a net particle transport, a simple illustrative example is the Rayleigh-Bénard cell, where heated fluid rises into a colder layer where it deposits its energy, is pushed a bit to the side by other upcoming fluid elements and sinks down again. This behaviour arises because in the opaque outer layer of the Sun radiative heat transfer is inefficient. Near the interface between a convectively stable and an unstable region there will be a certain diffusion of convective motions into the former: the affected stably stratified zone is called 'overshoot layer'.

The toroidal velocity profile shows a strong shear layer at the bottom of the convection zone, named 'tachocline' (Spiegel & Zahn, 1992; Charbonneau et al., 1999), below which the Sun rotates rigidly, seeFigure 3.12. In the convection zone the rotation pattern varies in a spoke-like fashion. There is one more layer with strong shear near the solar surface (at a depth of approximately 35 Mm). Poloidal velocities are about an order of magnitude smaller than the toroidal ones and as such are hard to measure. Many solar dynamo models incorporate a pole-wards surface flow and an equator-wards return flow near the bottom of the convection zone, this flow pattern is referred to as 'meridional circulation'. However, recent observations seem to indicate that the return flow is much closer to the surface,

namely around the same radial distance as the aforementioned near-surface shear layer (Hathaway, 2011).

Chapter 4

Models of a magnetic Sun

4.1 Aspects of a (solar) model

The idea behind modelling: *'Make everything as simple as possible, but not simpler.'* When starting to build a model one has to consider which processes take place, which of those are the most important and which ones can be neglected for a given parameter space. This choice of which physics to include can be made based on estimations from previous insights or parameter dependency experiments and then tested comparing the results with observations. These experiments can be of numerical or laboratory origins, with limitations of appropriate boundary and initial conditions and respectively resolution or realisability and diagnostics.

Unfortunately, the solar convection zone is far out of the reach of current day experiments and thus a large number of competing processes remain to complicate our view. At the same time, the available observational data is limited to flows and temperatures (sound speed) in the convection zone (initial conditions) and surface magnetism (observable one should be able to reproduce).

Generation of sunspots is strongly tied to the global magnetic field generation and transport. Below a summary of thoughts on these processes.

4.2 The Rising Flux Tube

The solar dynamo is usually described in the $\alpha\Omega$-dynamo formalism: generation of a toroidal field by shearing a poloidal field by differential rotation ('Ω-effect') and the regeneration of a poloidal field from a toroidal field by helical turbulence ('α-effect').

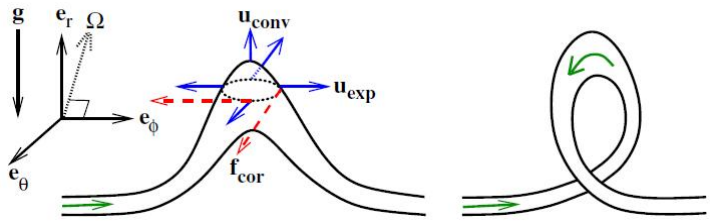

Figure 4.1: Rising flux tube model: a perturbed flux tube segment subject to magnetic tension, magnetic buoyancy, adiabatic expansion and Coriolis forces rises and generates internal twist (Ossendrijver, 2003).

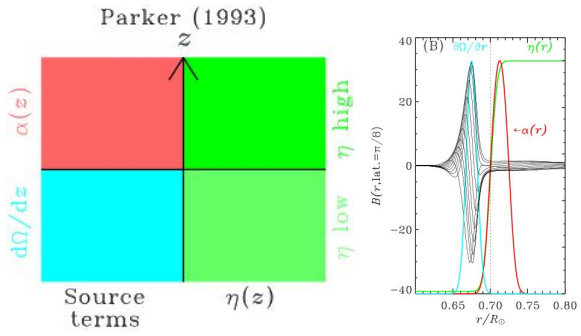

Figure 4.2: interface dynamo as proposed by Parker(left) and a simulation implementation(right) (Charbonneau, 2005).

In this generally accepted framework, thin flux tubes are generated and stored in the overshoot layer at the bottom of the convection zone, where turbulent diffusion is not strong enough to instantly destroy any newly created magnetic structures, and buoyantly rise to the surface, forming sunspots, see Figure 4.1. Different rising flux tube models agree on generation of the toroidal magnetic field by shearing the poloidal field in the strong tachocline shear layer, but offer several alternative processes to generate a poloidal field. Based on the location where the latter is produced, one can divide the models in three main categories:

- Overshoot dynamos: the α effect is located at the base of convective zone, originating from magnetic buoyancy instabilities (Thelen, 2000) or hydrodynamic instability of latitudinal differential rotation (Dikpati & Gilman, 2001). However, it has been argued that the width of the overshoot layer may be too small for these models to be viable (Rüdiger & Brandenburg, 1995).

- Interface dynamos: the alpha effect is located above the shear layer where the magnetic field is stored (Parker, 1993), thus avoiding quenching by the presence of a strong magnetic field, see Figure 4.2.

- Babcock-Leighton type flux transport dynamos: rising flux tubes are tilted by the Coriolis force to produce Hale's polarity law, resulting in a net poloidal field upon emergence. The meridional flow is responsible for pole-ward transport of this residual field (Dikpati & Charbonneau, 1999). This corresponds to an alpha effect in the near-surface layer with a reversed sign compared to the previous models.

Given that it has no memory, a dynamo alone can not account for the observed large scale time modulations of solar activity. It has been suggested (Gough, 1981) that these could be the result of magnetic or thermal coupling between the radiative and convective regions in the Sun.

4.3 Unanswered questions

Numerical simulations and observations by local helioseismology have raised a number of questions for the accepted picture of flux tubes rising from the overshoot layer. Some have been answered, others have been swept under the carpet as a sacrifice to the conceptual elegance of the theory (Brandenburg, 2005; Parker, 2009), a brief look at the latter:

- The flux tube simplification, initially introduced for educative purpose, has become a key element in the theory. Questions have been raised about the physical relevance of this field structure (Cattaneo et al., 2006), and so far one has not been able to produce these tubes in numerical simulations.
- The buoyant rise is pictured as a dominant transport process, however, simulations have shown competing downward turbulent pumping (Nordlund et al., 1992).
- A magnetic field strength of 100kGauss at the base of the convection zone (implying magnetic energies a hundred times larger than the energy contained in the local velocity field) are required to avoid pole-ward deflection of rising flux tubes by the Coriolis force (Choudhuri & Gilman, 1987; Fan et al., 1993).
- For integrity during rise through the convection zone (over 20 scale heights) fairly large fields (Fan et al., 2003) and a certain degree of twist are required . A small degree of twist (above a critical value twist would make the tubes kink-unstable (Linton et al., 1996)) can stabilise tubes to some extent with respect to Rayleigh-Taylor instabilities (Moreno-Insertis & Emonet, 1996) as long as the Alfvén speed of the azimuthal component is larger than the relative speed of the surrounding plasma (Abbett et al., 2000, 2004).

4.4 Distributed dynamo

The issues above are key criticisms on the deeply seated flux tube dynamo paradigm and appear to favour the idea of sunspot generation in the top layer (70Mm) of the convection zone. Other observations and numerical results in favour of a dynamo operating in the near-surface layer of the Sun:

- Helioseismologic observations show that sunspots are fairly shallow structures (Kosovichev, 2002)
- The observed sunspot angular velocity coincides with the rotation speed around 35Mm below the surface (Thompson et al., 2003).
- The buoyancy of magnetic structures in the convection zone (Parker, 1975) is suppressed by downward pumping (Nordlund et al., 1992) and as such need not lead to a strong loss of magnetic flux.
- Fully convective stars (i.e. without a possibility to store magnetic fields) have dynamos (Vilhu, 1984)

Chapter 5

Sunspots as local collapse

5.1 Turbulent sunspot formation

As magnetic fields restrict plasma motions, it is fairly straightforward to assume that turbulent effects will have a certain (anisotropic) field dependence. Mean-field simulations with B-dependent turbulent transport coefficients (Kitchatinov & Mazur, 2000) and turbulent pressure (Rogachevskii & Kleeorin, 2007; Brandenburg et al., 2010) have shown a possibility to create sunspot-like large scale magnetic structures. Of course the validity of the assumed magnetic dependence should be tested in direct simulations for the appropriate parameter range.

5.2 Thermal collapse

5.2.1 Principle

When turbulent heat transport is locally suppressed close to the solar surface, the radiative losses can no longer be balanced by the reduced heat flow. As a result the plasma cools down and, in a compressional downflow, enhances the magnetic field.

5.2.2 Model

The model was tested in a 2D mean-field simulation by Kitchatinov & Mazur (2000), solving the induction and entropy equation in a stratified convection setup with an imposed vertical magnetic field of 400 or 700Gauss. The quenching of the turbulent transport coefficients is based on the result of an analysis within the quasi-linear approximation by Kitchatinov et al. (Kitchatinov et al., 1994). For strong fields with respect to the equipartition field strength (a hypothetical magnetic field containing the same energy as the local velocity field), the thermal diffusivity is inversely proportional to the ratio $\overline{\mathbf{B}}/B_{eq}$. In the absence of a magnetic field, there is of course no magnetic quenching.

Other approximations in the simulations include: inelasticity and near-adiabatic stratification, also, due to computational limitations on the density contrast, it was not possible to include the upper 3Mm of the convection zone.

The simulations show local magnetic field enhancements (higher than observed in the Sun), heat flux reduction (smaller than observed) and downdrafts (in agreement with helioseismic tomography).

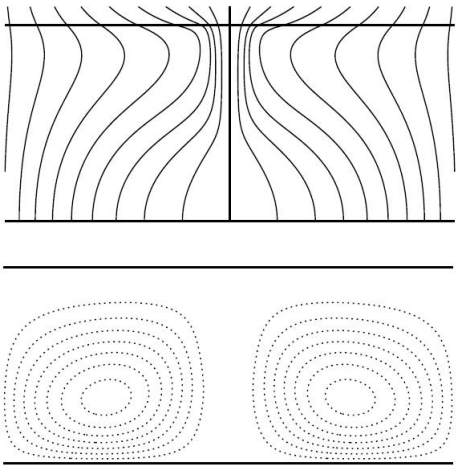

Figure 5.1: Magnetic (upper panel) and velocity (lower panel) field configuration resulting from magnetically quenching of turbulent heat transport (Kitchatinov & Mazur, 2000).

5.3 Reduced turbulent pressure

5.3.1 Principle

The effect of velocity fluctuations on the mean flow is, in its simplest form, captured by the Boussinesq assumption that relates the Reynolds stress tensor $\overline{u_i u_j}$ to the mean strain through a constant turbulent viscosity. This relation is of course in most cases far too simplified and there will be dependencies on the mean flow (such as the Λ-effect, Rüdiger (1980)) or the mean magnetic field (Rüdiger, 1974).

The effect of the presence of magnetic fluctuations can be modelled through a modification of the magnetic stress tensor. An analysis by Rüdiger et al. (1986) suggested a reduction of the total magnetic tension force by magnetic fluctuations. Kleeorin et al. (1990) came to a similar conclusion regarding the magnetic pressure and suggested that an instability resulting from this effective magnetic pressure reduction might well be able to create large scale magnetic flux concentrations, and perhaps even play an important role in the formation of sunspots.

The argument for the magnetic pressure reduction can be understood as follows. The turbulent pressure has both magnetic and kinetic contributions, in the case of isotropic turbulence one finds (Kleeorin & Rogachevskii, 1990; Rogachevskii & Kleeorin, 2007):

$$P_{\rm turb} = \frac{1}{3}\overline{\rho \mathbf{u}^2} e + \frac{1}{6}\overline{\mathbf{b}^2}/\mu_0. \tag{5.1}$$

It was shown numerically by Brandenburg et al. (2010) that for magnetic fields that are not too strong with respect to the equipartition value, the turbulent energy remains approximately constant. This can be expressed as

$$E_{\rm turb} = \frac{1}{2}\overline{\rho \mathbf{u}^2} + \frac{1}{2}\overline{\mathbf{b}^2}/\mu_0 \approx \text{const}. \tag{5.2}$$

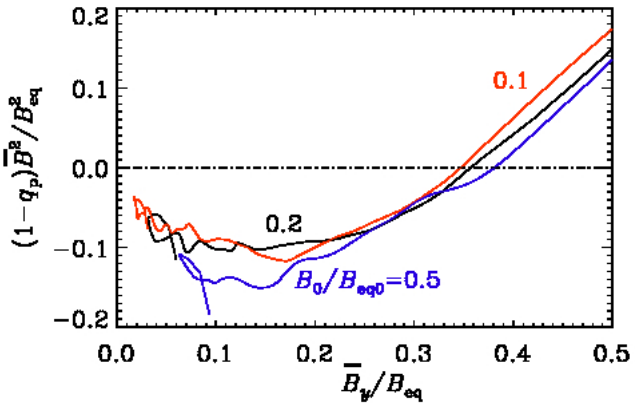

Figure 5.2: reduced magnetic pressure due to forced turbulence in a magnetised stratified medium, taken from **Paper I**.

Combining both expression gives:

$$P_{\rm turb} = \frac{1}{6}\overline{\mathbf{b}^2}/\mu_0 + \frac{2}{3}E_{\rm turb}. \tag{5.3}$$

This effect was predicted by analytical studies by Rogachevskii & Kleeorin (2007) and was also found numerically by Brandenburg et al. (2010) for forced turbulence in an unstratified medium. In **Paper I** we demonstrate the presence of a reduction and sign reversal of the effective magnetic pressure also in a stratified medium, see Figure 5.2. Similar results were later obtained by Käppylä et al. (2011) for turbulent convection.

From Equation (5.3) one sees that magnetic fluctuations have a negative feedback on the local pressure. This could cause a compression of the flow and with it a compression of the frozen in magnetic fields, leading to an increase of the local magnetic field strength. Assuming that the fluctuations are correlated with the mean field, there will be an even stronger reduction of the local pressure and an instability develops. Eventually saturation occurs when the magnetic field reaches values for which the pressure sign reversal disappears. Note that in the presence of a small scale dynamo, where magnetic fluctuations are generated even in the absence of a mean field, the pressure difference is reduced and the instability may not occur.

Thus far the negative effective magnetic pressure instability (NEMPI) has not been observed in direct numerical simulations, while mean-field computations do show certain structure formation in the magnetic field (Brandenburg et al., 2010), as also shown in Figure 5.3. To clarify the dichotomy between these results, a parameter study was conducted in **Paper II**. This analysis showed that for weak stratification or strong turbulent diffusion NEMPI is not triggered.

5.3.2 Mean-field model

As mentioned above, the effect of magnetic fluctuations is modelled as a feedback on the magnetic stress tensor. The current model is described by three turbulent transport co-

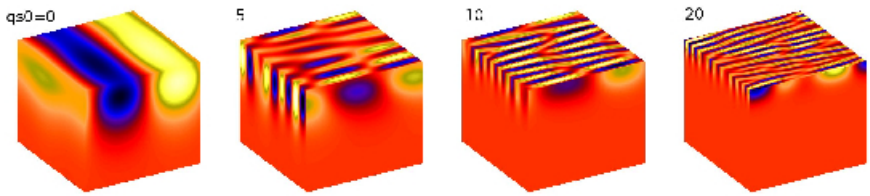

Figure 5.3: Magnetic flux concentration formation through NEMPI for different values from q_s, taken from **paper II**.

efficients: q_p is related to the magnetic pressure, q_s to the magnetic tension force and q_g to the interaction between the magnetic field and convection. In the direct simulations of **paper I**, the latter two coefficients were found to be zero within the measurement errors. The pressure reduction, shows a single dependence on the ratio of the mean field and the equipartition field strength $\overline{\boldsymbol{\beta}} = \overline{\mathbf{B}}/B_{eq}$, as shown in Figure 5.2. For the purpose of mean-field modelling a fit function of the form

$$P_M = \left(1 - q_{p0}\left[1 - \frac{2}{\pi}\arctan\left(\frac{\overline{\beta}^2}{\beta_p^2}\right)\right]\right)\overline{\beta}^2 \tag{5.4}$$

was used, where q_{p0} and β_p are model constants . However, it remains to be checked if the correct values for low magnetic fields, to which NEMPI has shown to be very susceptible, can be reproduced by this fit.

Chapter 6

Outlook

The findings of **Paper II** should now be interpreted in the context of **Paper I** and we will have to see if it is numerically possible to realise NEMPI in DNS, and whether NEMPI can be applicable to the parameter regime of the solar convection zone. Depending on the outcome, a proper continuation of our research would be the inclusion of radiative transfer into the model. Along the same line of thought, I would like to see if it is possible to confirm the results obtained by Kitchatinov & Mazur (2000), as discussed in Chapter 5, in DNS.

The continuation of **Paper IV** might include the application of the current model to a three-dimensional structure and/or changes in the model itself, this may be strongly affected by the questions sprouting from communications with the referees on our current work. It would be interesting to continue to explore the limitations of this mean-field model with respect to laboratory experiments.

Chapter 7

Contribution to the papers

In **Paper I** nearly all of the DNS simulations were performed and analysed by me. I played an active role in the discussion of the content of the text and in the adaptations following the referee reports. **Paper II** was built on mean-field simulations, which were performed and analysed by me. I wrote a few sections in the paper, although they were largely rewritten and extended by the senior coauthors. My contribution to **Paper III** was mostly through coding and participation in the analysis of the results as far as the validity of the method was concerned. **Paper IV** sprouted from a course project, and involved a fair amount of coding (initial and boundary conditions, modifications of existing equations), findings from these explorations were then more rigorously analysed by Axel, who also wrote most of the text in the paper.

Chapter 8

Acknowledgements

I would like to thank Axel for guiding my steps in this new environment, for his patience, for his contagious enthousiasm for really any scientific topic and in particular astrophysics.

Also thanks to my fellow PhD students, the astrophysics group - including the numerous visitors, for nice conversations, not always related to physics.

Thanks to a bunch of people at Nordita, the SU astronomy department and the KTH plasma physics group, for everything from administrative help to taking me along for Friday pizza.

Finally thanks to my family here in Sweden and in Belgium for being there for me and giving me a little push when needed.

Bibliography

Abbett, W.P., Fisher, G.H. & Fan, Y., 2000, ApJ, 540, 548-562

Abbett, W.P., Fisher, G.H., Fan, Y. & Bercik, D.J., 2004, ApJ, 612, 557-575

Babcock, H.W. & Babcock, H.D., 1955, ApJ, 121, 349

Babcock, H.W., 1961, ApJ, 133, 572

Balthasar, H., Schüssler, M. & Wöhl, H., 1982, Solar Phys., 76, 21-28

Balthasar, H., Vazquez, M. & Wöhl, H., 1986, A&A, 155, 87-98

Baumann, I. & Solanki, S.K, 2005, A&A, 443, 1061-1066

Beer, J., Blinov, A., Bonani, G., Hofmann, H. J., Finkel, R. C., 1990, Nature, 347, 164-166

Bhattacharjee, A. & Hameiri, E., 1986, Phys. Rev. Lett., 57, 206-209

Blackman, E.G. & Field, G.B., 2000, ApJ, 534, 984-988

Bodin, H., Nucl. Instr. & Meth. Phys. Res., 1983, 207, 1-22

Brandenburg, A., 2005, ApJ, 625, 539-547

Brandenburg, A., Haugen, N.E.L., Käpylä, P. & Sandin C., 2005, Astron. Nachr., 326, 174-185

Brandenburg, A., Kleeorin, N.& Rogachevskii, I., 2010, Astron. Nachr., 331, 5

Brandenburg, A. & Subramanian, K., 2005, Phys. Rep., 417, 1-209

Burbidge E.M., Burbidge, G.R., Fowler, W.A. & Hoyle, F., 1957, Rev. Mod. Phys., 29, 547-650

Carrington, R.C., 1858, MNRAS, 19, 1-3

Cattaneo, F., Brummel, N.H. & Cline, K.S., 2006, MNRAS, 365, 727-734

Chabrier, G. & Kker, M., 2006, A&A, 446, 1027-1037

Chandrasekhar, S., 1939, An introduction to the study of stellar structure (The University of Chicago press)

Charbonneau, P., 2005, Liv. Rev. Sol. Phys., 2

Charbonneau, P., Christensen-Dalsgaard, J., Henning, R., Larsen, R.M., Schou, J., Thompson, M.J. & Tomczyk, S., 1999, ApJ, 527, 445-460

Cheung, M.C.M., Rempel, M., Title, A.M. & Schssler, M., 2010, ApJ, 720, 233-244

Choudhuri, A.R. & Gilman, P.A., 1987, ApJ, 316, 788-800

Christensen-Dalsgaard, J., Gough, D. O. & Thompson, M. J., 1991, ApJ, 378, 413-437

Christensen-Dalsgaard, J., Gough, D.O. & Toomre, J., 1985, Science, 229, 923-931

Cowling, T.G., 1933, MNRAS, 94, 39-48

Dikpati, M. & Charbonneau, P., 1999, ApJ, 518, 508-520

Dikpati, M. & Gilman, P., 2001, ApJ, 559, 428-442

Eddington, A.S., 1920, Nature, 106, 14-20

Eddington, A.S., 1926, The Internal Constitution of the Stars (Cambridge University Press)

Eddy, J.A., 1976, Science, 192, 1189-1202

Elsasser, W.M., 1946, Phys. Rev., 69, 106-116

Fan, Y., Abbett, W.P. & Fischer, G.H., 2003, ApJ, 582, 1206-1219

Fan, X., Fischer, G.H. & DeLuca, E.E., 1993, ApJ, 405, 390-401

Gailitis, A., Lielausis, O., Platacis, E., Gerbeth, G. & Stefani, F., 2004, Phys. Plasmas, 11, 2838-2843

Giovanelli, R. G., 1982, Solar Phys., 80, 21-31

Gough, D.O., 1981, Solar Phys., 74, 21-34

Hale, G.E., 1908, ApJ, 28, 315

Hale, G.E., Ellerman, F., Nicholson, S. B. & Joy, A. H., 1919, ApJ, 49, 153

Hathaway, D.H., 2011, *arXiv:1102.0965*

Howard, R.F, 1996, Solar Phys., 296, 557

Hurlburt, N.E. & Rucklidge, A.M., 2000, MNRAS, 314, 793-806

Ivanova, T.S & Ruzmaikin, A.A., 1977, Sov. Astron., 21, 479-485

Ji, H. & Prager, S.C., 2002, Magnetohydrodyn. 38, 191-210

Käpylä, P.J., Brandenburg, A., Kleeorin, N., Mantere, M.J. & Rogachevskii, I., 2011, *arXiv:1102.0965*

Rüdiger, G., 2000, Solar Phys., 191, 325-340

Kitchatinov, L.L., Pipin, V.V. & Rüdiger, G., 1994, Astron. Nachr., 315, 157-170

Kleeorin, N., Moss, D. & Rogachevskii, I., 2000, A&A, 361, 5-8

Kleeorin, N. & Rogachevskii, I., 1990, in T.D. Guyenne and J.J. Hunt, ed. Noordwijk: European Space Agency Publication Division (21-23), Plasma Astrophysics, Proceedings of the European Space Agency Workshop, Telavi

Kleeorin, N., Rogachevskii, I. & Ruzmaikin, A.A. 1990, Sov. Phys. JETP, 70, 878

Kolmogorov A.N., 1941, Dokl. Akad. Nauk SSSR, 30, 301-305

Kosovichev, A.G., 1996, ApJ, 461, 55

Kosovichev, A.G., 2002, Astron. Nachr., 323, 186-191

Kosovichev, A.G., 2004, in A.V. Stepanov, E.E. Benevolenskaya, and A.G. Kosovichev, ed. Cambridge University Press (171-178), Multi-Wavelength Investigations of Solar Activity, IAU Symposium, Vol. 223

Kosovichev, A.G. & Stenflo, J.O., 2008, ApJ, 688, 115-118

Krause, F. & Rüdiger, G., 1975, Solar Phys., 42, 107-119

Larmor, J., 1919, Reports of the British Association for the Advancement of Science, 159-160

Leighton, R.B., 1969, ApJ, 156, 1

Li, K.J., Yun, H.S. & Gu, X.M., 2001, AJ, 122, 2115-2117

Linton, M.G., Longcope D.W. & Fischer, G.H., 1996, ApJ, 469, 954

Longcope, D.W., Linton, M., Pevtsov, A., Fisher, G. & Klapper, I., 1999, in M.R. Brown, R.C. Canfield and A.A. Pevtsov, ed. American Geophysical Union (93), Magnetic Helicity in Space and Laboratory Plasmas: Geophysical Monograph 111

Meyer, A., Schmidt, H.U. & Weiss, N.O., 1977, MNRAS, 179, 741-761

Monchaux, R., Berhanu, M., Aumatre, S., Chiffaudel, A., Daviaud, F., Dubrulle, B., Ravelet, F., Fauve, S., Mordant, N., Ptrlis, F., Bourgoin, M., Odier, P., Pinton, J.-F., Plihon, N. & Volk, R., 2009, Phys. Fluids, 21,

Moreno-Insertis, F. & Emonet, T., 1996, ApJ, 472, 53

Müller, U. & Stieglitz, R., 2002, Nonlin. Proc. Geophys., 9, 165-170

Nordlund, A., Brandenburg, A., Jennings, R.L., Rieutord, M., Ruokolainen, J., Stein, R.F. & Tuominen, I., 1992, ApJ, 392, 647-652

Ortolani, S., 1989, Plasma Phys. & Contr. Fus., 31, 1665-1684

Ossendrijver, M., 2003, A&A Rev., 11, 287-367

Parker, E.N., 1955, ApJ, 121, 491

Parker, E.N., 1975, Solar Phys., 40, 291-301

Parker, E.N., 1993, ApJ, 408, 707-719

Parker, E.N., 2009, Spa. Sci. Rev., 144, 15-24

Petrovay, K. & Moreno-Insertis, F., 1997, ApJ, 485, 398

Petrovay, K. & Van Driel-Gesztelyi, L., 1997, Solar Phys., 176, 249-266

Pouquet, A., Frisch, U. & Leorat, J., 1976, J. Fluid Mech., 77, 321-354

Rädler, K.-H., 1969, Geod. Geophys. Veröff., 131-135

Rempel, M., Schüssler, M. & Knölker, M., 2009, ApJ, 691, 640-649

Rheinhardt, M.& Brandenburg, A., 2010, A&A, 520, 28

Rogachevskii, I. & Kleeorin, N., 2007, Phys. Rev. E, 76,

Rüdiger, G., 1974, Astron. Nachr., 295, 275-284

Rüdiger, G., 1980, Geophys. Astrophys. Fluid Dyn., 16, 239-261

Rüdiger, G. & Brandenburg, A., 1995, A&A, 296, 557

Rüdiger, G. & Kitchatinov, L., 2000, Astron. Nachr., 321, 75-80

Rüdiger, G., Krause, F., Tuominen, I. & Virtanen, H., 1986, A&A, 166, 306-318

Ruzmaikin, A.A., Sokolov, D.D. & Shukurov, A.M., 1988, Magnetic fields of galaxies (Izdatel'stvo Nauka)

Scharmer, G., Nordlund, A. & Heinemann, T., 2008, ApJ, 677, 149-152

Schlichenmaier, R., Rezaei, R. & Bello Gonzalez, N., 2011, *arXiv:1102.0965*

Schou, J., Antia, H.M., Basu, S., Bogart, R.S., Bush, R.I., Chitre, S.M., Christensen-Dalsgaard, J., di Mauro, M.P., Dziembowski, W.A., Eff-Darwich, A., Gough, D.O., Haber, D.A., Hoeksema, J.T., Howe, R., Korzennik, S.G., Kosovichev, A.G., Larsen, R.M., Pijpers, F.P., Scherrer, P. H., Sekii, T., Tarbell, T.D., Title, A.M., Thompson, M.J. & Toomre, J., 1998, ApJ, 505, 390-417

Schrinner, M., Rädler, K.-H., Schmitt, D., Rheinhardt, M. & Christensen, U. , 2005, Astron. Nachr., 326, 245-249

Schrinner, M., Rädler, K.-H., Schmitt, D., Rheinhardt, M. & Christensen, U., 2007, Geophys. Astrophys. Fluid Dyn., 101, 81-116

Schüssler, M. & Vögler, A., 2006, ApJ, 641, 73-76

Schwabe, M., 1844, Astron. Nachr., 21, 233

Solanki, S.K., 2003, A&A Rev., 11, 152-286

Spence, E. J., Reuter, K. & Forest, C. B., 2009, ApJ, 700, 470-478

Spiegel, E.A. & Zahn, J.-P., 1992, A&A, 265, 106-114

Spörer, F.W.G., 1883, Astron. Nachr., 107, 331

Spörer, F.W.G., 1888, Astron. Nachr., 118, 307

Steenbeck, M., Krause, F. & Rädler, K.-H., Zeit. Naturforsch., 21, 369-376

Tassoul, J.L. & Tassoul, M., 2004, A concise history of solar and stellar physics (Princeton University Press)

Thelen, J.-C., 2000, MNRAS, 315, 165-183

Thompson, M.J., Christensen-Dalsgaard, J., Miesch, M.S. & Toomre, J., 2003, ARA&A, 599, 643

Usoskin, I. G., Mursula, K., Solanki, S., Schüssler, M. & Alanko, K., 2004, A&A, 413, 745-751

Vilhu, O., 1984, A&A, 133, 117-126

Westwood Oliver J.A., 1883, Or What Do We Owe to the Sun? a Popular Examination of the Cycle Theory of the Weather, Famines, Pestilences, Commercial Panics, Etc. (Kessinger Publishing)

Zappala, R.A. & Zuccarello, F., 1991, A&A, 242, 480-487

Zhao, J., Kosovichev, A.G. & Duvall, T.L., Jr., 2001, ApJ, 557, 384-388

I

DRAFT VERSION JULY 27, 2011
Preprint typeset using LaTeX style emulateapj v. 08/22/09

EFFECT OF STRATIFIED TURBULENCE ON MAGNETIC FLUX CONCENTRATIONS

AXEL BRANDENBURG, KOEN KEMEL
NORDITA, AlbaNova University Center, Roslagstullsbacken 23, SE-10691 Stockholm, Sweden;
Department of Astronomy, AlbaNova University Center, Stockholm University, SE-10691 Stockholm, Sweden

NATHAN KLEEORIN, IGOR ROGACHEVSKII
Department of Mechanical Engineering, Ben-Gurion University of the Negev, POB 653, Beer-Sheva 84105, Israel
(Revision: 1.162)
Draft version July 27, 2011

ABSTRACT

To understand the basic mechanism of the formation of magnetic flux concentrations, we determine by direct numerical simulations the turbulence contributions to the mean magnetic pressure in a strongly stratified isothermal layer, where a weak uniform horizontal mean magnetic field is applied. In a first setup, the *turbulent intensity* is nearly constant in height, so the kinetic energy density decreases with height due to the decrease in density, while in a second series of numerical experiments, the turbulent intensity increases with height such that the *kinetic energy density* is nearly independent of height. Turbulent magnetic diffusivity and turbulent pumping velocity are determined with the test-field method for both cases. Corresponding numerical mean-field models are used to assess whether or not a large-scale instability is to be expected. The existence of a negative effect of turbulence on the effective mean magnetic pressure is demonstrated for strongly stratified forced turbulence over a range values of magnetic Reynolds and Prandtl numbers. The vertical profile of the turbulent magnetic diffusivity is found to agree with what is expected based on simple mixing length expressions. Turbulent pumping is shown to be down the gradient of turbulent magnetic diffusivity, but it is twice as large as expected. Mean-field numerical modelling confirms the excitation of the instability for both setups, although no large-scale instability is found in the direct numerical simulations. Small-scale dynamo action is shown to reduce the negative effect of turbulence on the effective mean magnetic pressure.

Subject headings: MHD – Sun: magnetic fields – sunspots – Turbulence

1. INTRODUCTION

In a stratified layer, magnetic fields do not normally stay in equilibrium but tend to become buoyantly unstable (e.g. Newcomb 1961; Parker 1966, 1979a; Gilman 1970a,b; Hughes & Proctor 1988; Cattaneo & Hughes 1988; Wissink et al. 2000; Isobe et al. 2005; Kersalé et al. 2007), see also reviews by Hughes (2007) and Tobias & Weiss (2007). This mechanism is generally invoked in order to understand magnetic flux emergence at the solar surface (e.g. Hood et al. 2009). The mechanism does not explicitly rely upon the existence of turbulence, except that the origin of the Sun's magnetic field is generally believed to be related to a turbulent dynamo operating in the convection zone, or possibly beneath it; see Solanki et al. (2006) for a recent review.

Turbulent dynamos work under a variety of circumstances and are able to produce large-scale magnetic fields (see Brandenburg & Subramanian 2005 for a review). At first glance this generation process is counter-intuitive, because it works against the well-known concept of turbulent mixing (Taylor 1921; Prandtl 1925). However, it is now well established that turbulence can also cause non-diffusive effects. In addition to the well-known α effect that is generally believed to be responsible for the Sun's large-scale field (Moffatt 1978; Parker 1979b; Krause & Rädler 1980), there is also the Λ effect that is responsible for driving the differential rotation of the Sun (Rüdiger 1980, 1989; Rüdiger & Hollerbach 2004). Yet another import effect is turbulent pumping or γ effect (Rädler 1969), which corresponds to the advection of mean magnetic field that is not associated with any material motion. The γ effect appears, for example, in nonuniform turbulence and transports mean magnetic field down the gradient of turbulent intensity, which is usually downward in turbulent convection. However, this effect can also be modified by the mean magnetic field itself (Kitchatinov et al. 1994; Rogachevskii & Kleeorin 2006), which can then correspond to a mean-field buoyancy effect.

When invoking the concept of magnetic buoyancy, one must ask what the effect of turbulence is in this context. The turbulent pressure associated with the convective fluid motions and magnetic fluctuations is certainly not negligible and reacts sensitively to changes in the background magnetic field. The main reason for this is that the kinetic energy density in isotropic turbulence contributes to the total turbulent dynamic pressure twice as much as turbulent magnetic energy density, i.e.

$$P_{\rm turb} = \tfrac{1}{3}\overline{\rho \boldsymbol{u}^2} + \tfrac{1}{6}\overline{\boldsymbol{b}^2}/\mu_0. \quad (1)$$

Here, $P_{\rm turb}$ is the total turbulent dynamic pressure caused by velocity and magnetic fluctuations, $\boldsymbol{u}$ and $\boldsymbol{b}$, respectively, μ_0 is the vacuum permeability, ρ is the fluid density, and overbars indicate ensemble averaging. On the other hand, any rise in local turbulent magnetic energy density must be accompanied by an equal and opposite change of turbulent kinetic energy density in order to obey approximate energy conservation, i.e.

$$\tfrac{1}{2}\overline{\rho \boldsymbol{u}^2} + \tfrac{1}{2}\overline{\boldsymbol{b}^2}/\mu_0 \equiv E_{\rm tot} \approx {\rm const}. \quad (2)$$

This relation is known to hold quite well even in open systems with boundaries, as was demonstrated by direct numerical simulations (Brandenburg et al. 2010, hereafter referred to as BKR). This clearly implies that, upon generation of magnetic fluctuations, the total turbulent dynamic pressure shows

a reversed (destabilizing) feedback, i.e.

$$P_{\rm turb} = -\tfrac{1}{6}\overline{\boldsymbol{b}^2}/\mu_0 + {\rm const}, \quad (3)$$

where the constant is $2E_{\rm tot}/3$ (Kleeorin et al. 1990). For strongly anisotropic turbulence, Eq. (3) is also valid except for the change of the $1/6$ factor into $1/2$ (Rogachevskii & Kleeorin 2007), hereafter referred to as RK07. This phenomenology was supported by analytical studies using the spectral τ approximation and the renormalization approach and led Kleeorin & Rogachevskii (1994) to the realization that the effective mean magnetic pressure force is reduced and can be reversed for certain mean magnetic field strengths (see also Kleeorin et al. (1990)). Under certain conditions (e.g. strong density stratification), this can cause a magnetic buoyancy instability via perturbations of a uniform mean magnetic field in stratified turbulence (Kleeorin et al. 1993, 1996). Later, when considering the effect of turbulent convection on the mean Lorentz force, RK07 suggested that magnetic flux concentrations in the Sun such as active regions and even sunspots might be formed by this reversed feedback effect.

Contrary to a statement by Spruit (2011), the effect of turbulence on the mean Lorentz force cannot be understood solely in terms of turbulent magnetic diffusion. Turbulence has two main effects. Firstly, it creates inhomogeneous magnetic structures by the reversed feedback effect, and secondly, it acts in the opposite way by destroying magnetic flux concentrations through turbulent magnetic diffusion.

The basic phenomenon of magnetic flux concentration by the effect of turbulence on the mean Lorentz force has been recently confirmed numerically by BKR who solved the mean-field momentum and induction equations and found a linear instability for sufficiently strong stratification. This instability was followed by nonlinear saturation at near-equipartition strengths.

Using direct numerical simulations (DNS) of forced turbulence, BKR also verified the validity of the phenomenology highlighted by Eq. (3). However, their DNS ignored the effects of stratification which would lead to additional effects such as turbulent pumping that might oppose the instability.

Extending the DNS of BKR to the case with stratification is therefore one of the main goals of the present paper. This will allow us for the first to make a meaningful comparison between DNS in stratified fluid with mean-field modeling. We are now also able to present data for cases where small-scale dynamo action is possible. An additional aim is to clearly demonstrate the operation of the instability directly in a three-dimensional turbulence simulation. One might then expect to see the spontaneous formation of long-lived magnetic flux concentrations. The effects of convection will be addressed in a companion paper (Käpylä et al. 2011).

Most of the numerical simulations on magnetic flux emergence (e.g. Stein & Nordlund 2001; Schüssler & Vögler 2006; Martínez et al. 2008; Rempel et al. 2009) have been done using initial conditions with an already existing strongly inhomogeneous large-scale magnetic field. Recent simulations by BKR and Kitiashvili et al. (2010); Käpylä et al. (2011) study the formation of large-scale magnetic structures from an initially uniform large-scale magnetic field. In particular, Large-Eddy Simulations of solar magneto-convection by Kitiashvili et al. (2010) do already give indications that the spontaneous formation of long-lived magnetic flux concentrations from initial uniform magnetic field might be possible, although the underlying mechanism in their simulations still remains to be clarified. One of the differences compared with BKR is the vertical orientation of the imposed magnetic field in turbulent convection. In forced and convection-driven turbulence simulations of BKR and Käpylä et al. (2011), respectively, the imposed magnetic field was a horizontal one. A similar type of magnetic flux concentration has been seen in convection simulations at large aspect ratios by Tao et al. (1998), which show a segregation into magnetized and weakly magnetized regions.

Other possibilities for causing flux concentrations include turbulent thermal collapse, whereby the magnetic field suppresses the convective energy flux, leading to local cooling, and thus to contraction and further enhancement of magnetic flux (Kitchatinov & Mazur 1988). By considering isothermal stratified flow, we will exclude this possibility in our present work, allowing thus a more definitive identification of the effect of density-stratified turbulence on the mean Lorentz force.

2. DNS MODEL AND ANALYSIS

We consider a cubic computational domain of size L^3. The smallest wavenumber is then $k_1 = 2\pi/L$. We adopt an isothermal equation of state with constant sound speed $c_{\rm s}$, so the gas pressure is $p = \rho c_{\rm s}^2$. In the presence of gravity, $\boldsymbol{g} = (0, 0, -g)$, where g is the constant gravitational acceleration, this leads to an exponentially stratified density,

$$\rho = \rho_0 \exp(-z/H_\rho), \quad (4)$$

with a constant density scale height $H_\rho = c_{\rm s}^2/g$ and a normalization factor ρ_0. For all our calculations we choose $k_1 H_\rho = 1$. This implies that the number of scale heights is $\Delta \ln \rho = L/H_\rho = 2\pi$, corresponding to a density contrast of $\exp 2\pi \approx 535$. This state is also chosen as our initial condition.

We solve the equations of compressible magneto-hydrodynamics in the form

$$\rho \frac{{\rm D}\boldsymbol{U}}{{\rm D}t} = \boldsymbol{J} \times \boldsymbol{B} - c_{\rm s}^2 \boldsymbol{\nabla}\rho + \boldsymbol{\nabla} \cdot (2\nu\rho \mathsf{S}) + \rho(\boldsymbol{f} + \boldsymbol{g}), \quad (5)$$

$$\frac{\partial \boldsymbol{A}}{\partial t} = \boldsymbol{U} \times \boldsymbol{B} + \eta \nabla^2 \boldsymbol{A}, \quad (6)$$

$$\frac{\partial \rho}{\partial t} = -\boldsymbol{\nabla} \cdot \rho \boldsymbol{U}, \quad (7)$$

where ν and η are kinematic viscosity and magnetic diffusivity, respectively, $\boldsymbol{B} = \boldsymbol{B}_0 + \boldsymbol{\nabla} \times \boldsymbol{A}$ is the magnetic field consisting of a uniform mean field, $\boldsymbol{B}_0 = (0, B_0, 0)$, and a nonuniform part that is represented in terms of the magnetic vector potential $\boldsymbol{A}$, $\boldsymbol{J} = \boldsymbol{\nabla} \times \boldsymbol{B}/\mu_0$ is the current density, and $\mathsf{S}_{ij} = \frac{1}{2}(U_{i,j} + U_{j,i}) - \frac{1}{3}\delta_{ij} \boldsymbol{\nabla} \cdot \boldsymbol{U}$ is the traceless rate of strain tensor, where commas denote partial differentiation. The turbulence is driven with a forcing function $\boldsymbol{f}$ that consists of random plane non-polarized waves with an average wavenumber $k_{\rm f} = 5\, k_1$. The forcing strength is arranged such that the turbulent rms velocity, $u_{\rm rms} = \langle \boldsymbol{u}^2 \rangle^{1/2}$, is around $0.1\, c_{\rm s}$. This value is small enough so that compressibility effects are confined to those associated with stratification alone.

Our simulations are characterized by several non-dimensional parameters. We define the Reynolds number as ${\rm Re} = u_{\rm rms}/\nu k_{\rm f}$ and the magnetic Prandtl number as ${\rm Pr}_M = \nu/\eta$. We anticipate that it is important to have ${\rm Pr}_M < 1$. However, in order to reach somewhat larger values of ${\rm Re}_M$ we now choose as our primary model ${\rm Pr}_M = 0.5$ instead of 0.25, as

was the case in BKR. In some additional cases, we span the entire range from $\mathrm{Pr}_M = 1/8$ to $\mathrm{Pr}_M = 8$. For large enough values of Re_M and Pr_M, there is small-scale dynamo action. We define the equipartition field strength both as a function of z and for the middle of the domain, i.e.

$$B_{\rm eq}(z) = (\mu_0 \overline{\rho \boldsymbol{u}^2})^{1/2}, \quad B_{\rm eq0} = (\mu_0 \rho_0)^{1/2}\, u_{\rm rms}. \quad (8)$$

The latter will be used to specify the normalized strength of the imposed horizontal field, which is also independent of height. Another alternative is to normalize by the equipartition field strength at the top of the domain. In our models with nearly height-independent turbulent velocity, this would make the imposed field strength normalized by the equipartition value at the top ≈ 5 times bigger.

In all cases we adopt stress-free perfect conductor boundary conditions at top and bottom of the domain. The simulations are performed with the PENCIL CODE[1], which uses sixth-order explicit finite differences in space and a third-order accurate time stepping method (Brandenburg & Dobler 2002). We use a resolution of either 128^3 or 256^3 mesh points.

In this paper we present two groups of runs. In the first group we have the same forcing amplitude at all heights while in the second group we adjust the forcing such that the rms velocity becomes height-dependent. In contrast to earlier work where it was possible to analyze the results in terms of volume averages, we now have to restrict ourselves to horizontal averages which show a strong dependence on height. Thus, we determine the contribution to the mean momentum density that comes from the fluctuating field, i.e.,

$$\overline{\Pi}^{\rm f}_{ij} = \overline{\rho}\,\overline{u_i u_j} + \tfrac{1}{2}\delta_{ij}\overline{\boldsymbol{b}^2} - \overline{b_i b_j}, \quad (9)$$

where the μ_0 factor is dropped from now on and overbars indicate xy averages. The superscript f signifies the contributions from the small-scale field. This, together with the contribution from the mean field,

$$\overline{\Pi}^{\rm m}_{ij} = \overline{\rho}\,\overline{U}_i\overline{U}_j + \delta_{ij}\left(\overline{p} + \tfrac{1}{2}\overline{\boldsymbol{B}}^2\right) - \overline{B}_i\overline{B}_j - 2\nu\overline{\rho}\,\overline{\mathsf{S}}_{ij}, \quad (10)$$

comprises the total mean momentum tensor, and the averaged momentum equation is given by:

$$\frac{\partial}{\partial t}\overline{\rho}\,\overline{\boldsymbol{U}}_i = -\nabla_j\left(\overline{\Pi}^{\rm f}_{ij} + \overline{\Pi}^{\rm m}_{ij}\right) + \overline{\rho}\,g_i. \quad (11)$$

Here $\overline{\boldsymbol{U}}$ and $\overline{\boldsymbol{B}}$ are the mean velocity and magnetic fields, $\overline{p}$ is the mean fluid pressure. We are interested in the contribution to Eq. (9) that arises only in the presence of the mean field, so we subtract the corresponding tensor components that are obtained in the absence of the mean field and make for this the ansatz (RK07)

$$\overline{\Pi}^{{\rm f},\overline{B}}_{ij} - \overline{\Pi}^{{\rm f},0}_{ij} = -\left(\tfrac{1}{2}q_{\rm p}\delta_{ij} + q_{\rm g}\hat{g}_i\hat{g}_j\right)\overline{B}^2 + q_{\rm s}\overline{B}_i\overline{B}_j, \quad (12)$$

where $\hat{\boldsymbol{g}}$ is a unit vector in the vertical direction. Equation (12) can even be obtained from symmetry arguments, i.e., in the case of a horizontal imposed field, the linear combination of three independent true tensors, δ_{ij}, $\hat{g}_i\hat{g}_j$ and $\overline{B}_i\overline{B}_j$, yields ansatz (12). In the theory, the coefficients $q_{\rm p}$, $q_{\rm s}$ and $q_{\rm g}$ have been obtained using the spectral τ approach and the renormalization approach. The τ approach has been justified in a number of numerical simulations (Brandenburg et al. 2004; Brandenburg & Subramanian 2005b, 2007). However, if there is insufficient scale separation, higher order terms such as $\overline{J}_i\overline{J}_j$ would need to be included. Such terms are not presently included with the uniform fields used in the present study.

The effective mean Lorentz force that takes into account the turbulence effects, reads:

$$\overline{\rho}\,\overline{\boldsymbol{\mathcal{F}}}^{\rm M}_i = -\nabla_j\Big(\tfrac{1}{2}\overline{B}^2\delta_{ij} - \overline{B}_i\overline{B}_j + \overline{\Pi}^{{\rm f},\overline{B}}_{ij} - \overline{\Pi}^{{\rm f},0}_{ij}\Big). \quad (13)$$

Except for the contribution proportional to $\hat{g}_i\hat{g}_j$ and the fact that we use here only horizontal averages, Eq. (12) is equivalent to that used in BKR, where full volume averages were used. Asymptotic expressions for the $\overline{B}$ dependence of $q_{\rm p}$, $q_{\rm s}$, and $q_{\rm g}$ are given in Appendix A. Here we use DNS of density-stratified turbulence to determine these coefficients. In the present case, we have $\overline{\boldsymbol{B}} \approx (0, \overline{B}, 0)$,

$$\begin{aligned}
\overline{\rho}\,(\overline{u_x^2} - \overline{u_{0x}^2}) + \tfrac{1}{2}(\overline{\boldsymbol{b}^2} - \overline{\boldsymbol{b}_0^2}) - \overline{b_x^2} + \overline{b_{0x}^2} &= -\tfrac{1}{2}q_{\rm p}\overline{B}^2, \quad (14)\\
\overline{\rho}\,(\overline{u_y^2} - \overline{u_{0y}^2}) + \tfrac{1}{2}(\overline{\boldsymbol{b}^2} - \overline{\boldsymbol{b}_0^2}) - \overline{b_y^2} + \overline{b_{0y}^2} &= -(\tfrac{1}{2}q_{\rm p} - q_{\rm s})\overline{B}^2,\\
\overline{\rho}\,(\overline{u_z^2} - \overline{u_{0z}^2}) + \tfrac{1}{2}(\overline{\boldsymbol{b}^2} - \overline{\boldsymbol{b}_0^2}) - \overline{b_z^2} + \overline{b_{0z}^2} &= -(\tfrac{1}{2}q_{\rm p} + q_{\rm g})\overline{B}^2,
\end{aligned}$$

where we have taken into account that there is a small-scale dynamo, which would have produced finite background magnetic fluctuations $\boldsymbol{b}_0$. The critical magnetic Reynolds number for small-scale dynamo action is around 100. To derive Eqs. (14) we used Eqs. (9) and (12).

3. RESULTS

3.1. *Effective mean magnetic pressure*

We begin by considering the turbulence effects on the effective mean magnetic pressure and plot in Fig. 1 the dependence of $q_{\rm p}$ on height. To improve the statistics, we present here time averaged results of $q_{\rm p}$, which itself is already averaged over x and y. Error bars have been calculated by dividing the time series into three equally long pieces and computing the maximum departure from the total average. In agreement with earlier work, this function is always positive and exceeds unity if the mean magnetic field is not sufficiently strong. This is the case primarily at the bottom of the domain (negative values of z) where the density is high and therefore the magnetic field, in units of the equipartition field strength, is weak. Furthermore, since $B_0 = \mathrm{const}$ and $B_{\rm eq}$ increases with depth, $B_0/B_{\rm eq}$ is smallest at the bottom, so $q_{\rm p}$ increases. The sharp uprise toward the boundary is just a result of the exponential increase of the density combined with the fact that the horizontal velocity reach a local maximum on the boundary.

The total effective magnetic pressure of the mean field (that takes into account the effects of turbulence on the mean Lorentz force) is given by $\frac{1}{2}[1 - q_{\rm p}(\overline{B})]\overline{B}^2$. This has to be compared with the turbulent kinetic energy density, $\frac{1}{2}\overline{\rho\boldsymbol{u}^2}$. Small contributions of terms $\propto q_{\rm g}$ to the effective mean magnetic pressure are discussed in Sect. 3.3. In Fig. 2 we plot $(1 - q_{\rm p})\overline{B}^2/B_{\rm eq}^2$, where $B_{\rm eq}^2$ is itself in general a function of height; see Eq. (8). It turns out that this function now reaches a negative minimum somewhere in the middle of the domain.

We expect that $q_{\rm p}$ is a function of the ratio of $\overline{B}/B_{\rm eq}$. This was confirmed numerically in BKR for constant $B_{\rm eq}$ by varying the value of B_0 to obtain $q_{\rm p}$ for a range of different simulations. In the present case, however, $B_{\rm eq}$ is a function of z, which is the main reason why $q_{\rm p}$ depends on height. It turns out that the dependence of $q_{\rm p}$ on both $\overline{B}$ and z can be reduced to a single dependence just on the ratio $\overline{B}/B_{\rm eq}$. This is shown

[1] `http://pencil-code.googlecode.com`

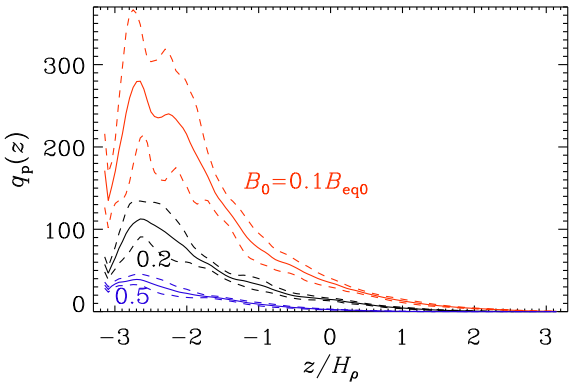

FIG. 1.— Dependence of $q_p(z)$ (solid lines) with error margins (dashed lines) as functions of z, for $B_0 = 0.1B_{eq0}$, $B_0 = 0.2B_{eq0}$, and $B_0 = 0.5B_{eq0}$, with Re $= 70$, $g/c_s^2 k_1 = 1$, and a density contrast of 530. Note that $q_p(z)$ reaches a maximum at the bottom of the domain where $B_0/B_{eq}(z)$ is minimum.

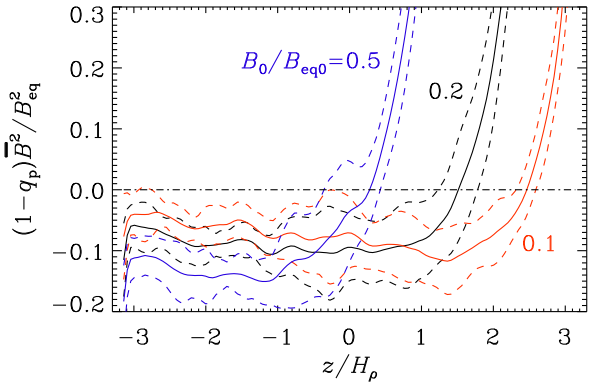

FIG. 2.— Normalized effective mean magnetic pressure as a function of depth, for $B_0 = 0.1B_{eq0}$, $B_0 = 0.2B_{eq0}$, and $B_0 = 0.5B_{eq0}$ using Re $=$ 70. Note that this function now reaches a negative minimum somewhere in the middle of the domain.

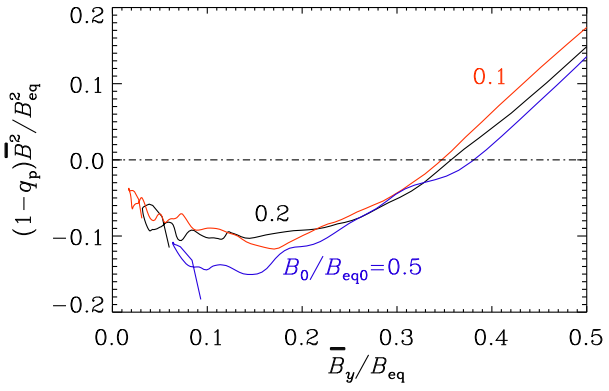

FIG. 3.— Same as Fig. 2, but as a parametric representation as function of the local value of the ratio of $B_0/B_{eq}(z)$. Note that the curves for $B_0 = 0.1B_{eq0}$, $B_0 = 0.2B_{eq0}$, and $B_0 = 0.5B_{eq0}$ collapse onto a single dependency. The error range is not shown, but the width of the error margin of the normalized effective mean magnetic pressure is generally below 0.05.

in Fig. 3, where we plot the effective mean magnetic pressure as a function of magnetic field in units of the local equipartition value. Note that now all three curves for different values of $\overline{B}$ collapse onto a single curve.

In the earlier DNS of BKR we described the results using a simple fit formula,

$$q_p = q_{p0}\left(1 - \frac{2}{\pi}\arctan\frac{\overline{B}^2}{B_p^2}\right). \quad (15)$$

Unfortunately, this formulation gives reasonably good fits for a range of different combinations of q_{p0} and B_p. Therefore, we now give the two new fit parameters, the value of the minimum effective pressure,

$$P_m(\overline{B}) = (1-q_p)\overline{B}^2/B_{eq}^2, \quad (16)$$

as well as the positions of the minimum and the transition through zero, defined by

$$P_m(\overline{B}_*) = \min(P_m), \quad \text{and} \quad P_m(\overline{B}_{crit}) = 0. \quad (17)$$

The resulting minimum of the effective magnetic pressure is now smaller than the value found in the DNS of BKR. Nevertheless, it it remarkable that these two rather different simulations still agree reasonably well and produce a minimum of the effective pressure that is compatible with what is expected from the τ approximation results of RK07. This is shown in Table 1, where we compare the results for $\min(P_m)$ and $\overline{B}_{crit}/B_{eq}$ with those of BKR and RK07. The fact that nearly the same functional form for the effective magnetic pressure of the mean field is obtained, supports the idea that this effect is robust.

We reiterate that, as long as the value of the plasma beta (i.e. the ratio of gas pressure to magnetic pressure), is much larger than unity, our results are independent of the plasma beta. What matters is the ratio of magnetic energy density to kinetic energy density, not the thermal energy density. This is also clear from the equations given in Appendix A. In the present simulations, the plasma beta varies from between 5 and 100 at the top to around 10^5 at the bottom, so the total pressure (gas plus magnetic plus turbulent pressure) is clearly positive.

3.2. *Equipartition versus pumping*

It turns out that most of the variability of the magnetic field occurs near the bottom of the computational domain. This is evident from Fig. 4, where we show visualizations of the y component of the departure from the imposed field, $B_y - B_0$, on the periphery of the domain for runs with $B_0/B_{eq0} = 0.1$, 0.2, and 0.5.

An obvious reason why most of the magnetic field variation occurs near the bottom of the computational domain is

TABLE 1
COMPARISON OF THE PRESENT SIMULATIONS WITH BKR AND RK07.

	Pr_M	Re_M	$\overline{B}_{crit}/B_{eq}$	$-\min(P_m)$
RK07			0.33	0.04
BKR	1/4	45	0.65	0.38
present	1/4	70	0.36	0.15
present	1	70	0.28	0.07
present	4	70	0.16	0.01

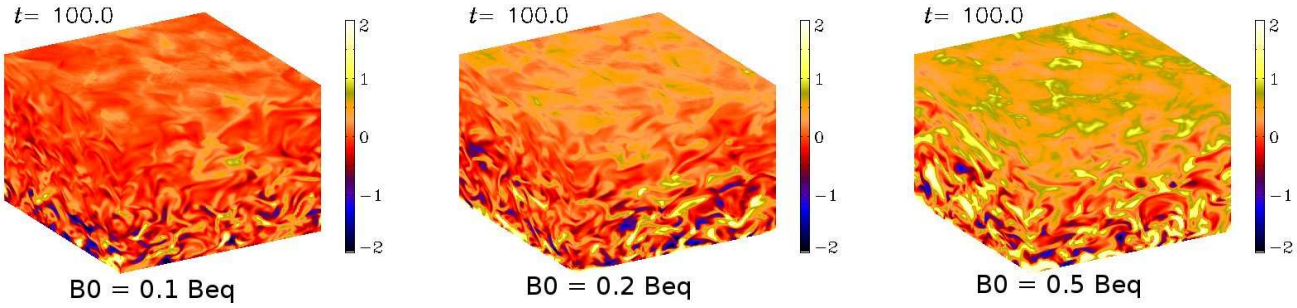

FIG. 4.— Visualization of $(B_y - B_0)/B_{\rm eq}$ on the periphery of the computational domain for runs with $B_0/B_{\rm eq0} = 0.1$, 0.2, and 0.5, with Re $= 70$.

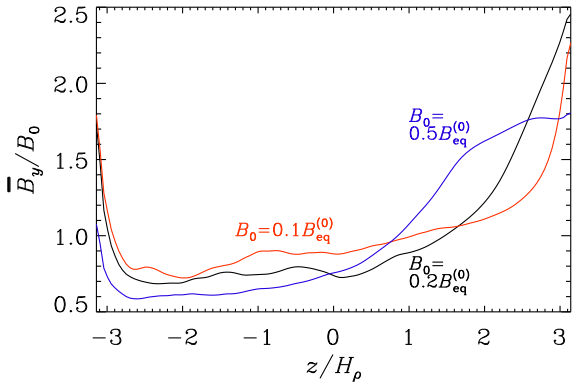

FIG. 5.— Normalized mean magnetic field in the direction of the imposed field versus height for $B_0 = 0.1B_{\rm eq0}$, $0.2B_{\rm eq0}$, and $0.5B_{\rm eq0}$ with Re $=$ 70.

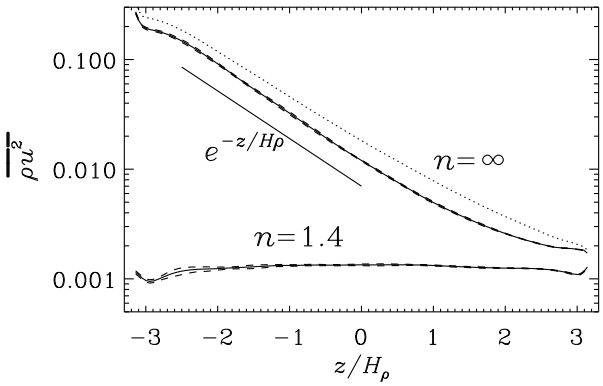

FIG. 6.— Turbulent kinetic energy density versus height for $n = \infty$ for $B_0 = 0$ (dotted line) and $B_0 = 0.2B_{\rm eq0}$ compared with the case for $n = 1.4$ and $B_0 = 0.2B_{\rm eq0}$.

related to the local value of the equipartition field strength, $B_{\rm eq}$, which is proportional to $\rho^{1/2}$. Therefore, $B_0/B_{\rm eq}$, is large in the upper parts, so it will be less easy for the turbulence to produce strong fluctuations due to the enhanced work done against the Lorentz force. By contrast, in the lower parts $B_0/B_{\rm eq}$ is small, allowing magnetic fluctuations to be produced.

The vertical dependence of the horizontally averaged mean magnetic field (now normalized to $B_0 = {\rm const}$) is shown in Fig. 5. We see that, especially for intermediate field strengths, there is an increase of the magnetic field near the top of the domain. One possibility is that this is caused by the effect of nonlinear turbulent pumping, which might cause the mean field to be pumped up due to the gradients of the mean turbulent kinetic energy density in the presence of a finite mean magnetic field (cf. Rogachevskii & Kleeorin 2006). This type of pumping is different from the regular pumping down the gradient of turbulent intensity (Rädler 1969). To compensate for this effect, we have produced additional runs where the kinetic energy density is approximately constant with height. This is achieved by modulating the forcing function by a z-dependent factor $e^{z/H_{\rm f}}$. We define $n = H_{\rm f}/H_\rho$ and find that for $n = 1.4$ the kinetic energy density is approximately independent of height; see Fig. 6.

As a consequence of reducing the turbulent driving in the lower parts by having $B_{\rm eq}(z) \approx {\rm const}$, we allow the magnetic field to have almost the same energy density as the turbulence, i.e. $B_0/B_{\rm eq}(z)$ is approximately independent of z. This also means that the fluctuations are now no longer so pronounced at the bottom of the domain (Fig. 7), where Re drops to values around 5 and the flow is no longer turbulent. However, at the top the Reynolds number is around 120, so here the flow is still turbulent. In Fig. 8 we show the vertical dependence of the horizontally averaged mean magnetic field in units of the imposed field strength. Note that now the field shows an increase toward the bottom of the domain. This effect might be related to regular turbulent pumping (Rädler 1969), which now has a downward component because $\overline{\boldsymbol{u}^2}$ decreases with depth. We return to this issue further below.

In the runs shown above we used ${\rm Pr}_M = 1/2$. As expected from earlier work of BK07, the negative magnetic pressure effect should be most pronounced at small ${\rm Pr}_M$. This is indeed confirmed by comparing with larger and smaller val-

TABLE 2
${\rm Pr}_M$ DEPENDENCE FOR ${\rm Re}_M = 35$, 70, AND 130.

	$B_{\rm rms}/\overline{B}_y$			$\overline{B}_{\rm crit}/B_{\rm eq}$			$-\min(P_{\rm m})$		
${\rm Pr}_M\backslash{\rm Re}_M$	35	70	130	35	70	130	35	70	130
1/8			0.3			0.28			0.07
1/4		2.4	6.2		0.36	0.25		0.15	0.05
1/2		4.5	7.1		0.34	0.25		0.10	0.05
1	0	5.4		unc.	0.28		0.17	0.07	
2	0	5.9		0.24	0.22		0.09	0.03	
4	0	5.8		0.20	0.16		0.02	0.01	
8	0	3.5		n.r.	0.12		n.r.	0.01	

'unc.' means result is uncertain, 'n.r.' means no sign reversal of $q_{\rm p}$.

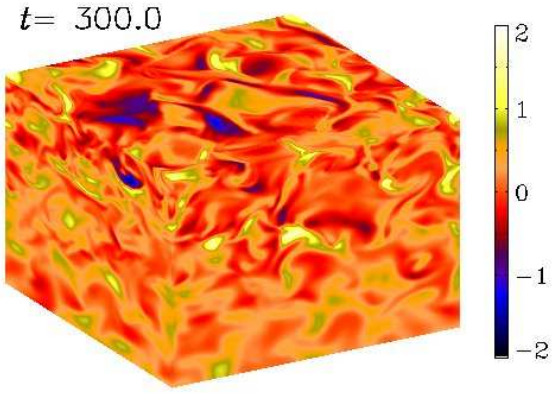

FIG. 7.— Visualization of $(B_y - B_0)/B_{\rm eq}$ on the periphery of the computational domain for the run with nearly uniform turbulent kinetic energy density using $H_{\rm f} = nH_\rho$ with $n = 1.4$.

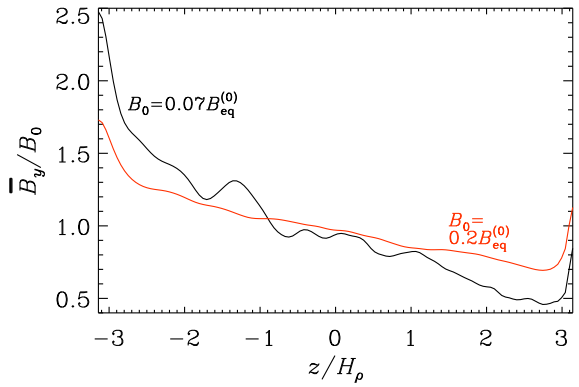

FIG. 8.— Normalized mean magnetic field in the direction of the imposed field versus height in the case of nearly constant turbulent kinetic energy density, i.e. $B_{\rm eq}(z) \approx$ const.

ues of Pr_M; see Fig. 9 and Table 2. For these runs we have again constant turbulent intensity with height ($n \to \infty$), similar to those of Fig. 4. A snapshot of the magnetic field for $\mathrm{Pr}_M = 1/8$, $\mathrm{Re}_M = 130$, and a resolution of 256^3 mesh points is shown in Fig. 10, where we see intense small-scale distortions of the field at the bottom and weaker large-scale patches at the top. It is however unclear whether this is related to the expected reduction of turbulent pressure by the mean field.

3.3. *Resolution dependence*

A density contrast of over 500 may seem rather large (Cattaneo et al. 1991). However, this impression may derive from experience with polytropic models, where most of the density variation occurs near the surface. In our isothermal model, the scale height is constant, so the logarithmic density change is independent of height. In Fig. 11 we demonstrate by explicit comparison that simulations with 128^3 and 256^3 mesh points give nearly the same result.

3.4. *Coefficients $q_{\rm s}$ and $q_{\rm g}$*

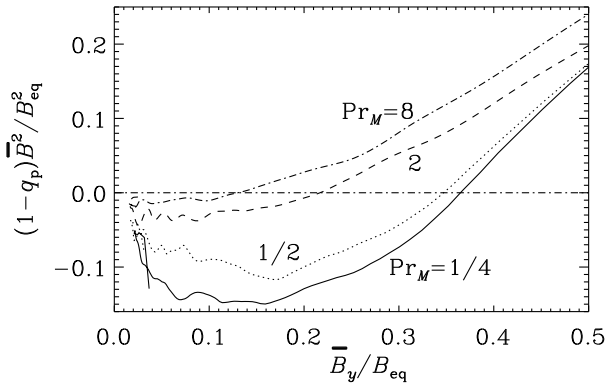

FIG. 9.— Normalized effective mean magnetic pressure for different values of Pr_M, where Re_M is approximately 70 and $B_0 = 0.1B_{\rm eq0}$.

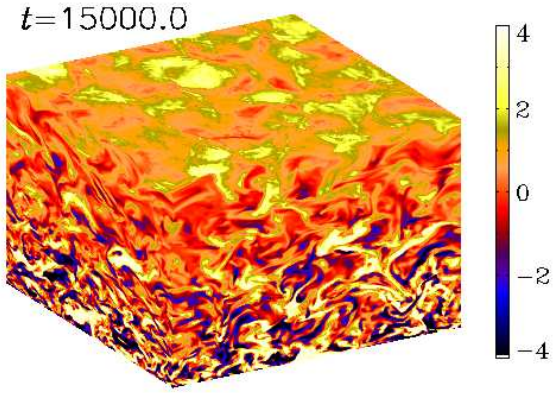

FIG. 10.— Visualization of $(B_y - B_0)/B_{\rm eq}$ on the periphery of the computational domain for a run with $B_0/B_{\rm eq0} = 0.1$, $\mathrm{Pr}_M = 1/8$, $\mathrm{Re}_M = 130$, $\mathrm{Re} = 1000$ at a resolution of 256^3 mesh points.

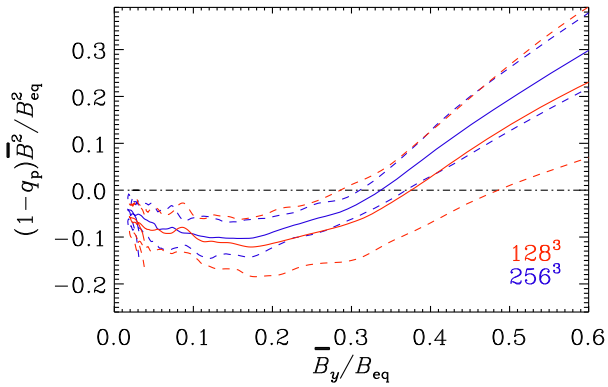

FIG. 11.— Resolution dependence of $q_{\rm p}(\overline{B}_y/B_{\rm eq})$ for $\mathrm{Pr}_M = 1/2$, $\mathrm{Re}_M = 70$ using 128^3 and 256^3 mesh points. Error bars are given by the shaded areas.

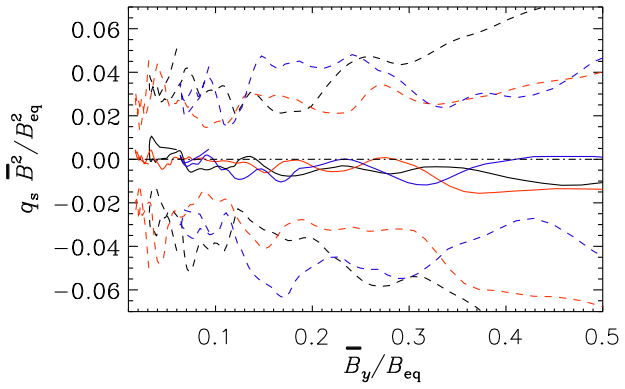

FIG. 12.— Similar to Fig. 3, but for $q_s\overline{\boldsymbol{B}}^2/B_{eq}^2$ and now as a function of $\overline{B}_y/B_{eq}$. Within the error range (dashed lines), $q_s=0$ for all field strengths.

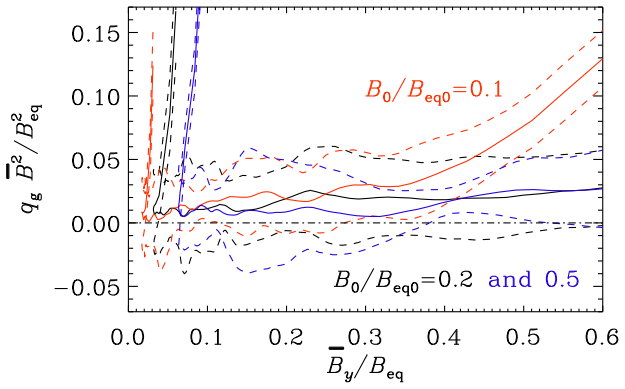

FIG. 13.— Similar to Fig. 12, but for q_g. Note that q_g attains positive values for $B_0/B_{eq}=0.1$.

Using Eqs. (14), we now determine q_s and q_g. The results are shown in Figs. 12 and 13 for the three imposed field strengths considered above, where $\overline{\boldsymbol{u}}^2$ was nearly independent of z, so $B_{eq}(z)$ varied by a factor of $\exp\pi\approx23$, allowing us to scan the dependence on $\overline{B}/B_{eq}$ in a single run. It turns out that both q_s and q_g are around zero.

Comparing with BKR, we should point out that they found q_g always to be zero, because the turbulence was isotropic in the plane perpendicular to the direction of the imposed field. On the other hand, recent calculations of stratified convection with an imposed horizontal magnetic field did indeed yield non-vanishing (positive) values of q_g (Käpylä et al. 2011). More recent calculations of q_g from stratified convection, on the other hand, confirm that $q_g\overline{\boldsymbol{B}}^2/B_{eq}^2$ is indeed different from zero and around 0.4. In the present study with vertical density stratification, q_g is much smaller, but generally positive. This appears to be in conflict with the theoretical expectation for q_g given in Appendix A, where $q_g=O(\ell_f^2/H_\rho^2)$ and $k_f/k_1=5$, we find $\ell_f^2/H_\rho^2\approx1.6$, while Fig. 13 suggests that $|q_g|$ is much smaller.

Next, we discuss the results for q_s. In BKR there was some evidence that q_s can become negative in a narrow range of field strengths, but the error bars were rather large. The present results are now much clearer and suggest that $(1-q_s)\overline{B}^2/B_{eq}^2$ is indeed always positive. This is also in agreement with recent convection simulations (Käpylä et al. 2011).

In summary, the present simulations provide no evidence that the coefficients q_s and q_g could contribute to the large-scale instability that causes the magnetic flux concentrations. This is not borne out by the analytic results given in Appendix A. The results from recent convection simulations fall in between the analytic and numerical results mentioned above, because in those q_g was found to be positive, while q_s was still found to be negative (Käpylä et al. 2011).

3.5. *Local field concentrations?*

One of the features we might eventually expect to see is the formation of local magnetic field concentrations in DNS. This may require larger values of the magnetic Reynolds number than what has been possible so far. The current simulations (Fig. 7) do already show some type of magnetic field concentration near the top, but the effect is not yet as pronounced as one would eventually expect it to be. To find out whether magnetic flux concentrations should have been expected, we need to determine the underlying mean-field transport coefficients and compare with a corresponding mean-field model. This will be done in the next section.

4. COMPARISON WITH MEAN-FIELD MODELS

4.1. *Basic equations*

We follow here the same procedure as BKR and consider the equations for the mean velocity $\overline{\boldsymbol{U}}$, the mean density $\overline{\rho}$, and the mean vector potential $\overline{\boldsymbol{A}}$ in the form

$$\frac{\partial\overline{\boldsymbol{U}}}{\partial t}=-\overline{\boldsymbol{U}}\cdot\boldsymbol{\nabla}\overline{\boldsymbol{U}}-c_s^2\boldsymbol{\nabla}\ln\overline{\rho}+\boldsymbol{g}+\overline{\boldsymbol{\mathcal{F}}}^{\rm M}+\overline{\boldsymbol{\mathcal{F}}}_{\rm K,tot}, \quad (18)$$

$$\frac{\partial\overline{\boldsymbol{A}}}{\partial t}=\overline{\boldsymbol{U}}\times\overline{\boldsymbol{B}}+\overline{\boldsymbol{\mathcal{E}}}-\eta\overline{\boldsymbol{J}}-\boldsymbol{\nabla}\overline{\Phi}, \quad (19)$$

$$\frac{\partial\overline{\rho}}{\partial t}=-\boldsymbol{\nabla}\cdot\overline{\rho}\overline{\boldsymbol{U}}, \quad (20)$$

where $\overline{\Phi}$ is the mean electrostatic potential, $\overline{\boldsymbol{B}}=\boldsymbol{B}_0+\boldsymbol{\nabla}\times\overline{\boldsymbol{A}}$ is the mean magnetic field including the imposed field, and

$$\overline{\rho}\overline{\boldsymbol{\mathcal{F}}}^{\rm M}=\overline{\boldsymbol{J}}\times\overline{\boldsymbol{B}}+\tfrac{1}{2}\boldsymbol{\nabla}(q_p\overline{B}^2) \quad (21)$$

is the effective mean Lorentz force, where we use for $q_p(\overline{B})$ the fit formula given by Eq. (15). This fit formula was also used in BKR. However, in view of the results of Sect. 3.4, the q_s and q_g terms will now be omitted, and

$$\overline{\boldsymbol{\mathcal{F}}}_{\rm K,tot}=(\nu_t+\nu)\left(\nabla^2\overline{\boldsymbol{U}}+\boldsymbol{\nabla}\boldsymbol{\nabla}\cdot\overline{\boldsymbol{U}}+2\overline{\boldsymbol{\mathsf{S}}}\boldsymbol{\nabla}\ln\overline{\rho}\right) \quad (22)$$

is the total (turbulent and microscopic) viscous force,

$$\overline{\boldsymbol{\mathcal{E}}}=\boldsymbol{\gamma}\times\overline{\boldsymbol{B}}-\eta_t\overline{\boldsymbol{J}}, \quad (23)$$

is the mean electromotive force, where $\boldsymbol{\gamma}$ is the turbulent pumping velocity and η_t is the turbulent magnetic diffusivity. In our mean-field models we assume $\nu_t/\eta_t=1$ (Yousef et al. 2003). The kinematic theory of Roberts & Soward (1975) and others predicts that $\eta_t(z)=u_{\rm rms}(z)/3k_f$ and $\boldsymbol{\gamma}=-\frac{1}{2}\boldsymbol{\nabla}\eta_t$. It is fairly easy to assess the accuracy of these expressions by computing turbulent transport coefficients from the simulations using the test-field method (Schrinner et al. 2005, 2007). This will be done in Sect. 4.2.

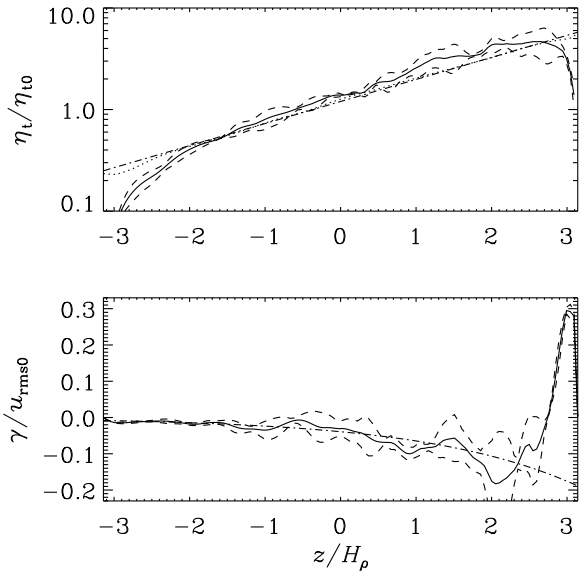

FIG. 14.— Results for η_t and γ with the test-field method (solid lines; error margins are shown as dashed lines). In the upper panel, the dotted line gives $1.2\,u_{\rm rms}/3k_{\rm f}$ and the dash-dotted line represents $1.2\,u_{\rm rms0}\exp(z/H_u)/3k_{\rm f}$. In the lower panel, the dash-dotted lines represents $-1.2\,u_{\rm rms0}\exp(z/H_u)/3k_{\rm f}H_u$.

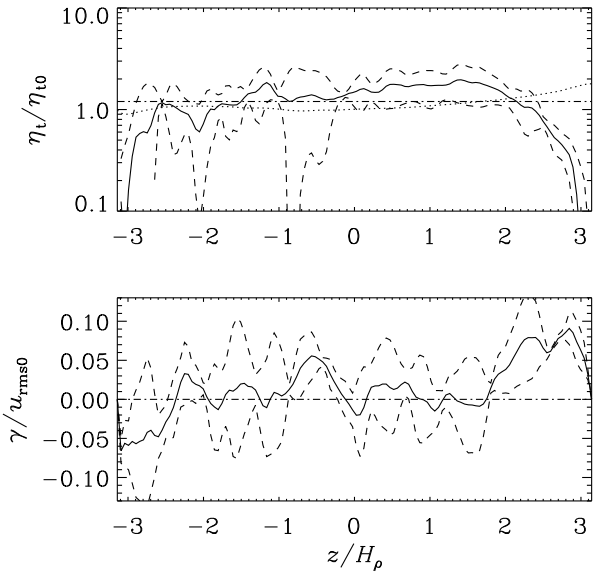

FIG. 15.— Same as Fig. 14, but for the case with $H_u \to \infty$ that corresponds to Model U.

A comment regarding $\overline{\Phi}$ is here in order. It is advantageous to isolate a diffusion operator of the form $\eta_t\nabla^2\overline{\boldsymbol{A}}$ by using the so-called resistive gauge in which $\overline{\Phi} = \eta_t\boldsymbol{\nabla}\cdot\overline{\boldsymbol{A}}$. This means that the diffusion operator now becomes $\eta_t\nabla^2\overline{\boldsymbol{A}}+(\boldsymbol{\nabla}\cdot\overline{\boldsymbol{A}})\boldsymbol{\nabla}\eta_t$ (Dobler et al. 2002). This formulation is important in situation where η_t is non-uniform.

4.2. *Determination of η_t and γ from the simulations*

We use the kinematic test-field method of Schrinner et al. (2005, 2007) in the Cartesian implementation, as described by Brandenburg et al. (2008a), to compute η_t and γ from the simulations. For a response to earlier criticism of this method see Appendix B. We analyze the two setups discussed above and refer to them as Model U (where $u_{\rm rms}$ and hence η_t are nearly constant in height) and Model B (where $B_{\rm eq}$ is nearly constant in height).

The set of test fields includes constant and linearly growing ones. For both models we use $B_0 = 0.01\rho^{1/2}c_{\rm s}$, corresponding to $B_0 \approx 0.1B_{\rm eq0}$ for Model U and $B_0 \approx 0.07B_{\rm eq0}$ for Model B. The results are shown in Figs. 14 and 15. In Table 3 we summarize the relevant parameters inferred for these models. It turns out that the DNS results are well described by $\eta_t = 1.2\,\eta_{t0}$, with $\eta_{t0} = u_{\rm rms}/3k_{\rm f}$ and $u_{\rm rms}(z) = u_{\rm rms0}\exp(z/H_u)$, but $\gamma = -{\rm d}\eta_t/{\rm d}z$, i.e. without the 1/2 factor expected from the kinematic mean-field theory.

We emphasize that $\boldsymbol{\gamma} \approx \boldsymbol{0}$ for Model U, suggesting that additional effects owing to the mean magnetic field such as mean-field magnetic buoyancy (Kitchatinov et al. 1994; Rogachevskii & Kleeorin 2006) are weak (Appendix C)

4.3. *Results from the mean-field models*

Next we consider solutions of Eqs. (18)–(23) for Models U and B using the parameters specified in Table 3. We have either constant η_t (Models U) or constant $B_{\rm eq}$ (Models B). In both cases we use $\eta = 2\nu = 4\times10^{-4}c_{\rm s}/k_1$, $B_0 = 0.01\rho^{1/2}c_{\rm s}$, with $B_p/B_{\rm eq} = 0.12$, which corresponds

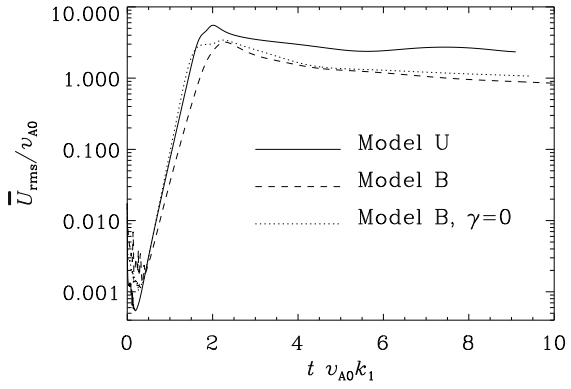

FIG. 16.— Evolution of the mean velocity for Models U and B obtained by solving the mean field equations. Model B' refers to a model where the pumping velocity is ignored.

to the values used in the DNS. As in BKR, these equations exhibit a linear instability with subsequent saturation. However, this result is still remarkable because there are a number of differences compared with the models studied in BKR. Firstly, we consider here an isothermal atmosphere which is stably stratified, unlike the isentropic one used in BKR, which was only marginally stable. This underlines again the robustness of this model and shows that this large-scale instability can be verified over a broad range of conditions. Secondly, this instability also works in situations where η_t and/or $B_{\rm eq}$ are non-uniform and where there is a pumping effect that sometimes might have a tendency to suppress the instability.

TABLE 3
SUMMARY OF PARAMETERS ENTERING MODELS U AND B.

Model	$\eta_{t0}k_1/c_{\rm s}$	$B_{\rm eq}/\rho_0^{1/2}c_{\rm s}$	${\rm Re}_M$	comment
U	0.0088	0.130	66	$B_{\rm eq} = B_{\rm eq0}\,e^{z/2H_\rho}$
B	0.0023	0.035	2.5–60	$\eta_t = \eta_{t0}\,e^{z/2H_\rho}$

In Fig. 16 we compare the evolution of the rms velocity of the mean flow. Note that, in contrast to the corresponding plots in BKR, we have here normalized $\overline{U}_{\rm rms}$ with respect to $v_{\rm A0} \equiv B_0/\sqrt{\overline{\rho}}$ and time is normalized with respect to the Alfvén wave traveling time, $(v_{\rm A0}k_1)^{-1}$. This was done because in these units the curves for Models U and B show similar growth rates. This is especially true when the pumping term is ignored in Model B, i.e. when we set artificially $\gamma = 0$. With pumping included (as was determined from the kinematic test-field method), the growth rate is slightly smaller (compare dashed and dotted lines). The pumping effect does not significantly affect the nonlinear saturation phase, i.e. the late-time saturation behavior for the two versions of Model B is similar. Instead, the saturation phase is different for Model U compared with Model B and the saturation value is larger for Model U.

Visualizations of the mean magnetic field as well as the mean velocity are shown in Fig. 17 for three times near saturation. As in BKR, an eigenfunction develops at the smallest horizontal wavenumber and the field is largest near the top of the domain. As the field reaches saturation, the structures descend, although the ratio $|\overline{B}|/B_{\rm eq}$ is still largest at the top where it reaches values of the order of 0.4.

5. DISCUSSION

To understand the mean-field results obtained above, let us discuss the physics of the large-scale instability in more detail. We consider an isolated flux tube of magnetic field lines. If the flux tube is lighter than the surrounding fluid, it moves upward. The reason for continued upward floating of the magnetic flux tube is as follows. The decrease of the magnetic field inside the ascending tube is due to its expansion, but this is accompanied by an increase of the magnetic pressure inside the tube. The latter is caused by the negative effective mean magnetic pressure, $\frac{1}{2}(1-q_{\rm p})\,\overline{B}^2 < 0$. The decrease of the magnetic field inside the tube results in a decrease of the fluid density and causes buoyancy of the magnetic flux tube. The latter implies the excitation of a large-scale instability. The criterion of this instability reads (Kleeorin et al. 1993, 1996)

$$(1-q_{\rm p})\,(H_\rho - H_B) > 0, \qquad (24)$$

where H_B is the characteristic spatial scale of the mean magnetic field variations. This instability can be excited even in a uniform mean magnetic field ($H_B \to \infty$). The source of free energy of this instability is provided by the small-scale turbulent fluctuations. In contrast, the free energy in the Parker's magnetic buoyancy instability (Parker 1966) or in the interchange instability in plasma (Tserkovnikov 1960) is drawn from the gravitational field. In the absence of turbulence ($q_{\rm p} = 0$), condition (24) coincides with the criterion for the Parker's magnetic buoyancy instability ($H_\rho > H_B$).

Our DNS have shown that for an isothermal atmosphere with strong density stratification the total turbulent pressure is decreased due to the generation of magnetic fluctuations by the tangling an imposed horizontal mean magnetic field by the velocity fluctuations. This phenomenon strongly affects the mean Lorentz force so that the effective mean magnetic pressure becomes negative. For our numerical model with approximately uniform turbulent rms velocity, the ratio of imposed to equipartition field strength changes with height, because the density decreases with height, while the imposed field is constant. This allows us to determine the full functional form of the effective mean magnetic pressure as a function of normalized field strength for a single run.

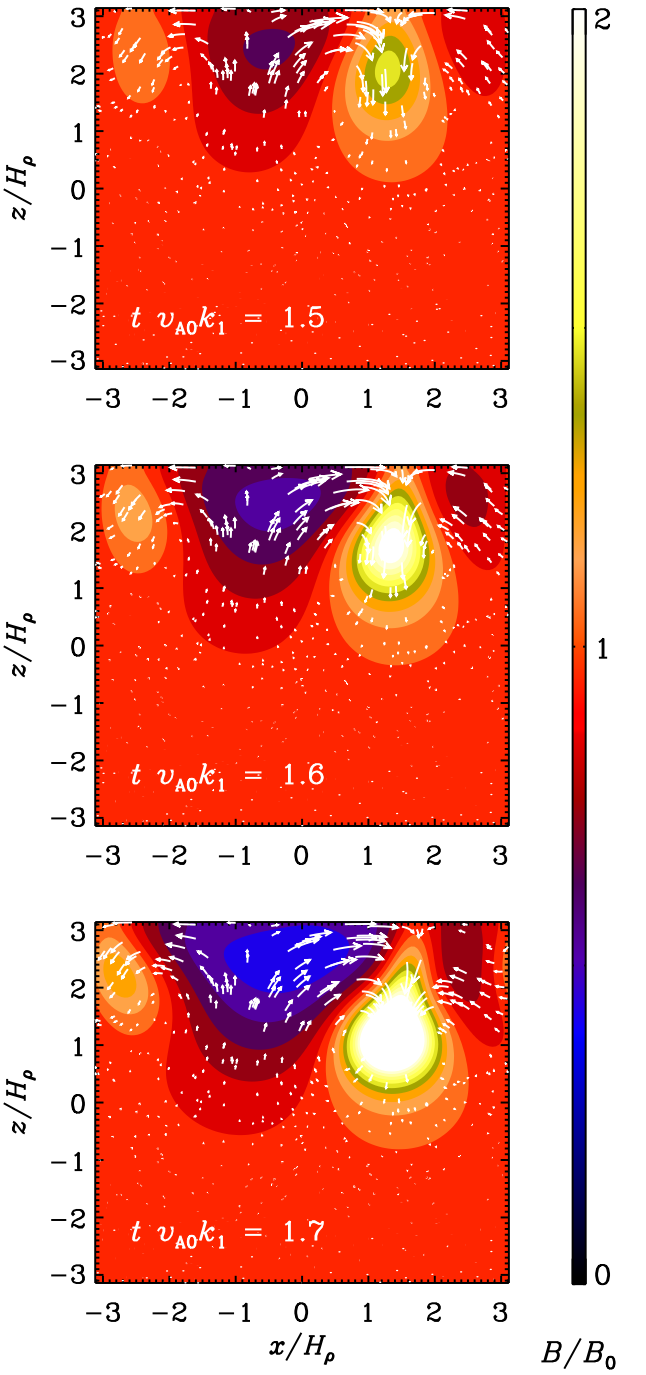

FIG. 17.— Mean magnetic field in the y direction (color coded) together with velocity vectors in the xz plane for Model U. Note the spontaneous production of flux structures.

In all the runs where a negative effective mean magnetic pressure is found, the magnetic fluctuations are noticeably reduced in those parts of the domain where the imposed field exceeds about 10–30% of the equipartition value. This dependence is found to be similar to that obtained earlier using both analytic theory (RK07) and direct numerical simulations (BKR), and the results are robust when changing the strength of the imposed field.

In simulations where the turbulent velocity is nearly inde-

pendent of height, the reduction of magnetic fluctuations occurs in the upper layers where the equipartition field strength decreases with height (Model U). In Model B, where the equipartition field strength is nearly constant in height, the magnetic fluctuations are found to be slightly stronger in the upper parts.

However, none of our direct numerical simulations of forced hydromagnetic turbulence show any obvious signs of a linear large-scale instability that might result in magnetic flux concentrations, as was expected from corresponding mean-field calculations. At this point we can only speculate about possible causes of this discrepancy. Obvious candidates include too small values of the magnetic Reynolds number or too large values of the magnetic Prandtl number. On the other hand, our direct simulations suggest that even for the rather moderate values studied in this paper, a suppression of the total turbulent pressure exists such that the net effective mean magnetic pressure shows a clear negative minimum at about 10–20% of the equipartition value. Another perhaps more likely possibility is that our ansatz for $\overline{\boldsymbol{\mathcal{F}}}_{\rm M}$ is too simplistic. Obvious extensions include higher order terms involving derivatives of the mean magnetic field. Although the effects of such terms should decrease with increasing scale separation, i.e., for larger values of $k_{\rm f}/k_1$, it is not clear that our value of $k_{\rm f}/k_1=5$ is sufficient. Given that the most unstable mode is expected to have an even smaller length scale in the direction of the mean field, it becomes indeed quite likely that $k_{\rm f}/k_1=5$ is not sufficient in that direction. It might therefore be worthwhile to perform DNS with larger scale separation. At the same time, it should be possible to determine the effective mean magnetic pressure using mean magnetic fields that are not uniform but vary on the scale of the domain. Furthermore, it is worthwhile to perform direct numerical simulations of the type presented here, but over a broader range of values of the magnetic Reynolds and Prandtl numbers. In this way it should be possible to optimize our choice of parameters in order to see where the results of mean-field and direct numerical simulations can be brought closer together.

We reiterate that, while our DNS in stratified fluids reproduce the theoretically expected form of $q_{\rm p}(\overline{B}/B_{\rm eq})$, they do not currently demonstrate the excitation of a large-scale instability. This situation is reminiscent of the history of DNS findings of the α effect and large-scale dynamo action. In the early papers of Meneguzzi et al. (1981) and Kida et al. (1991) the absence of a large-scale dynamo instability in helically forced DNS was noted. This, however, was no evidence for the absence of the α effect, but just an artifact of insufficient scale separation, as was noted only much later; see Fig. 23 of Haugen et al. (2004).

We acknowledge the allocation of computing resources provided by the Swedish National Allocations Committee at the Center for Parallel Computers at the Royal Institute of Technology in Stockholm and the National Supercomputer Centers in Linköping as well as the Norwegian National Allocations Committee at the Bergen Center for Computational Science. This work was supported in part by the European Research Council under the AstroDyn Research Project No. 227952 and the Swedish Research Council Grant No. 621-2007-4064. NK and IR thank NORDITA for hospitality and support during their visits.

APPENDIX

A. THE $\overline{B}$ DEPENDENCE OF $q_{\rm p}$, $q_{\rm s}$, AND $q_{\rm g}$

In the following we summarize theoretical results for the $\overline{B}$ dependence of the coefficients $q_{\rm p}$, $q_{\rm s}$, and $q_{\rm g}$ that enter in Eq. (12). We focus here on the case of anisotropic density-stratified background turbulence. Expressions for the isotropic case were given by RK07 and are summarized in BKR. Following BKR, we define $\beta\equiv\overline{B}/B_{\rm eq}$. We define the scale of the energy-carrying eddies as $\ell_{\rm f}=2\pi/k_{\rm f}$. Due to density stratification, new terms emerge that are proportional to $\ell_{\rm f}^2/H_\rho^2$. These terms were absent in BKR, but otherwise the following formulae are identical.

For very weak mean magnetic fields, $4\beta\ll{\rm Rm}^{-1/4}$, $q_{\rm p}$, $q_{\rm s}$ and $q_{\rm g}$ are approximately constant and given by

$$q_{\rm p}(\beta)=\frac{4}{45}\left(1+9\ln{\rm Rm}\right)(1-\epsilon)+\frac{16\,\ell_{\rm f}^2}{9\,H_\rho^2},\quad q_{\rm s}(\beta)=\frac{1}{15}\left(1+8\ln{\rm Rm}\right)(1-\epsilon),\quad q_{\rm g}(\beta)=-\frac{8\,\ell_{\rm f}^2}{3\,H_\rho^2};\tag{A1}$$

for ${\rm Rm}^{-1/4}\ll4\beta\ll1$ we have

$$q_{\rm p}(\beta)=\frac{16}{25}\left[1+5|\ln(4\beta)|+32\,\beta^2\right](1-\epsilon)+\frac{16\,\ell_{\rm f}^2}{9\,H_\rho^2}\Big[1-\frac{16\beta^2}{5}\Big],\tag{A2}$$

$$q_{\rm s}(\beta)=\frac{32}{15}\left[|\ln(4\beta)|+\frac{1}{30}+12\beta^2\right](1-\epsilon),\quad q_{\rm g}(\beta)=-\frac{8\,\ell_{\rm f}^2}{3\,H_\rho^2}\left[1-\frac{16\,\beta^2}{5}\right];\tag{A3}$$

and for strong fields, $4\beta\gg1$, we have

$$q_{\rm p}(\beta)=\frac{1}{6\beta^2}\Big(1-\epsilon+\frac{3\,\ell_{\rm f}^2}{H_\rho^2}\Big),\quad q_{\rm s}(\beta)=\frac{\pi}{48\beta^3}\,(1-\epsilon),\quad q_{\rm g}(\beta)=-\frac{3\,\ell_{\rm f}^2}{4\,H_\rho^2\,\beta^2},\tag{A4}$$

where the parameter $\epsilon=\langle\boldsymbol{b}_0^2\rangle/\langle\boldsymbol{u}_0^2\rangle$ takes into account the contributions caused by the small-scale dynamo (see RK07, where it was assumed for simplicity that the range of scales of magnetic fluctuations generated by the small-scale dynamo coincides with that of the velocity fluctuations). Here we have taken into account that the anisotropic contributions to the nonlinear functions $q_{\rm p}(\beta)$ and $q_{\rm g}(\beta)$ for density-stratified background turbulence are given by

$$q_{\rm g}(\beta)=-\frac{3}{2}\,q_{\rm p}(\beta)=-\frac{8\,\ell_{\rm f}^2}{3\,H_\rho^2}\left[64\beta^4-4\beta^2+\frac{1}{3}+\frac{1}{4\beta^2}-2^9\,\ln\Big(1+\frac{1}{8\beta^2}\Big)-\frac{\arctan(\sqrt{8}\beta)}{8\sqrt{2}\,\beta^3}\right].\tag{A5}$$

For the derivation of Eq. (A5) we used Eqs. (A10)–(A11) given by RK07 with the following model of the density-stratified background turbulence written in the Fourier space:

$$\langle u_i(\boldsymbol{k})\, u_j(-\boldsymbol{k})\rangle = \frac{\langle \boldsymbol{u}_0^2\rangle\, E(k)}{8\pi\, k^2\, (k^2+\lambda^2)}\Big[\delta_{ij}\,(k^2+\lambda^2) - k_i\, k_j - \lambda_i\, \lambda_j + \mathrm{i}\,\big(\lambda_i\, k_j - \lambda_j\, k_i\big)\Big], \tag{A6}$$

where the velocity field satisfies the continuity equation in the anelastic approximation $\mathrm{div}\,\boldsymbol{u} = u_i\,\lambda_i,\ \lambda_i = -\nabla_i\overline{\rho}/\overline{\rho},\ \delta_{ij}$ is the Kronecker tensor, the energy spectrum function is $E(k) = (2/3)\, k_{\rm f}^{-1}\,(k/k_f)^{-5/3}$ for $k_{\rm f} < k < k_{\rm f}\,{\rm Re}^{3/4}$.

B. CRITICISMS OF THE TEST-FIELD METHOD

The kinematic test-field method has previously been criticized on the grounds that it invokes a predetermined arbitrary mean field. It has been argued (Cattaneo & Hughes 2008) that this technique will therefore yield only approximations to the true mean-field coefficients, and that their quality will depend on how well the true mean field is approximated by the choice of test field. This is not true, and the original criticism was in fact absent in the published version (Cattaneo & Hughes 2009). However, we emphasize that one needs not only one, but a set of different test fields to determine all relevant components of the α and turbulent diffusivity tensors. Furthermore, for finite scale separation ratios in space and time one also needs to represent all frequencies in space and time. The knowledge of all higher frequencies allows one to compute the integral kernels that describe the nonlocality of turbulent transport; see Brandenburg et al. (2008c) for nonlocality in space and Hubbard & Brandenburg (2009) for nonlocality in time. The multitude of test fields does allow one to compute also those parts of the α and turbulent diffusivity tensors that do not enter in the particular problem at hand, but also those parts that enter under any other circumstances. An example is the evolution of a passive vector field where the same mean-field theory applies (Tilgner & Brandenburg 2008).

Furthermore, had we used the quasi-kinematic test-field method, we would need to respond to the criticism of Courvoisier et al. (2010), who point out that this method fails if there is hydromagnetic background turbulence originating, for example, from small-scale dynamo action. In such a case a fully nonlinear test-field method must be employed (Rheinhardt & Brandenburg 2010). Furthermore, it is worth noting that even in cases where small-scale dynamo action was expected, such as those of Brandenburg et al. (2008b) where values of ${\rm Re}_M$ up to 600 were considered, the quasi-kinematic test-field method was still found to yield valid and self-consistent results, as was demonstrated by comparing the growth rate expected from the obtained coefficients of α_{ij} and η_{ij}. This growth rate was confirmed to be compatible with zero in the steady state; see also Ponty & Plunian (2011). Finally, as shown in Rheinhardt & Brandenburg (2010), the quasi-kinematic method is valid if magnetic fluctuations result solely from an imposed field.

C. COMMENTS ON MEAN-FIELD BUOYANCY

The work of Kitchatinov & Pipin (1993) is of interest in the present context, because it predicts the upward pumping of mean magnetic field. Here we discuss various short-comings of this work. (i) The gradient of the mean density is zero, (ii) the background turbulence is homogeneous, (iii) fluctuations of pressure, density and temperature are adiabatic, (iv) low Mach number flows are considered. Since the gradient of the mean density is zero, the hydrostatic equilibrium, $\boldsymbol{\nabla} p = \rho \boldsymbol{g}$, exists only if the gradient of the mean temperature is not zero. This implies that the turbulent heat flux is not zero and temperature fluctuations are generated by the tangling of this mean temperature gradient by the velocity fluctuations. Therefore, the key assumption made in Kitchatinov & Pipin (1993) that fluctuations of pressure, density and temperature are adiabatic, is not valid and the equation for the evolution of entropy fluctuations should be taken into account. This implies furthermore that the temperature fluctuations in Eq. (2.5) of their paper cannot be neglected. By contrast, we consider here flows with a non-zero mean density gradient and turbulence simulations that have strong density stratification.

REFERENCES

Brandenburg, A., & Dobler, W. 2002, Comp. Phys. Comm., 147, 471
Brandenburg, A., & Subramanian, K. 2005a, Phys. Rep., 417, 1
Brandenburg, A., & Subramanian, K. 2005, A&A, 439, 835
Brandenburg, A., & Subramanian, K. 2007, Astron. Nachr., 328, 507
Brandenburg, A., Käpylä, P., & Mohammed, A. 2004, Phys. Fluids, 16, 1020
Brandenburg, A., Kleeorin, N., & Rogachevskii, I. 2010, Astron. Nachr., 331, 5 (BKR)
Brandenburg, A., Rädler, K.-H., Rheinhardt, M., & Käpylä, P. J. 2008, ApJ, 676, 740
Brandenburg, A., Rädler, K.-H., Rheinhardt, M., & Subramanian, K. 2008b, ApJ, 687, L49
Brandenburg, A., Rädler, K.-H., & Schrinner, M. 2008c, A&A, 482, 739
Cattaneo, F., & Hughes, D. W. 1988, J. Fluid Mech., 196, 323
Cattaneo, F., Brummell, N. H., Toomre, J., Malagoli, A., and Hurlburt, N. E. 1991, ApJ, 370, 282
Cattaneo, F., & Hughes, D. W. 2008, arXiv:0805.2138v1
Cattaneo, F., & Hughes, D. W. 2009, MNRAS, 395, L48
Courvoisier A., Hughes D. W., & Proctor M. R. E. 2010, Proc. Roy. Soc. Lond., 466, 583
Dobler, W., Shukurov, A., & Brandenburg, A. 2002, Phys. Rev. E, 65, 036311
Gilman P.A. 1970a, ApJ, 162, 1019
Gilman P.A. 1970b, A&A, 286, 305
Haugen, N. E. L., Brandenburg, A., & Dobler, W. 2004, Phys. Rev. E, 70, 016308
Hood, A. W., Archontis, V., Galsgaard, K., & Moreno-Insertis, F. 2009, A&A, 503, 999
Hubbard, A., & Brandenburg, A. 2009, ApJ, 706, 712
Hughes, D. W. 2007, in The Solar Tachocline, ed. D. W. Hughes, R. Rosner, & N. O. Weiss (Cambridge: Cambridge Univ. Press), 275
Hughes, D. W., & Proctor, M. R. E. 1988, Ann. Rev. Fluid Mech., 20, 187
Isobe, H., Miyagoshi, T., Shibata, K., & Yokoyama, T. 2005, Nature, 434, 478
Käpylä, P. J., Brandenburg, A., Kleeorin, N., Mantere, M. J., & Rogachevskii, I. 2011, arXiv:1104.4541
Kersalé, E., Hughes, D. W., & Tobias, S. M. 2007, ApJ, 663, L113
Kida, S., Yanase, S., & Mizushima, J. 1991, Phys. Fluids, A 3, 457
Kitchatinov, L.L., & Mazur, M.V. 2000, Solar Phys., 191, 325
Kitchatinov, L. L., & Pipin, V. V. 1993, A&A, 274, 647
Kichatinov, L. L., Rüdiger, G., & Pipin V. V. 1994, Astron. Nachr., 315, 157
Kitiashvili, I. N., Kosovichev, A. G., Wray, A. A., & Mansour, N. N. 2010, ApJ, 719, 307
Kleeorin, N., Mond, M., & Rogachevskii, I. 1993, Phys. Fluids B, 5, 4128
Kleeorin, N., Mond, M., & Rogachevskii, I. 1996, A&A, 307, 293

Kleeorin, N., & Rogachevskii, I. 1994, Phys. Rev. E, 50, 2716
Kleeorin, N.I., Rogachevskii, I.V., & Ruzmaikin, A.A. 1990, Sov. Phys. JETP, 70, 878
Krause, F., & Rädler, K.-H. 1980, Mean-field magnetohydrodynamics and dynamo theory (Pergamon Press, Oxford)
Martínez, J., Hansteen, V. & Carlson, M. 2008, ApJ, 679, 871
Meneguzzi, M., Frisch, U., & Pouquet, A. 1981, Phys. Rev. Lett., 47, 1060
Moffatt, H.K. 1978, Magnetic field generation in electrically conducting fluids (Cambridge University Press, Cambridge)
Newcomb, W. A. 1961, Phys. Fluids, 4, 391
Parker, E.N. 1966, ApJ, 145, 811
Parker, E.N. 1979a, ApJ, 230, 905
Parker, E.N. 1979b, Cosmical magnetic fields (Oxford University Press, New York)
Ponty, Y., & Plunian, F. 2011, Phys. Rev. Lett., 106, 154502
Prandtl, L. 1925, Zeitschr. Angewandt. Math. Mech., 5, 136
Rädler, K.-H. 1969, Monats. Dt. Akad. Wiss., 11, 194
Rempel, M., Schüssler, M., & Knölker, M. 2009, ApJ, 691, 640
Rheinhardt, M., & Brandenburg, A. 2010, A&A, 520, A28
Roberts, P. H., & Soward, A. M. 1975, Astron. Nachr., 296, 49
Rogachevskii, I., & Kleeorin, N. 2006, Geophys. Astrophys. Fluid Dyn., 100, 243
Rogachevskii, I., & Kleeorin, N. 2007, Phys. Rev. E, 76, 056307 (RK07)
Rüdiger, G. 1980, Geophys. Astrophys. Fluid Dyn., 16, 239
Rüdiger, G. 1989, Differential rotation and stellar convection: Sun and solar-type stars (Gordon & Breach, New York)
Rüdiger, G., & Hollerbach, R. 2004, The magnetic universe (Wiley-VCH, Weinheim)
Schrinner, M., Rädler, K.-H., Schmitt, D., Rheinhardt, M., Christensen, U. 2005, Astron. Nachr., 326, 245
Schrinner, M., Rädler, K.-H., Schmitt, D., Rheinhardt, M., Christensen, U. R. 2007, Geophys. Astrophys. Fluid Dyn., 101, 81
Schüssler, M., & Vögler, A. 2006, ApJ, 641, L73
Solanki, S. K., Inhester, B., & Schüssler, M. 2006, Rep. Progr. Phys., 69, 563
Spruit, H. C. 2011, in The Sun, the Solar Wind, and the Heliosphere, ed. M. P. Miralles & J. Sánchez Almeida (IAGA Special Sopron Book Series, Vol. 4. Berlin: Springer), 39
Stein, R. F. & Nordlund, Å. 2001, ApJ, 546, 585
Tao, L., Weiss, N. O., Brownjohn, D. P., & Proctor, M. R. E. 1998, ApJ, 496, L39
Taylor, G. I. 1921, Proc. Lond. Math. Soc., 20, 196
Tilgner, A., & Brandenburg, A. 2008, MNRAS, 391, 1477
Tobias, S. M., & Weiss, N. O. 2007, in The Solar Tachocline, ed. D.W. Hughes, R. Rosner, & N. O. Weiss (Cambridge: Cambridge Univ. Press), 319
Tserkovnikov, Y. A. 1960, Sov. Phys. Dokl., 5, 87
Wissink, J. G., Hughes, D. W., Matthews, P. C., & Proctor, M. R. E. 2000, MNRAS, 318, 501
Yousef, T. A., Brandenburg, A., & Rüdiger, G. 2003, A&A, 411, 321

II

Properties of the negative effective magnetic pressure instability

K. Kemel[1,2], **A. Brandenburg**[1,2], **N. Kleeorin**[3], **I. Rogachevskii**[3]

[1] NORDITA, AlbaNova University Center, Roslagstullsbacken 23, SE 10691 Stockholm, Sweden
[2] Department of Astronomy, AlbaNova University Center, Stockholm University, SE 10691 Stockholm, Sweden
[3] Department of Mechanical Engineering, The Ben-Gurion University of the Negev, POB 653, Beer-Sheva 84105, Israel

July 15, 2011, Revision: 1.42

Key words magnetohydrodynamics (MHD) – instabilities – turbulence

As was demonstrated in earlier studies, turbulence can result in a negative contribution to the effective mean magnetic pressure, which, in turn, can cause a large-scale instability. In this study, hydromagnetic mean-field modelling is performed for an isothermally stratified layer in the presence of a horizontal magnetic field, and the negative effective magnetic pressure instability (NEMPI) is comprehensively investigated. It is shown that, if the effect of turbulence on the mean magnetic tension force vanishes, which is consistent with results from direct numerical simulations of forced turbulence, the fastest growing eigenmodes of NEMPI are two-dimensional. The growth rate is found to be sensitive to details of the dependence of the effective mean magnetic pressure on the mean magnetic field. A fit formula is proposed that gives the growth rate as a function of turbulent kinematic viscosity, turbulent magnetic diffusivity, mean magnetic field strength, and the degree of stratification. The formation of sunspots and solar active regions is discussed as a possible application of NEMPI.

1 Introduction

The concept of turbulent viscosity is often used in astrophysical and other applications in recognition of the fact that the microscopic viscosity is far too small to be relevant on the length scales under consideration. Turbulent viscosity is the simplest parameterization of the Reynolds stress tensor, $\overline{u_i u_j}$, where $\boldsymbol{u} = \boldsymbol{U} - \overline{\boldsymbol{U}}$ is the velocity fluctuation about a suitably defined average, denoted here by an overbar. Turbulent viscosity is by far not the only contribution to the Reynolds stress tensor.

In addition to hydrodynamic contributions such as the Λ effect (Rüdiger 1980, 1989), which is relevant to explaining stellar differential rotation (Rüdiger & Hollerbach 2004), and the anisotropic kinetic alpha effect (Frisch et al. 1987), which provides an important test case in mean-field hydrodynamics (Brandenburg & von Rekowski 2001; Courvoisier et al. 2010), there are magnetic contributions as well. One can think of them as a magnetic feedback on the hydrodynamic stress tensor (Rädler 1974; Rüdiger 1974) or, especially when magnetic fluctuations are also considered, as a mean-field contribution to the turbulent Lorentz force.

Work by Rüdiger et al. (1986) suggested that the total magnetic tension force that includes the effects of fluctuations should be reduced and might even change sign. A similar result was obtained by Kleeorin et al. (1989, 1990) using spectral τ approach who also found another effect of a reversal of the effective magnetic pressure term; see also Kleeorin & Rogachevskii (1994) and Kleeorin et al. (1993, 1996). Rogachevskii & Kleeorin (2007) argued that in turbulent convection this can lead to the formation of large-scale magnetic flux structures and perhaps even sunspots and active regions.

Recently, direct numerical simulations (DNS) of both unstratified and stratified forced turbulence (Brandenburg et al. 2010, 2011; hereafter referred to as BKR and BKKR, respectively) have substantiated this idea and have demonstrated that the effective magnetic pressure can indeed change sign. Similar results have now also been obtained for turbulent convection (Käpylä et al. 2011a). These papers have provided mean-field calculations illustrating that there is a negative effective magnetic pressure instability (hereafter referred to as NEMPI) when there is sufficient density stratification.

This instability is the convective type instability as well as interchange instability in plasma (Tserkovnikov 1960; Priest 1982) or magnetic buoyancy instability (Parker 1966). On the other hand, the source of free energy of NEMPI is provided by the small-scale turbulence, while the free energy in interchange or magnetic buoyancy instability is drawn from the gravitational field. The mechanism of NEMPI works even under isothermal conditions when entropy evolution is ignored and an isothermal equation of state is used. Three-dimensional calculations have shown that the mean magnetic field develops structure along the direction of the field (BKR). However, while the mean-field calculations have illustrated the nature of the instability, no systematic survey of solutions has yet been attempted.

The purpose of this paper is to clarify some still puzzling aspects concerning NEMPI. This is particularly important in view of the fact that no clear evidence of NEMPI has yet been seen in DNS (BKKR). In other words, although DNS

have shown that the effective mean magnetic pressure can change sign, and although we know from mean-field models that this should lead to the formation of structures near the surface, this type of structure formation has not been seen in DNS.

On the other hand, some type of structure formation has recently been reported in Large-Eddy Simulations (LES), so one wonders whether this might be an indication of NEMPI. We have here in mind the radiation magneto-convection simulations of Kitiashvili et al. (2010), in which one sees the formation of whirlpool-like magnetic structures. However, even in the absence of magnetic fields, one finds the formation of whirlpools, although this requires rapid rotation (Käpylä et al. 2011b).

Most relevant to NEMPI is perhaps the work of Tao et al. (1998), who also considered magneto-convection and find a horizontal segregation into magnetized and non-magnetized regions. The size of the individual regions is such that they encompass several turbulent eddies. This phenomenon might therefore well be associated with an effect that could also be modelled in terms of mean-field theory. However, before we can make such an association, we need to find out more about the properties of NEMPI. In particular, we need to know what is the optimal magnetic field strength, what are the requirements or restrictions in the turbulent velocity, and, finally, how much density stratification is needed to make NEMPI work.

To connect the aforementioned requirements to DNS, we need to have a meaningful parameterization of the turbulence effects. The work done so far has been focussing on measuring a reduction of the turbulent pressure and effective mean magnetic pressure as a function of the local mean magnetic field strength. The shape of the resulting dependence of the effective mean magnetic pressure on the mean magnetic field has been matched to a specific fit formula that can be characterized by two fit parameters that, in turn, can be linked to the minimum effective mean magnetic pressure and the critical field strength above which the effect is suppressed. However, there have been indications that this parameterization is not unique and that different combinations of the two fit parameters can result in similar values of minimum effective pressure and the critical field strength. The question therefore arises whether this degeneracy is important for the properties of NEMPI.

Finally, we mentioned already the fact that NEMPI is capable of exciting three-dimensional structures that show variation along the direction of the mean magnetic field. This would raise the worry that the two-dimensional results presented so far may not reflect the properties of the fastest growing mode and may therefore not be relevant to describing NEMPI. However, it turns out that this is not the case, because the degree to which three-dimensional modes are excited depends on the sign of one of the turbulence parameters, namely the term characterizing turbulence effects on the magnetic tension force, and that simulations indicate that this sign is not favorable for exciting three-dimensional modes (BKR). Before we begin addressing the various points, we discuss first the mean-field model and turn then to the points raised above.

2 Mean-field model

In view of future verifications of NEMPI with DNS, it is essential to be able to reduce the essential physics to a minimum. We will therefore not make any attempt to consider other aspects that would make the model more realistic with respect to the Sun. Given that NEMPI works even under isothermal conditions (BKKR), we adopt an isothermal equation of state where the mean pressure $\overline{p}$ is linear in the mean density $\overline{\rho}$, with $\overline{p}=\overline{\rho}c_{\rm s}^2$, and $c_{\rm s}=\,$const being the isothermal sound speed. We solve the evolution equations for mean velocity $\overline{\boldsymbol{U}}$, mean density $\overline{\rho}$, and mean vector potential $\overline{\boldsymbol{A}}$, in the form

$$\frac{\partial\overline{\boldsymbol{U}}}{\partial t}=-\overline{\boldsymbol{U}}\cdot\boldsymbol{\nabla}\overline{\boldsymbol{U}}-c_{\rm s}^2\boldsymbol{\nabla}\ln\overline{\rho}+\boldsymbol{g}+\overline{\boldsymbol{\mathcal{F}}}_{\rm M}+\overline{\boldsymbol{\mathcal{F}}}_{\rm K}, \quad (1)$$

$$\frac{\partial\overline{\rho}}{\partial t}=-\overline{\boldsymbol{U}}\cdot\boldsymbol{\nabla}\overline{\rho}-\overline{\rho}\boldsymbol{\nabla}\cdot\overline{\boldsymbol{U}}, \quad (2)$$

$$\frac{\partial\overline{\boldsymbol{A}}}{\partial t}=\overline{\boldsymbol{U}}\times\overline{\boldsymbol{B}}-(\eta_{\rm t}+\eta)\overline{\boldsymbol{J}}, \quad (3)$$

where $\overline{\boldsymbol{\mathcal{F}}}_{\rm M}$ is given by

$$\overline{\rho}\,\overline{\boldsymbol{\mathcal{F}}}_{\rm M}=-\tfrac{1}{2}\boldsymbol{\nabla}[(1-q_{\rm p})\overline{\boldsymbol{B}}^2]+\overline{\boldsymbol{B}}\cdot\boldsymbol{\nabla}\left[(1-q_{\rm s})\overline{\boldsymbol{B}}\right], \quad (4)$$

and

$$\overline{\boldsymbol{\mathcal{F}}}_{\rm K}=(\nu_{\rm t}+\nu)\left(\nabla^2\overline{\boldsymbol{U}}+\boldsymbol{\nabla}\boldsymbol{\nabla}\cdot\overline{\boldsymbol{U}}+2\overline{\mathsf{S}}\boldsymbol{\nabla}\ln\overline{\rho}\right) \quad (5)$$

is the total (turbulent plus microscopic) viscous force. Here, $\mathsf{S}_{ij}=\frac{1}{2}(\overline{U}_{i,j}+\overline{U}_{j,i})-\frac{1}{3}\delta_{ij}\boldsymbol{\nabla}\cdot\overline{\boldsymbol{U}}$ is the traceless rate of strain tensor of the mean flow. As in earlier work (BKR, BKKR), we approximate $q_{\rm p}$ and $q_{\rm s}$ by simple profiles that are only functions of the ratio $\beta\equiv|\overline{\boldsymbol{B}}|/B_{\rm eq}$, i.e.,

$$q_\sigma(\beta)=q_{\rm i0}[1-(2/\pi)\arctan(\beta^2/\beta_\sigma^2)], \quad (6)$$

where σ stands for subscripts p and s, respectively. The functions $q_{\rm p}$ and $q_{\rm s}$ quantify the impact of the mean magnetic field on the effective pressure and tension forces, respectively.

As initial condition, we assume a hydrostatic stratification with $\overline{\rho}(z)=\rho_0\exp(-z/H_\rho)$, where $H_\rho=c_{\rm s}^2/g$ is the scale height in a domain of size $L_x\times L_y\times L_z$, where $-L_z/2\leq z\leq L_z/2$. We normally use $L_x=L_y\equiv L$ and, unless noted otherwise, also $L_z=L$. In most of the cases we use $L_x=L_y=L_z\equiv L$. We add a small perturbation to the velocity field. We allow for the presence of an imposed field in the y direction, $\boldsymbol{B}_0=(0,B_0,0)$. The total field is then written as

$$\overline{\boldsymbol{B}}=\boldsymbol{B}_0+\boldsymbol{\nabla}\times\overline{\boldsymbol{A}}, \quad (7)$$

so the departure from the imposed field is expressed in terms of the mean magnetic vector potential $\overline{\boldsymbol{A}}$.

On the upper and lower boundaries we adopt stress-free boundary conditions for velocity, i.e. $\overline{U}_{x,z}=\overline{U}_{y,z}=\overline{U}_z=$

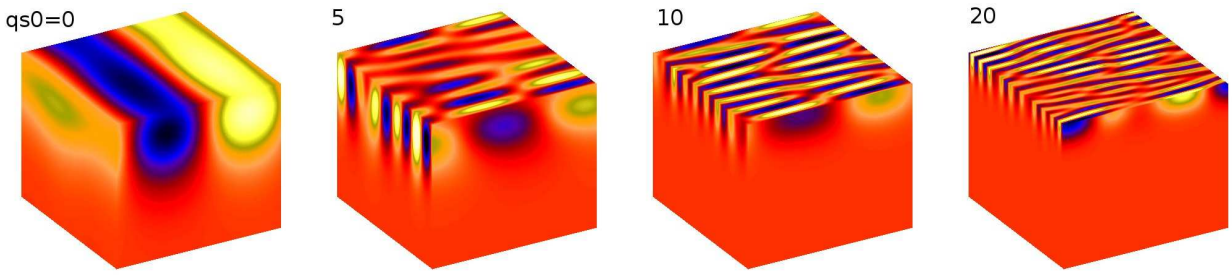

Fig. 1 Visualization of $\overline{B}_y$ at the periphery of the computational domain near the end of the kinematic growth phase. Note the change of the field pattern with increasing values of $q_{\rm s0}$ (=0, 5, 10, and 20 from left to right).

0, and a perfect conductor boundary condition for the magnetic field, i.e. $\overline{A}_x = \overline{A}_y = \overline{A}_{z,z} = 0$. Here, commas denote partial differentiation. No boundary condition for the density is required. All computations have been carried out with the PENCIL CODE[1].

Our model is characterized by the following set of input parameters. There are four parameters characterizing the hydrostatic equilibrium stratification, namely g, $c_{\rm s}^2$, ρ_0, and L_z. The remaining parameters are the Alfvén speed at the surface, $v_{\rm A}^{\rm top} = B_0/\sqrt{\rho_{\rm top}\mu_0}$, turbulent viscosity and magnetic diffusivity, as well as the parameters $q_{\sigma 0}$ and β_σ. Here, $\rho_{\rm top} = \rho_0 \exp(-z_{\rm top}/H_\rho)$ is the density at the surface, which is usually at $z \equiv z_{\rm top} = L_z/2$.

3 Results

3.1 Two- and three-dimensional solutions

Earlier work has suggested that the eigenmodes of NEMPI can be three-dimensional (BKR). This could make two-dimensional calculations questionable if the first excited mode were indeed the fastest growing one. However, it turns out that the wavelength of the eigenmode in the direction of the field increases as $q_{\rm s}$ decreases. In BKR, where three-dimensional (y-dependent) solutions to NEMPI were first reported, $q_{\rm s}$ was chosen to be around 10, and the fastest growing mode was indeed three-dimensional. In Fig. 1 we show that the effective wavenumber of the variation of the field in the y direction decreases with decreasing values of $q_{\rm s}$. This is shown quantitatively in Fig. 2, where we plot the dependence of the typical value of the field-aligned wavenumber, k_y, on the value of $q_{\rm s0}$. Here, k_y is evaluated in a layer near the surface. For normalization purposes, we define the lowest wavenumber in the computational domain as $k_1 = 2\pi/L$.

We find that the typical value of k_y grows approximately linearly with increasing values of $q_{\rm s0}$. As an approximate fit formula we can use $k_y^2/k_1^2 \approx 1.3\,q_{\rm s0}$. In addition, we find that the growth rate of the instability, λ, grows with $q_{\rm s0}$ approximately linearly, once $q_{\rm s0}$ exceeds a value of around 5. The fact that $k_y \to 0$ as $q_{\rm s0} \to 0$ is significant, because BKKR and also Käpylä et al. (2011b) found from simulations that $q_{\rm s0} \approx 0$. In that case, the characteristic length scale along the direction of the field becomes infinite and the calculation essentially two-dimensional. Conversely, when studying NEMPI in two dimensions, changing the value of $q_{\rm s0}$ has no effect on structure formation and the growth rate; see Table 1. However, it is now clear that this is an artifact of restricting the solutions to be two-dimensional.

3.2 Degeneracy in the $q_{\rm p}$ fit formula

We mentioned in the introduction that recent attempts to determine $q_{\rm p0}$ from simulations faced the difficulty that the fit formula possesses a degeneracy in that we can obtain a similarly looking dependence of the effective mean magnetic pressure $\mathcal{P}_{\rm eff}(\beta) = [1 - q_{\rm p}(\beta)]\,\beta^2$ over a wide range of values of $q_{\rm p0}$ by adjusting the value of $\beta_{\rm p}$ correspondingly. The core of the problem becomes clear from Fig. 3, where we plot the function $\mathcal{P}_{\rm eff}(\beta)$ in the lower panel and $\min(\mathcal{P}_{\rm eff})$ versus $\beta_{\rm crit}$ in the upper panel. The parameter $\beta_{\rm crit}$ is defined by the condition $\mathcal{P}_{\rm eff}(\beta_{\rm crit}) = 0$. It is evident that $\min(\mathcal{P}_{\rm eff})$ becomes more negative as $\beta_{\rm crit}$ decreases and $q_{\rm p0}$ increases. However, for a given value of $\beta_{\rm crit}$, the fit formula cannot produce a minimum of $\mathcal{P}_{\rm eff}$ that is below a certain value. This minimum value is attained for $q_{\rm p0} \to \infty$, but even the graphs for $q_{\rm p0} = 50$ or 20 lie quite close together. Conversely, for a given value of $\min(\mathcal{P}_{\rm eff})$, there is a minimum value of $\beta_{\rm crit}$ below which there is no solution. For $\min(\mathcal{P}_{\rm eff}) = -0.1$, for example, there are no values of $q_{\rm p0}$ for $\beta_{\rm crit}$ below about 0.3, while between 0.30 and 0.35 the same value of $\min(\mathcal{P}_{\rm eff})$ can be attained for $q_{\rm p0}$ between 20 and ∞. This is shown more clearly in the second panel of

Table 1 Comparison of growth rates for different values of L_y and $q_{\rm s}$, including a two-dimensional (2D) simulation ($L_y \to \infty$).

	L_y	$q_{\rm s} = 0$	$q_{\rm s} = 30$
3D	L	0.0124	0.2070
3D	$8L$	0.0137	
2D	∞	0.0141	0.0141

[1] http://www.pencil-code.googlecode.com

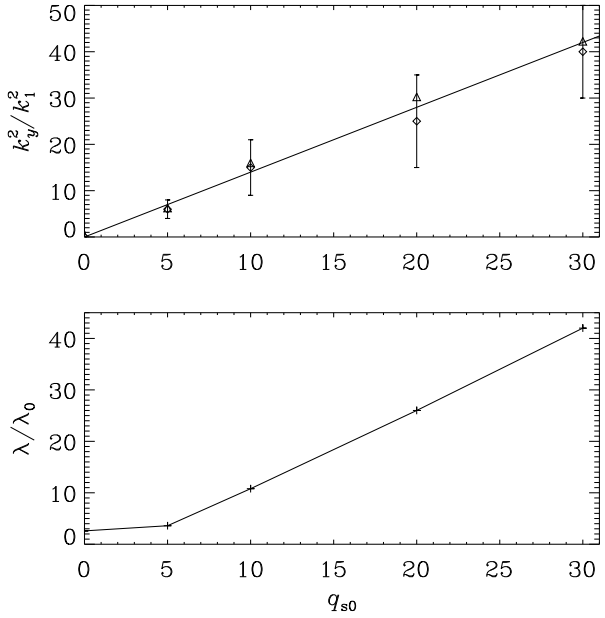

Fig. 2 Dependence of k_y on q_{s0} (upper panel), together with the corresponding growth rate λ (lower panel). Here, λ is normalized by $\lambda_0 \equiv g/c_s$.

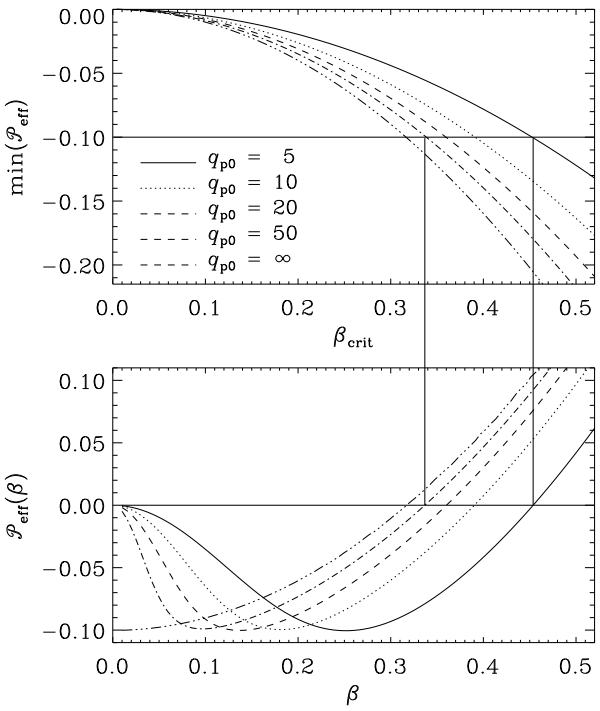

Fig. 3 Minimum effective magnetic pressure versus $\beta_{\rm crit}$ for 5 values of q_{p0} (upper panel), and the corresponding graphs of $\mathcal{P}_{\rm eff}(\beta)$ for which $\mathcal{P}_{\rm eff} = -0.1$. For two values of q_{p0} (5 and 50) the correspondence between $\beta_{\rm crit}$ and the zero point of $\mathcal{P}_{\rm eff}(\beta)$ for curves with $\min(\mathcal{P}_{\rm eff}) = -0.1$ is shown by vertical lines.

Fig. 3, where we plot $\mathcal{P}_{\rm eff}(\beta)$ for different values of q_{p0} and values of $\beta_{\rm crit}$ that all cross the line $\min(\mathcal{P}_{\rm eff}) = -0.1$ in the upper panel of this figure. This shows that, when q_{p0} is 10 or larger, the graph of $\mathcal{P}_{\rm eff}(\beta)$ becomes quite insensitive to the exact value of q_{p0}, and that the same graphs can be obtained for a set of different combinations of q_{p0} and β_p.

In the family of similarly looking solutions, the optimal value of B_p is found to decrease with increasing values of q_{p0}, as is shown in the upper panel of Fig. 4. However, even though the graphs of $q_p(\beta)$ are rather similar, mean-field simulation show that the resulting growth rates are sensitive to the value of q_p in the parameter regime where $\overline{B}/B_{\rm eq}$ is small. An alternative would be to use a third observation to fix the degeneracy of the model. One such parameter could be the position of the minimum of $\mathcal{P}_{\rm eff}$, i.e., the value $\beta_{\rm min}$, for which $\mathcal{P}_{\rm eff}(\beta_{\rm min}) = \min(\mathcal{P}_{\rm eff})$ is obeyed.

3.3 Onset condition of NEMPI

With a given prescription of $q_p(\beta)$, assuming here $q_{s0} = 0$, we can now compute two-dimensional mean-field models. Our goal is to obtain a simple description that can tell us how large the growth rate of the instability is, and what the critical condition for the onset of the instability is. Not much is known about the linear stability properties of NEMPI, so we have to rely on numerical determinations of the growth rates for different wavelengths in the different directions to obtain an approximate representation of the dispersion relation. Earlier work of Kemel et al. (2011) has suggested a relation of the form

$$\lambda = \Phi(v_{\rm A}^{\rm top}, g/c_s^2, q_{p0}, \beta_{\rm crit}) - \nu_t k_\nu^2 - \eta_t k_\eta^2, \qquad (8)$$

where k_ν and k_η are inverse length scales quantifying the effects of turbulent viscosity and turbulent magnetic diffusivity, Φ is a function of the Alfvén speed at the top, $v_{\rm A}^{\rm top}$, the inverse scale height $H_\rho^{-1} = g/c_s^2$, and other parameters describing the functional form of q_p.

We now need to determine the various unknowns. We begin by determining k_ν and k_η by varying either only ν_t or only η_t at a time. In this way we obtain a linear fit for the growth rate, $\lambda(\eta_t) = {\rm const} - \eta_t k_\eta^2$, giving us k_η^2 as the slope of this graph; see the upper and lower panels of Fig. 5 for the corresponding results for k_ν and k_η, respectively. It turns out that $k_\nu \approx 0.77\,k_1$ and $k_\eta \approx 1.1\,k_1$. The surprising result is that k_ν and k_η are different from each other by a factor of about $\sqrt{2}$. This was not the case in the earlier work of Kemel et al. (2011) using less accurate data. The new data seem sufficiently accurate so that this discrepancy cannot easily be explained by numerical errors. More plausibly, this discrepancy could be explained by a residual dependence of Φ on either ν_t or η_t, or both. Note, however, that the turbulent magnetic Prandtl number is of order unity (Kleeorin & Rogachevskii 1994; Yousef et al. 2003), so this uncertainty should be of no practical relevance.

Accepting now the fit parameters k_ν and k_η as they have been measured, we can proceed to determining the dependence of Φ on $v_{\rm A}^{\rm top}$, H_ρ, and other fit physical input param-

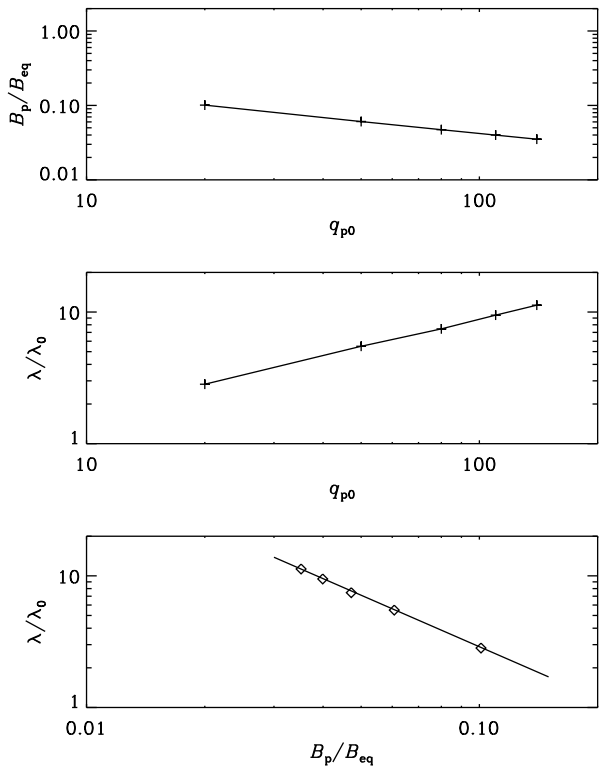

Fig. 4 Dependence of the fit parameter $B_{\rm p}$ on $q_{\rm p0}$, the corresponding growth rate λ, and the dependence of λ on $B_{\rm p}$. Here, λ is normalized by $\lambda_0 \equiv g/c_{\rm s}$.

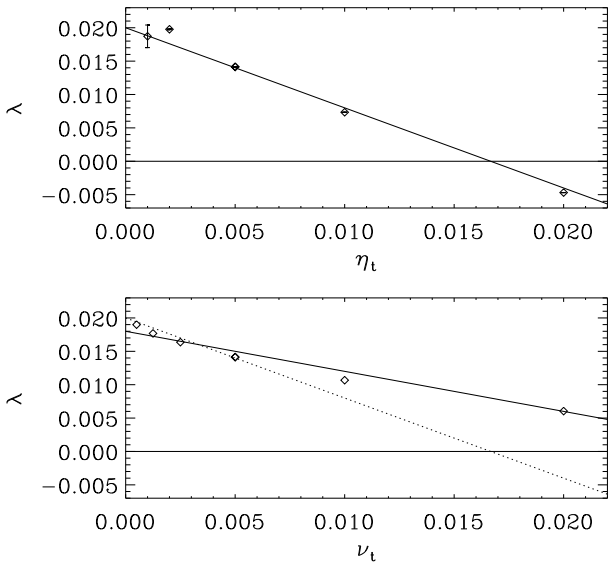

Fig. 5 Dependence of λ on $\eta_{\rm t}$ (upper panel) and $\nu_{\rm t}$ (lower panel). In the two panels, the straight lines represent the negative slopes $k_\eta^2 \approx 1.2$ and $k_\nu^2 \approx 0.6$, approximately. In the lower panel, the dotted line gives, for comparison, the negative slope 1.2 of the upper panel.

eters. We assume that this relation is multiplicative and find first the dependence on $v_{\rm A}^{\rm top}$ by plotting $\Phi = \lambda + \nu_{\rm t} k_\nu^2 + \eta_{\rm t} k_\eta^2$ against $v_{\rm A}^{\rm top}$. It turns out that this is nearly a linear relationship. Thus, keeping all other parameters unchanged, we find Φ as a function of $v_{\rm A}^{\rm top}$; see the first panel of Fig. 6. Next, we find Φ as a function of $g/c_{\rm s}^2$, which results in an exponential relationship, where $\ln \Phi$ is found to increase linearly with $g/c_{\rm s}^2 \equiv H_\rho^{-1}$; see the middle panel of Fig. 6. Thus, we can write $\ln \Phi \propto 1/k_\rho H_\rho$, where k_ρ is a new fit parameter. Here, $k_\rho \approx 0.5\, k_1$. Finally, we show in the third panel of Fig. 6 the dependence of Φ on the reconstructed fit,

$$\Phi_{\rm fit} = v_{\rm A}^{\rm top} k_{\rm A} \exp(1/k_\rho H_\rho)\, \varphi(q_{\rm p0}, \beta_{\rm p}), \qquad (9)$$

where $k_{\rm A} \approx 0.26\, k_1$ gives the best fit. This combined fit appears reasonably accurate for most of the parameter regime, substantiating thus the general validity of the fit formulae (8)–(9).

Some comments about the system size are in order. In all cases with $q_{\rm s0} = 0$, we find that in three-dimensional calculations with finite y extent, the value of L_y affects the growth rates only slightly; see Table 1. On the other hand, doubling the x extent yields two pairs of rolls, but at a slightly lower growth rate, indicating that our standard value of L_x is still not quite in the asymptotic regime. Extending the domain downward (in the negative z direction)

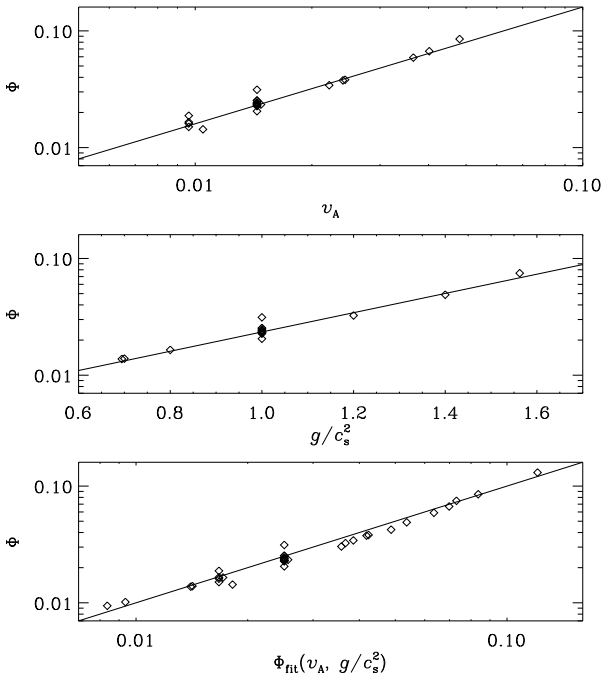

Fig. 6 Dependence of $\tilde{\lambda}$ on $v_{\rm A}^{\rm top}$ (upper panel), $g/c_{\rm s}^2$ (middle panel), and the combined fit $\Phi(v_{\rm A}^{\rm top}, g/c_{\rm s}^2)$ (lower panel).

does not change the results at all, but extending it in the upward direction (positive z direction) changes the value of

$\rho_{\rm top}$ and hence the value of $v_{\rm A}^{\rm top}$ in a way that is already fully described by our scaling law in Eq. (9).

4 Conclusions

The present work has clarified a number of puzzling aspects of NEMPI. Firstly, it is now clear that we can proceed with two-dimensional simulations as long as we know that $q_{\rm s0}=0$ (or negative). However, this may not always be the case. The fact that three-dimensional structures can emerge from NEMPI was initially thought to be an interesting aspect, because it could readily explain the formation of bipolar regions (BKR). However, given that simulations now indicate that $q_{\rm s0}\approx 0$ (or perhaps even negative), this proposal would no longer be an option, unless some other as yet unexplored effect begins to play a role. In principle, all turbulent transport processes are nonlocal and must be described by a convolution with the mean field rather than a multiplication. In Fourier space, the convolution corresponds to a multiplication with a scale-dependent turbulent transport coefficient. Thus, the idea of explaining bipolar regions would again become viable if this effect only existed at intermediate length scales. This would be a task for future simulations to clarify, because none of the currently available techniques are yet equipped to addressing this possibility.

Next, we have seen that the degeneracy in the fit formula used for $q_{\rm p}(\beta)$ and $P_{\rm eff}(\beta)$ is significant in that different combinations of $q_{\rm p0}$ and $\beta_{\rm p}$ result in similar values of $\min(P_{\rm eff})$ and $\beta_{\rm crit}$, but the growth rates can still be quite different. This means that it is not sufficient to measure only $\min(P_{\rm eff})$ and $\beta_{\rm crit}$. Instead, to characterize the functional form of $P_{\rm eff}(\beta)$ more accurately, we need some other characteristics to represent the dependence of this function near the origin. One such possibility is to use the field strength for which the minimum of the effective magnetic pressure is reached.

Finally, we have tried to establish an approximate dispersion relation to predict the growth rate of NEMPI as a function of turbulent viscosity, turbulent magnetic diffusivity, mean field strength, and the strength of stratification. This formula may serve as a first orientation and can hopefully be improved further with future simulations. This formula can also be useful in connection with analytic estimates concerning the regimes when NEMPI is expected in DNS or under other more realistic circumstances.

Acknowledgments. We acknowledge the use of computing time at the Center for Parallel Computers at the Royal Institute of Technology in Sweden as well as the National Supercomputing Center in Linköping. This work was supported in part by the European Research Council under the AstroDyn project 227952 and the Swedish Research Council grant 621-2007-4064.

References

Brandenburg, A., von Rekowski, B.: 2001, A&A 379, 1153
Brandenburg, A., Kleeorin, N., Rogachevskii, I.: 2010, AN 331, 5 (BKR)
Brandenburg, A., Kemel, K., Kleeorin, N., Rogachevskii, I.: 2011, ApJ (submitted), arXiv:1005.5700 (BKKR)
Courvoisier A., Hughes D. W., Proctor M. R. E.: 2010, Proc. Roy. Soc. Lond. 466, 583
Frisch, U., She, Z. S., Sulem, P. L.: 1987, Physica 28D, 382
Käpylä, P. J., Mantere, M. J., Hackman, T.: 2011a, ApJ (submitted), arXiv:1106.6029
Käpylä, P. J., Brandenburg, A., Kleeorin, N., Mantere, M. J., Rogachevskii, I.: 2011b, MNRAS (submitted), arXiv:1104.4541
Kemel, K., Brandenburg, A., Kleeorin, N., Rogachevskii, I.: 2011, in Proc. IAU, Vol. 6, IAU Symp. S274 (eds.), *Advances in Plasma Astrophysics*, A. Bonanno, E. de Gouveia dal Pino, A. Kosovichev, p. 473
Kitiashvili, I. N., Kosovichev, A. G., Wray, A. A., Mansour, N. N.: 2010, ApJ 719, 307
Kleeorin, N., Mond, M., Rogachevskii, I. 1993, Phys. Fluids B, 5, 4128
Kleeorin, N., Mond, M., Rogachevskii, I.: 1996, A&A 307, 293
Kleeorin, N., Rogachevskii, I.: 1994, PhRvE 50, 2716
Kleeorin, N.I., Rogachevskii, I.V., Ruzmaikin, A.A.: 1989, Sov. Astron. Lett. 15, 274
Kleeorin, N.I., Rogachevskii, I.V., Ruzmaikin, A.A.: 1990, Sov. Phys. JETP 70, 878
Parker, E.N.: 1966, ApJ 145, 811
Priest, E.R.: 1982, *Solar Magnetohydrodynamics* (D. Reidel Publ. Co., Dordrecht)
Rädler, K.-H.: 1974, AN 295, 265
Rogachevskii, I., Kleeorin, N.: 2007, PhRvE 76, 056307
Rüdiger, G.: 1974, AN 295, 275
Rüdiger, G.: 1980, GApFD 16, 239
Rüdiger, G.: 1989, *Differential rotation and stellar convection: Sun and solar-type stars* (Gordon & Breach, New York)
Rüdiger, G., Hollerbach, R.: 2004, *The magnetic universe* (New York: Wiley-VCH, Weinheim)
Rüdiger, G., Tuominen, I., Krause, F., Virtanen, H.: 1986, A&A 166, 306
Tao, L., Weiss, N.O., Brownjohn, D.P., Proctor, M.R.E.: 1998, ApJ 496, L39
Tserkovnikov, Y. A.: 1960, Sov. Phys. Dokl., 5, 87
Yousef, T. A., Brandenburg, A., Rüdiger, G.: 2003, A&A 411, 321

III

Astronomy & Astrophysics manuscript no. paper
August 11, 2011

Turbulent transport in stratified and/or rotating turbulence

A. Brandenburg[1,2], K.-H. Rädler[3], and K. Kemel[1,2]

[1] NORDITA, AlbaNova University Center, Roslagstullsbacken 23, SE-10691 Stockholm, Sweden
[2] Department of Astronomy, AlbaNova University Center, Stockholm University, SE-10691 Stockholm, Sweden
[3] Astrophysical Institute Potsdam, An der Sternwarte 16, D-14482 Potsdam, Germany

August 11, 2011, Revision: 1.125

ABSTRACT

Context. The large-scale magnetic fields of stars and galaxies are often described using mean-field dynamo theory. At moderate magnetic Reynolds numbers, the transport coefficients which define the mean electromotive force can be determined from simulations. This applies analogously also to the mean-field theory of passive scalar transport.
Aims. In the case of axisymmetric turbulence, that is, turbulence with only one preferred direction, magnetic transport is governed by nine coefficients and passive scalar transport by four coefficients. All these coefficients are determined for turbulence in the presence of either rotation or density stratification or, if they are aligned to each other, of both. The kinematic problem is considered in which the magnetic field does not act back on the flow.
Methods. The test-field method is used where transport coefficients are determined by solving a set of equations with properly chosen mean magnetic fields or mean scalars. The method is adapted to mean fields which may depend on all thee space coordinates.
Results. Anisotropy of turbulent diffusion is found to be moderate in spite of rapid rotation or strong density stratification. Contributions to the mean electromotive force determined by the symmetric part of the gradient tensor of the magnetic field turn out to be important. In stratified rotating turbulence, the α effect is strongly anisotropic, suppressed along the rotation axis on large length scales, but strongly enhanced at intermediate length scales. Also the $\boldsymbol{\Omega}\times\overline{\boldsymbol{J}}$ effect is enhanced at intermediate length scales. The turbulent passive scalar diffusivity is typically almost twice as large as the magnetic turbulent diffusivity.
Conclusions. The method provides a powerful tool for analyzing transport properties of axisymmetric turbulence. A range of future applications is proposed. In the presence of rotation and stratification, all mentioned coefficients are non-vanishing. Some of those ignored in earlier investigations turn out to be of significant magnitude.

Key words. magnetohydrodynamics (MHD) – hydrodynamics – turbulence

1. Introduction

Stellar mixing length theory is a rudimentary description of turbulent convective energy transport. The mixing length theory of turbulent transport goes back to Prandtl (1925) and, in the stellar context, to Vitense (1953). The simplest form of turbulent transport is turbulent diffusion, which quantifies the mean flux of a given quantity, e.g., momentum, concentration of chemicals, specific entropy or magnetic fields, down the gradient of its mean value. In all these cases essentially a Fickian diffusion law is established, where the turbulent diffusion coefficient is proportional to the rms velocity of the turbulent eddies and the effective mean free path of the eddies or their correlation length.

Mean-field theories, which have been elaborated, e.g., for the behavior of magnetic fields or of passive scalars in turbulent media, go beyond this concept. In the case of magnetic fields, the effects of turbulence occur in a mean electromotive force, which is related to the mean magnetic field and its derivatives in a tensorial fashion. Examples for effects described by the mean magnetic field alone, without spatial derivatives, are the α-effect (Steenbeck et al., 1966) and the pumping of mean magnetic flux (Rädler, 1966, 1968; Roberts & Soward, 1975). Likewise the mean passive scalar flux contains a pumping effect (Elperin et al., 1996). In both the magnetic and the passive scalar cases turbulent diffusion occurs, which is in general anisotropic. The coupling between the mean electromotive force and the magnetic field and its derivatives, or mean passive scalar flux and the mean scalar and its derivatives, is given by turbulent transport coefficients.

On the analytic level of the theory the determination of these transport coefficients is only possible with some approximations. The most often used one is the second-order correlation approximation (SOCA), which has delivered so far many important results. Its applicability is however restricted to certain ranges of parameters like the magnetic Reynolds number or the Péclet number number. In spite of this restriction, SOCA is an invaluable tool, because it allows a rigorous treatment within the limits of its applicability. It is in particular important for testing numerical methods that apply in a wider range.

In recent years it has become possible to compute the full set of turbulent transport coefficients numerically from simulations of turbulent flows. The most accurate method for that is the test-field method (Schrinner et al., 2005, 2007). In addition to the equations describing laminar and turbulent flows, one solves a set of evolution equations for the small-scale magnetic or scalar fields which result from given mean fields, the test fields. By selecting a sufficient number of independent test fields, one obtains a corresponding number of mean electromotive forces or mean

scalar fluxes and can then compute in a unique way all the associated turbulent transport coefficients.

Most of the applications of the test-field method are based on spatial averages that are taken over two coordinates. In the magnetic case this approach has been applied to a range of different flows including isotropic homogeneous turbulence (Sur et al., 2008; Brandenburg et al., 2008a), homogeneous shear flow turbulence (Brandenburg et al., 2008b) without and with helicity (Mitra et al., 2009), and turbulent convection (Käpylä et al., 2009). One of the main results is that in the isotropic case, for magnetic Reynolds numbers $R_{\rm m}$ larger than unity, the turbulent diffusivity is given by $\frac{1}{3}\tau u_{\rm rms}^2$, where the correlation time τ is, to a good approximation, given by $\tau=(u_{\rm rms}k_{\rm f})^{-1}$. Here, $u_{\rm rms}$ is the rms velocity of the turbulent small-scale flow and $k_{\rm f}$ is the wavenumber of the energy-carrying eddies. For smaller $R_{\rm m}$, the turbulent diffusivity grows linearly with $R_{\rm m}$. Furthermore, if the turbulence is driven isotropically by polarized waves, the flow becomes helical and there is an α effect that, in the kinematic regime (for weak magnetic fields), is proportional to $\overline{\boldsymbol{\omega}\cdot\boldsymbol{u}}$, where $\boldsymbol{\omega}=\boldsymbol{\nabla}\times\boldsymbol{u}$ is the vorticity of the small-scale flow, $\boldsymbol{u}$. In the passive scalar case, test scalars are used to determine turbulent transport coefficients. Results have been obtained for anisotropic flows in the presence of rotation or strong magnetic fields (Brandenburg et al., 2009), linear shear (Madarassy & Brandenburg, 2010), and for irrotational flows (Rädler et al., 2011).

The present paper deals with the magnetic and the passive scaler case in the above sense. Its goal is to compute the transport coefficients for axisymmetric turbulence, that is, turbulence with one preferred direction, given by the presence of either rotation or density stratification, or both. Except for a few comparison cases, we always consider flows in a slab between stress-free boundaries. To facilitate comparison with earlier work on forced turbulence, we consider an isothermal layer even in the density-stratified case, i.e., there is no convection, and the flow is driven by a prescribed random forcing function just as we did in the case of homogeneous turbulence. This is similar to earlier work on forced homogeneous turbulence, but now we will be able to address questions regarding vertical pumping as well as helicity production and α effect in the presence of rotation.

2. Mean-field concept in turbulent transport

2.1. Mean electromotive force

The evolution of the magnetic field $\boldsymbol{B}$ in an electrically conducting fluid is assumed to obey the induction equation,

$$\frac{\partial\boldsymbol{B}}{\partial t}=\boldsymbol{\nabla}\times(\boldsymbol{U}\times\boldsymbol{B}-\eta\boldsymbol{J}), \tag{1}$$

where $\boldsymbol{U}$ is the velocity and η the microscopic magnetic diffusivity of the fluid, and $\boldsymbol{J}$ is defined by $\boldsymbol{J}=\boldsymbol{\nabla}\times\boldsymbol{B}$ (so that $\boldsymbol{J}/\mu_0$ with μ_0 being the magnetic permeability is the electric current density). We define mean fields as averages, assume that the averaging satisfies (exactly or approximately) the Reynolds rules, and denote averaged quantities by overbars. The mean magnetic field $\overline{\boldsymbol{B}}$ is then governed by

$$\frac{\partial\overline{\boldsymbol{B}}}{\partial t}=\boldsymbol{\nabla}\times\left(\overline{\boldsymbol{U}}\times\overline{\boldsymbol{B}}+\overline{\boldsymbol{\mathcal{E}}}-\eta\overline{\boldsymbol{J}}\right), \tag{2}$$

where $\overline{\boldsymbol{\mathcal{E}}}=\overline{\boldsymbol{u}\times\boldsymbol{b}}$ is the mean electromotive force resulting from the correlation of velocity and magnetic field fluctuations, $\boldsymbol{u}=\boldsymbol{U}-\overline{\boldsymbol{U}}$ and $\boldsymbol{b}=\boldsymbol{B}-\overline{\boldsymbol{B}}$.

We focus attention on the mean electromotive force $\overline{\boldsymbol{\mathcal{E}}}$ in cases in which the velocity fluctuations $\boldsymbol{u}$ constitute axisymmetric turbulence, that is, turbulence with one preferred direction, which we describe by the unit vector $\hat{\boldsymbol{e}}$. Until further notice we accept the traditional assumption according to which $\overline{\boldsymbol{\mathcal{E}}}$ in a given point in space and time is a linear homogeneous function of $\overline{\boldsymbol{B}}$ and its first spatial derivatives in this point. Then, $\overline{\boldsymbol{\mathcal{E}}}$ can be represented in the form

$$\begin{aligned}\overline{\boldsymbol{\mathcal{E}}} &= -\alpha_\perp\overline{\boldsymbol{B}}-(\alpha_\parallel-\alpha_\perp)(\hat{\boldsymbol{e}}\cdot\overline{\boldsymbol{B}})\hat{\boldsymbol{e}}-\gamma\hat{\boldsymbol{e}}\times\overline{\boldsymbol{B}}\\ &\quad -\beta_\perp\overline{\boldsymbol{J}}-(\beta_\parallel-\beta_\perp)(\hat{\boldsymbol{e}}\cdot\overline{\boldsymbol{J}})\hat{\boldsymbol{e}}-\delta\hat{\boldsymbol{e}}\times\overline{\boldsymbol{J}}\\ &\quad -\kappa_\perp\overline{\boldsymbol{K}}-(\kappa_\parallel-\kappa_\perp)(\hat{\boldsymbol{e}}\cdot\overline{\boldsymbol{K}})\hat{\boldsymbol{e}}-\mu\hat{\boldsymbol{e}}\times\overline{\boldsymbol{K}}\end{aligned} \tag{3}$$

with nine coefficients $\alpha_\perp$, $\alpha_\parallel$, ..., μ. [1] Like $\overline{\boldsymbol{J}}=\boldsymbol{\nabla}\times\overline{\boldsymbol{B}}$, also $\overline{\boldsymbol{K}}$ is determined by the gradient tensor $\boldsymbol{\nabla}\overline{\boldsymbol{B}}$. While $\overline{\boldsymbol{J}}$ is given by its antisymmetric part, $\overline{\boldsymbol{K}}$ is a vector defined by $\overline{\boldsymbol{K}}=\hat{\boldsymbol{e}}\cdot(\boldsymbol{\nabla}\overline{\boldsymbol{B}})^{\rm S}$ with $(\boldsymbol{\nabla}\overline{\boldsymbol{B}})^{\rm S}$ being the symmetric part of $\boldsymbol{\nabla}\overline{\boldsymbol{B}}$. A more detailed explanation of (3) is given in Appendix A. If $\hat{\boldsymbol{e}}$ is understood as polar vector (for example $\boldsymbol{\nabla}\overline{\varrho}/|\boldsymbol{\nabla}\overline{\varrho}|$, where $\overline{\varrho}$ is the mean mass density), then $\overline{\boldsymbol{K}}$ is axial and γ, $\beta_\perp$, $\beta_\parallel$ and μ are true scalars, but $\alpha_\perp$, $\alpha_\parallel$, δ, $\kappa_\perp$ and $\kappa_\parallel$ pseudoscalars. Sometimes it is useful to interpret $\hat{\boldsymbol{e}}$ as an axial vector (for example $\boldsymbol{\Omega}/|\boldsymbol{\Omega}|$ with $\boldsymbol{\Omega}$ being an angular velocity). Then, $\overline{\boldsymbol{K}}$ is a polar vector, $\beta_\perp$, $\beta_\parallel$, δ, $\kappa_\perp$, $\kappa_\parallel$ and μ are true scalars but $\alpha_\perp$, $\alpha_\parallel$ and γ pseudo scalars.

We may split $\overline{\boldsymbol{\mathcal{E}}}$ and $\overline{\boldsymbol{B}}$ into parts $\overline{\boldsymbol{\mathcal{E}}}_\perp$ and $\overline{\boldsymbol{B}}_\perp$ perpendicular to $\hat{\boldsymbol{e}}$ and parts $\overline{\boldsymbol{\mathcal{E}}}_\parallel$ and $\overline{\boldsymbol{B}}_\parallel$ parallel to it. Then (3) can be written in the form

$$\begin{aligned}\overline{\boldsymbol{\mathcal{E}}}_\perp &= -\alpha_\perp\overline{\boldsymbol{B}}_\perp-\gamma\hat{\boldsymbol{e}}\times\overline{\boldsymbol{B}}_\perp-\beta_\perp\overline{\boldsymbol{J}}_\perp-\delta\hat{\boldsymbol{e}}\times\overline{\boldsymbol{J}}_\perp\\ &\quad -\kappa_\perp\overline{\boldsymbol{K}}_\perp-\mu\hat{\boldsymbol{e}}\times\overline{\boldsymbol{K}}_\perp\\ \overline{\boldsymbol{\mathcal{E}}}_\parallel &= -\alpha_\parallel\overline{\boldsymbol{B}}_\parallel-\beta_\parallel\overline{\boldsymbol{J}}_\parallel-\kappa_\parallel\overline{\boldsymbol{K}}_\parallel.\end{aligned} \tag{4}$$

Let us return to (3). In the simple case of homogeneous isotropic turbulence we have $\alpha_\perp=\alpha_\parallel$ and $\beta_\perp=\beta_\parallel$, and all remaining coefficients vanish. Then, (3) takes the form $\overline{\boldsymbol{\mathcal{E}}}=\alpha\overline{\boldsymbol{B}}-\eta_{\rm t}\overline{\boldsymbol{J}}$ with properly defined α and $\eta_{\rm t}$. These two coefficients have been determined by test-field calculations (Sur et al., 2008; Brandenburg et al., 2008a).

In several previous studies of $\overline{\boldsymbol{\mathcal{E}}}$, more general kinds of turbulence (that is, not only axisymmetric turbulence) have been considered, but with a less general definition of mean fields, which were just horizontal averages. More precisely, Cartesian coordinates (x,y,z) were adopted and the averages were taken over all x and y so that they depend on z and t only (Brandenburg et al., 2008a,b). This definition implies remarkable simplifications. Of course, we then have $\overline{J}_z=0$. Further, there are no non-zero components of $\boldsymbol{\nabla}\overline{\boldsymbol{B}}$ other than $\overline{B}_{x,z}$ and $\overline{B}_{y,z}$, for $\boldsymbol{\nabla}\cdot\overline{\boldsymbol{B}}=0$ requires $\overline{B}_{z,z}=0$, and these components can be expressed as components of $\overline{\boldsymbol{J}}$, *viz.* $\overline{B}_{x,z}=\overline{J}_y$ and $\overline{B}_{y,z}=-\overline{J}_x$. (Here and in what follows, commas denote partial derivatives.) This again implies $\overline{\boldsymbol{K}}=-\frac{1}{2}\,\hat{\boldsymbol{e}}\times\overline{\boldsymbol{J}}$. As a consequence, this definition of

[1] Note that the signs in front of some individual terms on the right-hand side of (3), in particular of those with $\alpha_\perp$, $\alpha_\parallel$ and γ, may differ from the signs used in other representations.

mean fields reduces (3) to

$$\overline{\boldsymbol{\mathcal{E}}} = -\alpha_\perp \overline{\boldsymbol{B}} - (\alpha_\parallel - \alpha_\perp)(\hat{\boldsymbol{e}}\cdot\overline{\boldsymbol{B}})\hat{\boldsymbol{e}} - \gamma \hat{\boldsymbol{e}}\times\overline{\boldsymbol{B}} - \beta^\dagger \overline{\boldsymbol{J}} - \delta^\dagger\, \hat{\boldsymbol{e}}\times\overline{\boldsymbol{J}}\,, \tag{5}$$

where $\beta^\dagger = \beta_\perp + \frac{1}{2}\mu$ and $\delta^\dagger = \delta - \frac{1}{2}\kappa_\perp$. Of course, $\alpha_\perp$, $\alpha_\parallel$, γ, $\beta^\dagger$ and $\delta^\dagger$ are independent of x or y. Clearly, $\beta_\perp$ and μ as well as δ and $\kappa_\perp$ have no longer independent meanings. From (2) we may conclude that $\partial\overline{B}_z/\partial t = 0$. If we restrict ourselves to applications in which $\overline{B}_z$ vanishes initially, it does so at all times and the term with $\alpha_\parallel - \alpha_\perp$ in (5) disappears. Then, only the four coefficients $\alpha_\perp$, γ, $\beta^\dagger$ and $\delta^\dagger$ are of interest. They can be determined by test-field calculations using two test fields independent of x and y (Brandenburg et al., 2008a,b).

In this paper we go in several respect beyond the assumptions mentioned so far. Firstly, we relax the assumption that $\overline{\boldsymbol{\mathcal{E}}}$ in a given point in space is a homogeneous function of $\overline{\boldsymbol{B}}$ and its first spatial derivatives in this point. Instead, we admit a non-local connection between $\overline{\boldsymbol{\mathcal{E}}}$ and $\overline{\boldsymbol{B}}$. For simplicity, however, we further on assume that $\overline{\boldsymbol{\mathcal{E}}}$ at a given time depends only on $\overline{\boldsymbol{B}}$ at the same time, that is, we remain with an instantaneous connection between $\overline{\boldsymbol{\mathcal{E}}}$ and $\overline{\boldsymbol{B}}$. Secondly, we consider mean fields no longer as averages over all x and y. We define $\overline{\boldsymbol{B}}$ at a point (x,y) in a plane $z=$ const by averaging over some surroundings of this point in this plane so that it still depends on x and y. In that sense we generalize (3) so that

$$\begin{aligned}\overline{\boldsymbol{\mathcal{E}}}(\boldsymbol{x}) = -\int\big(&\alpha_\perp(\boldsymbol{x},\boldsymbol{\xi})\overline{\boldsymbol{B}}(\boldsymbol{x}-\boldsymbol{\xi})\\ &+\big(\alpha_\parallel(\boldsymbol{x},\boldsymbol{\xi})-\alpha_\perp(\boldsymbol{x},\boldsymbol{\xi})\big)\big(\hat{\boldsymbol{e}}\cdot\overline{\boldsymbol{B}}(\boldsymbol{x}-\boldsymbol{\xi})\big)\hat{\boldsymbol{e}}\\ &+\gamma(\boldsymbol{x},\boldsymbol{\xi})\,\hat{\boldsymbol{e}}\times\overline{\boldsymbol{B}}(\boldsymbol{x}-\boldsymbol{\xi})\\ &+\beta_\perp(\boldsymbol{x},\boldsymbol{\xi})\,\overline{\boldsymbol{J}}(\boldsymbol{x}-\boldsymbol{\xi})\\ &+\big(\beta_\parallel(\boldsymbol{x},\boldsymbol{\xi})-\beta_\perp(\boldsymbol{x},\boldsymbol{\xi})\big)\big(\hat{\boldsymbol{e}}\cdot\overline{\boldsymbol{J}}(\boldsymbol{x}-\boldsymbol{\xi})\big)\hat{\boldsymbol{e}}\\ &+\delta(\boldsymbol{x},\boldsymbol{\xi})\,\hat{\boldsymbol{e}}\times\overline{\boldsymbol{J}}(\boldsymbol{x}-\boldsymbol{\xi})\\ &+\kappa_\perp(\boldsymbol{x},\boldsymbol{\xi})\,\overline{\boldsymbol{K}}(\boldsymbol{x}-\boldsymbol{\xi})\\ &+\big(\kappa_\parallel(\boldsymbol{x},\boldsymbol{\xi})-\kappa_\perp(\boldsymbol{x},\boldsymbol{\xi})\big)\big(\hat{\boldsymbol{e}}\cdot\overline{\boldsymbol{K}}(\boldsymbol{x}-\boldsymbol{\xi})\big)\hat{\boldsymbol{e}}\\ &+\mu(\boldsymbol{x},\boldsymbol{\xi})\,\hat{\boldsymbol{e}}\times\overline{\boldsymbol{K}}(\boldsymbol{x}-\boldsymbol{\xi})\big)\,\mathrm{d}^3\xi\,.\end{aligned} \tag{6}$$

As a consequence of the axisymmetry of the turbulence, the coefficients $\alpha_\perp$, $\alpha_\parallel$, ..., μ depend only via $\xi_x^2+\xi_y^2$ on ξ_x and ξ_y. We consider them also as symmetric in ξ_z. The integration is over all $\boldsymbol{\xi}$ space. Of course, $\overline{\boldsymbol{\mathcal{E}}}$, $\overline{\boldsymbol{B}}$, $\overline{\boldsymbol{J}}$, and $\overline{\boldsymbol{K}}$ may depend on t. For simplicity, however, the argument t has been dropped.

Let us subject (6) to a Fourier transformation with respect to $\boldsymbol{\xi}$. We define it by

$$F(\boldsymbol{\xi}) = (2\pi)^{-3}\int \tilde{F}(\boldsymbol{k})\,\exp(\mathrm{i}\boldsymbol{k}\cdot\boldsymbol{\xi})\,\mathrm{d}^3k\,. \tag{7}$$

In this way we obtain

$$\begin{aligned}\overline{\boldsymbol{\mathcal{E}}}(\boldsymbol{x}) = -\int\Big(&\tilde{\alpha}_\perp(\boldsymbol{x},\boldsymbol{k})\tilde{\overline{\boldsymbol{B}}}(\boldsymbol{k})\\ &+\big(\tilde{\alpha}_\parallel(\boldsymbol{x},\boldsymbol{k})-\tilde{\alpha}_\perp(\boldsymbol{x},\boldsymbol{k})\big)\big(\hat{\boldsymbol{e}}\cdot\tilde{\overline{\boldsymbol{B}}}(\boldsymbol{k})\big)\,\hat{\boldsymbol{e}}\\ &+\tilde{\gamma}(\boldsymbol{x},\boldsymbol{k})\,\hat{\boldsymbol{e}}\times\tilde{\overline{\boldsymbol{B}}}(\boldsymbol{k})\\ &+\tilde{\beta}_\perp(\boldsymbol{x},\boldsymbol{k})\,\tilde{\overline{\boldsymbol{J}}}(\boldsymbol{k})+\big(\tilde{\beta}_\parallel(\boldsymbol{x},\boldsymbol{k})-\tilde{\beta}_\perp(\boldsymbol{x},\boldsymbol{k})\big)\big(\hat{\boldsymbol{e}}\cdot\tilde{\overline{\boldsymbol{J}}}(\boldsymbol{k})\big)\,\hat{\boldsymbol{e}}\\ &+\tilde{\delta}(\boldsymbol{x},\boldsymbol{k})\,\hat{\boldsymbol{e}}\times\tilde{\overline{\boldsymbol{J}}}(\boldsymbol{k})\\ &+\tilde{\kappa}_\perp(\boldsymbol{x},\boldsymbol{k})\tilde{\overline{\boldsymbol{K}}}(\boldsymbol{k})+\big(\tilde{\kappa}_\parallel(\boldsymbol{x},\boldsymbol{k})-\tilde{\kappa}_\perp(\boldsymbol{x},\boldsymbol{k})\big)\big(\hat{\boldsymbol{e}}\cdot\tilde{\overline{\boldsymbol{K}}}(\boldsymbol{k})\big)\,\hat{\boldsymbol{e}}\\ &+\tilde{\mu}(\boldsymbol{x},\boldsymbol{k})\,\hat{\boldsymbol{e}}\times\tilde{\overline{\boldsymbol{K}}}(\boldsymbol{k})\Big)\,\exp(\mathrm{i}\boldsymbol{k}\cdot\boldsymbol{x})\,\mathrm{d}^3\boldsymbol{k}\,;\end{aligned} \tag{8}$$

see Chatterjee et al. (2011) for a corresponding relation in the case of horizontally averaged magnetic fields that depend only on z. Like $\alpha_\perp$, $\alpha_\parallel$, ..., μ, the $\tilde{\alpha}_\perp$, $\tilde{\alpha}_\parallel$, ..., $\tilde{\mu}$ are real quantities. They depend only via $k_\perp = (k_x^2+k_y^2)^{1/2}$ on k_x and k_y and are symmetric in k_z, i.e., depend only via $k_\parallel = |k_z|$ on k_z. Due to the reality of the $\alpha_\perp$, $\alpha_\parallel$, ..., μ and their symmetry in ξ_x, ξ_y and ξ_z we have

$$\tilde{\alpha}_\perp(\boldsymbol{x},\boldsymbol{k}) = \int \alpha_\perp(\boldsymbol{x},\boldsymbol{\xi})\,\cos k_x\xi_x\,\cos k_y\xi_y\,\cos k_z\xi_z\,\mathrm{d}^3\xi \tag{9}$$

and analogous relations for $\tilde{\alpha}_\parallel$, ..., $\tilde{\mu}$. We note that $\tilde{\alpha}_\perp$, ..., $\tilde{\mu}$, taken at $\boldsymbol{k}=\boldsymbol{0}$, agree with $\alpha_\perp$, ..., μ in Equation (3).

2.2. Mean passive scalar flux

There are interesting analogies between turbulent transport of magnetic flux and that of a passive scalar (cf. Rädler et al., 2011). Assume that the evolution of a passive scalar C, e.g., the concentration of an admixture in a fluid, is given by

$$\frac{\partial C}{\partial t} = -\boldsymbol{\nabla}\cdot(\boldsymbol{U}C - D\boldsymbol{\nabla}C), \tag{10}$$

where D is the microscopic (molecular) diffusivity. Then the mean scalar $\overline{C}$ has to satisfy

$$\frac{\partial \overline{C}}{\partial t} = -\boldsymbol{\nabla}\cdot(\overline{\boldsymbol{U}C} + \overline{\boldsymbol{\mathcal{F}}} - D\boldsymbol{\nabla}\overline{C}), \tag{11}$$

where $\overline{\boldsymbol{\mathcal{F}}} = \overline{\boldsymbol{u}c}$ is the mean passive scalar flux, $\boldsymbol{u}$ stands again for the fluctuations of the velocity and $c = C - \overline{C}$ for the fluctuations of C. Consider again axisymmetric turbulence with a preferred direction given by the unit vector $\hat{\boldsymbol{e}}$. Assume that $\overline{\boldsymbol{\mathcal{F}}}$ in a given point in space and time is determined by $\overline{C}$ and its gradient $\overline{\boldsymbol{G}} = \boldsymbol{\nabla}\overline{C}$ in this point. Then we have

$$\overline{\boldsymbol{\mathcal{F}}} = -\gamma^C\overline{C}\hat{\boldsymbol{e}} - \beta_\perp^C\overline{\boldsymbol{G}} - (\beta_\parallel^C - \beta_\perp^C)(\hat{\boldsymbol{e}}\cdot\overline{\boldsymbol{G}})\hat{\boldsymbol{e}} - \delta^C\hat{\boldsymbol{e}}\times\overline{\boldsymbol{G}}, \tag{12}$$

with coefficients γ^C, $\beta_\perp^C$, $\beta_\parallel^C$ and δ^C. If $\hat{\boldsymbol{e}}$ is a polar vector, γ^C is a scalar but δ^C a pseudoscalar, and if $\hat{\boldsymbol{e}}$ is an axial vector, γ^C is a pseudoscalar but δ^C a scalar, while $\beta_\perp^C$ and $\beta_\parallel^C$ are always scalars. We note that $\boldsymbol{\nabla}\cdot(\delta^C\hat{\boldsymbol{e}}\times\overline{\boldsymbol{G}})$ is only unequal zero if δ^C is not constant but varies in the direction of $\hat{\boldsymbol{e}}\times\overline{\boldsymbol{G}}$. We may split $\overline{\boldsymbol{\mathcal{F}}}$ and $\overline{\boldsymbol{G}}$ into parts $\overline{\boldsymbol{\mathcal{F}}}_\perp$ and $\overline{\boldsymbol{G}}_\perp$ perpendicular to $\hat{\boldsymbol{e}}$, and parts $\overline{\boldsymbol{\mathcal{F}}}_\parallel$ and $\overline{\boldsymbol{G}}_\parallel$ parallel to it, and give (12) the form

$$\begin{aligned}\overline{\boldsymbol{\mathcal{F}}}_\perp &= -\beta_\perp^C\overline{\boldsymbol{G}}_\perp - \delta^C\hat{\boldsymbol{e}}\times\overline{\boldsymbol{G}}_\perp\\ \overline{\boldsymbol{\mathcal{F}}}_\parallel &= -\gamma^C\hat{\boldsymbol{e}}\overline{C} - \beta_\parallel^C\overline{\boldsymbol{G}}_\parallel.\end{aligned} \tag{13}$$

Let us now relax the assumption that $\overline{\boldsymbol{\mathcal{F}}}$ in a given point in space and time is determined by $\overline{C}$ and $\overline{\boldsymbol{G}}$ in this point. Analogously to the magnetic case we consider a non-local

but instantaneous connection between $\overline{\boldsymbol{\mathcal{F}}}$ and $\overline{C}$. Then we have

$$\begin{aligned}\overline{\boldsymbol{\mathcal{F}}}(\boldsymbol{x}) \;=\; -\int \Big(&\gamma^C(\boldsymbol{x},\boldsymbol{\xi})\,\hat{\boldsymbol{e}}\,\overline{C}(\boldsymbol{x}-\boldsymbol{\xi})\\ &+\beta_\perp^C(\boldsymbol{x},\boldsymbol{\xi})\overline{\boldsymbol{G}}(\boldsymbol{x}-\boldsymbol{\xi})\\ &+\big(\beta_\parallel^C(\boldsymbol{x},\boldsymbol{\xi})-\beta_\perp^C(\boldsymbol{x},\boldsymbol{\xi})\big)\,\big(\hat{\boldsymbol{e}}\cdot\overline{\boldsymbol{G}}(\boldsymbol{x}-\boldsymbol{\xi})\big)\,\hat{\boldsymbol{e}}\\ &+\delta^C(\boldsymbol{x},\boldsymbol{\xi})\,\hat{\boldsymbol{e}}\times\overline{\boldsymbol{G}}(\boldsymbol{x}-\boldsymbol{\xi})\Big)\,\mathrm{d}^3\xi\,.\end{aligned}\tag{14}$$

As $\alpha_\perp$, $\alpha_\parallel$, ..., μ in the magnetic case, γ^C, $\beta_\perp^C$, $\beta_\parallel^C$ and δ^C depend only via $\xi_x^2+\xi_y^2$ on ξ_x and ξ_y, and we consider them also as symmetric in ξ_z. The integration is again over all $\boldsymbol{\xi}$ space. Note that $\overline{\boldsymbol{\mathcal{F}}}$, $\overline{C}$, and $\overline{\boldsymbol{G}}$ may, even if it is not explicitly indicated, depend on t. Applying the Fourier transformation defined by (7) on (14), we arrive at

$$\begin{aligned}\overline{\boldsymbol{\mathcal{F}}}(\boldsymbol{x}) \;=\; -\int \Big(&\tilde{\gamma}^C(\boldsymbol{x},\boldsymbol{k})\,\hat{\boldsymbol{e}}\,\tilde{\overline{C}}(\boldsymbol{k})\\ &+\tilde{\beta}_\perp^C(\boldsymbol{x},\boldsymbol{k})\tilde{\overline{\boldsymbol{G}}}(\boldsymbol{k})\\ &+\big(\tilde{\beta}_\parallel^C(\boldsymbol{x},\boldsymbol{k})-\tilde{\beta}_\perp^C(\boldsymbol{x},\boldsymbol{k})\big)\,\big(\hat{\boldsymbol{e}}\cdot\tilde{\overline{\boldsymbol{G}}}(\boldsymbol{k})\big)\,\hat{\boldsymbol{e}}\\ &+\tilde{\delta}^C(\boldsymbol{x},\boldsymbol{k})\,\hat{\boldsymbol{e}}\times\tilde{\overline{\boldsymbol{G}}}(\boldsymbol{k})\Big)\,\exp(\mathrm{i}\boldsymbol{k}\cdot\boldsymbol{x})\,\mathrm{d}^3k\,,\end{aligned}\tag{15}$$

where $\tilde{\gamma}_\perp^C$, $\tilde{\beta}_\perp^C$, $\tilde{\beta}_\parallel^C$ and $\tilde{\delta}^C$ are real quantities. They depend only via $k_x^2+k_y^2$ on k_x and k_y, and only via $k_\parallel$ on k_z, and they satisfy relations analogous to (9). We note that $\tilde{\gamma}^C$, $\tilde{\beta}_\perp^C$, $\tilde{\beta}_\parallel^C$, and $\tilde{\delta}^C$ at $\boldsymbol{k}=\boldsymbol{0}$ agree with γ^C, $\beta_\perp^C$, $\beta_\parallel^C$, and δ^C in (12).

3. Simulating the turbulence

We assume that the fluid is compressible and its flow is governed by the equations

$$\begin{aligned}\frac{\mathrm{D}\boldsymbol{U}}{\mathrm{D}t} &= \boldsymbol{f}+\boldsymbol{g}-\boldsymbol{\nabla}h-2\boldsymbol{\Omega}\times\boldsymbol{U}+\rho^{-1}\boldsymbol{\nabla}\cdot(2\nu\rho\mathbf{S})\\ \frac{\mathrm{D}h}{\mathrm{D}t} &= -c_\mathrm{s}^2\boldsymbol{\nabla}\cdot\boldsymbol{U}\,.\end{aligned}\tag{16}$$

Here, $\boldsymbol{f}$ means a random force which drives isotropic turbulence (e.g., Haugen et al., 2004), $\boldsymbol{g}$ the gravitational force, and h the specific enthalpy. An isothermal equation of state, $p=\rho c_\mathrm{s}^2$, has been adopted with a constant isothermal sound speed c_s. In general a fluid flow in a rotating system is considered, where $\boldsymbol{\Omega}$ is the angular velocity which defines the Coriolis force. As usual ρ means the mass density, ν the kinematic viscosity and $\mathbf{S}$ the trace-free rate of strain tensor, $\mathsf{S}_{ij}=\frac{1}{2}(\partial U_{i,j}+\partial U_{j,i})-\frac{1}{3}\delta_{ij}\boldsymbol{\nabla}\cdot\boldsymbol{U}$. The influence of the magnetic field on the fluid motion, that is the Lorentz force, is ignored throughout the paper.

We consider a cubic domain of size L^3, so the smallest wavenumber is $k_1=2\pi/L$. In most of the cases a density stratification is included with $\boldsymbol{g}=(0,0,-g)$, so the density scale height is $H_\rho=c_\mathrm{s}^2/g$. The number of scale heights across the domain, L/H_ρ, is equal to $\Delta\ln\rho$, where Δ denotes the difference of values at the two edges of the domain. For $H_\rho=L$ we have a density contrast of $\exp 2\pi\approx 535$. The forcing is assumed to work with an average wavenumber k_f. The scale separation ratio is then given by k_f/k_1, for which we usually adopt the value 5. This means that we have about 5 eddies in each of the three coordinate directions.

The flow inside the considered domain depends on the boundary conditions. Unless indicated otherwise we take the top and bottom surfaces $z=z_1$ and $z=z_2$ with $z_2=-z_1=L/2$ as stress-free and adopt periodic boundary conditions for the other surfaces.

4. Computing the transport coefficients

4.1. Test-field method

In the magnetic case the coefficients $\alpha_\perp$, $\alpha_\parallel$, ..., μ are determined by the test-field method (Schrinner et al., 2005, 2007; Brandenburg et al., 2008a). This method works with a set of test fields $\overline{\boldsymbol{B}}$, called $\overline{\boldsymbol{B}}^\mathrm{T}$, and the corresponding mean electromotive forces $\overline{\boldsymbol{\mathcal{E}}}$, called $\overline{\boldsymbol{\mathcal{E}}}^\mathrm{T}$. For the latter we have $\overline{\boldsymbol{\mathcal{E}}}^\mathrm{T}=\overline{\boldsymbol{u}\times\boldsymbol{b}^\mathrm{T}}$, where the $\boldsymbol{b}^\mathrm{T}$ obey

$$\begin{aligned}\boldsymbol{b}^T &= \boldsymbol{\nabla}\times\boldsymbol{a}^T\\ \frac{\partial\boldsymbol{a}^T}{\partial t} &= \overline{\boldsymbol{U}}\times\boldsymbol{b}^T+\boldsymbol{u}\times\boldsymbol{B}^T+(\boldsymbol{u}\times\boldsymbol{b}^T)'+\eta\nabla^2\boldsymbol{a}^T\,,\end{aligned}\tag{17}$$

with $\overline{\boldsymbol{U}}$ and $\boldsymbol{u}$ taken from the solutions of (16). For the boundaries $z=$ const we choose conditions which correspond to an adjacent perfect conductor, for the x and y directions periodic boundary conditions.

We define four test fields by

$$\begin{aligned}\overline{\boldsymbol{B}}^{1\mathrm{s}} &= (B_0\,\mathrm{s}x\,\mathrm{s}y\,\mathrm{s}z,0,0)\,,\quad \overline{\boldsymbol{B}}^{1\mathrm{c}}=(B_0\,\mathrm{s}x\,\mathrm{s}y\,\mathrm{c}z,0,0)\\ \overline{\boldsymbol{B}}^{2\mathrm{s}} &= (0,0,B_0\,\mathrm{s}x\,\mathrm{s}y\,\mathrm{s}z)\,,\quad \overline{\boldsymbol{B}}^{2\mathrm{c}}=(0,0,B_0\,\mathrm{s}x\,\mathrm{s}y\,\mathrm{c}z)\end{aligned}\tag{18}$$

with a constant B_0. Here and in what follows we use the abbreviations

$$\begin{aligned}\mathrm{s}x &= \sin k_x x\,,\quad \mathrm{c}x=\cos k_x x\\ \mathrm{s}y &= \sin k_y y\,,\quad \mathrm{c}y=\cos k_y y\\ \mathrm{s}z &= \sin k_z z\,,\quad \mathrm{c}z=\cos k_z z\,.\end{aligned}\tag{19}$$

We recall that test-fields need not to be solenoidal (see Schrinner et al., 2005, 2007).

We denote the mean electromotive forces which correspond to the test fields (18) by $\overline{\boldsymbol{\mathcal{E}}}^{1\mathrm{s}}$, $\overline{\boldsymbol{\mathcal{E}}}^{1\mathrm{c}}$, $\overline{\boldsymbol{\mathcal{E}}}^{2\mathrm{s}}$, and $\overline{\boldsymbol{\mathcal{E}}}^{2\mathrm{c}}$. With the presentation (6) and relations like (9) we find

$$\begin{aligned}\overline{\mathcal{E}}_x^{1\mathrm{s}} &= -B_0\big(\tilde{\alpha}_\perp\,\mathrm{s}x\,\mathrm{s}y\,\mathrm{s}z-(\tilde{\delta}-\frac{1}{2}\tilde{\kappa}_\perp)k_z\,\mathrm{s}x\,\mathrm{s}y\,\mathrm{c}z\big)\\ \overline{\mathcal{E}}_y^{1\mathrm{s}} &= -B_0\big(\tilde{\gamma}\,\mathrm{s}x\,\mathrm{s}y\,\mathrm{s}z+(\tilde{\beta}_\perp+\frac{1}{2}\tilde{\mu})k_z\,\mathrm{s}x\,\mathrm{s}y\,\mathrm{c}z\big)\\ \overline{\mathcal{E}}_z^{1\mathrm{s}} &= B_0\,\tilde{\beta}_\parallel k_y\,\mathrm{s}x\,\mathrm{c}y\,\mathrm{s}z\\ \overline{\mathcal{E}}_x^{2\mathrm{s}} &= -B_0\big((\tilde{\beta}_\perp-\frac{1}{2}\tilde{\mu})k_y\,\mathrm{s}x\,\mathrm{c}y\,\mathrm{s}z+(\tilde{\delta}+\frac{1}{2}\tilde{\kappa}_\perp)k_x\,\mathrm{c}x\,\mathrm{s}y\,\mathrm{s}z\big)\\ \overline{\mathcal{E}}_y^{2\mathrm{s}} &= B_0\big((\tilde{\beta}_\perp-\frac{1}{2}\tilde{\mu})k_x\,\mathrm{c}x\,\mathrm{s}y\,\mathrm{s}z-(\tilde{\delta}+\frac{1}{2}\tilde{\kappa}_\perp)k_y\,\mathrm{s}x\,\mathrm{c}y\,\mathrm{s}z\big)\\ \overline{\mathcal{E}}_z^{2\mathrm{s}} &= -B_0\big(\tilde{\alpha}_\parallel\,\mathrm{s}x\,\mathrm{s}y\,\mathrm{s}z+\tilde{\kappa}_\parallel k_z\,\mathrm{s}x\,\mathrm{s}y\,\mathrm{c}z\big)\end{aligned}\tag{20}$$

and corresponding relations for $\overline{\mathcal{E}}_x^{1\mathrm{c}},\ldots,\overline{\mathcal{E}}_x^{2\mathrm{c}}$, whose right-hand sides can be derived from those in (20) simply by replacing $\mathrm{s}z$ and $\mathrm{c}z$ by $\mathrm{c}z$ and $-\mathrm{s}z$, respectively.

In view of the assumed axisymmetry of the turbulence, we consider $\alpha_\perp$, $\alpha_\parallel$, ..., μ in what follows as independent of x and y but admit a dependence on z. When multiplying both sides of the equations (20) and of the corresponding

ones for $\overline{\mathcal{E}}{}^{\rm 1c}_x,\ldots,\overline{\mathcal{E}}{}^{\rm 2c}_x$ with $\mathrm{s}x\,\mathrm{s}y$, $\mathrm{s}x\,\mathrm{c}y$ or $\mathrm{c}y\,\mathrm{s}y$ and averaging over all x and y, we obtain a system of equations, which can be solved for $\tilde\alpha_\perp$, $\tilde\alpha_\parallel$, ..., $\tilde\mu$. The result reads

$$\begin{aligned}
\tilde\alpha_\perp &= -\langle b^{ss}(\,\mathrm{s}z\overline{\mathcal{E}}{}^{\rm 1s}_x+\,\mathrm{c}z\overline{\mathcal{E}}{}^{\rm 1c}_x)\rangle\\
\tilde\alpha_\parallel &= -\langle b^{ss}(\,\mathrm{s}z\overline{\mathcal{E}}{}^{\rm 2s}_z+\,\mathrm{c}z\overline{\mathcal{E}}{}^{\rm 2c}_z)\rangle\\
\tilde\gamma &= -\langle b^{ss}(\,\mathrm{s}z\overline{\mathcal{E}}{}^{\rm 1s}_y+\,\mathrm{c}z\overline{\mathcal{E}}{}^{\rm 1c}_y)\rangle\\
\tilde\beta_\perp &= -\tfrac{1}{2}\langle B^{ss}(\,\mathrm{c}z\overline{\mathcal{E}}{}^{\rm 1s}_y-\,\mathrm{s}z\overline{\mathcal{E}}{}^{\rm 1c}_y)+B^{sc}(\,\mathrm{s}z\overline{\mathcal{E}}{}^{\rm 2s}_x+\,\mathrm{c}z\overline{\mathcal{E}}{}^{\rm 2c}_x)\rangle\\
&= -\tfrac{1}{2}\langle B^{ss}(\,\mathrm{c}z\overline{\mathcal{E}}{}^{\rm 1s}_y-\,\mathrm{s}z\overline{\mathcal{E}}{}^{\rm 1c}_y)-B^{cs}(\,\mathrm{s}z\overline{\mathcal{E}}{}^{\rm 2s}_y+\,\mathrm{c}z\overline{\mathcal{E}}{}^{\rm 2c}_y)\rangle\\
\tilde\beta_\parallel &= \langle B^{sc}(\,\mathrm{s}z\overline{\mathcal{E}}{}^{\rm 1s}_z+\,\mathrm{c}z\overline{\mathcal{E}}{}^{\rm 1c}_z)\rangle \qquad (21)\\
\tilde\delta &= \tfrac{1}{2}\langle B^{ss}(\,\mathrm{c}z\overline{\mathcal{E}}{}^{\rm 1s}_x-\,\mathrm{s}z\overline{\mathcal{E}}{}^{\rm 1c}_x)-B^{cs}(\,\mathrm{s}z\overline{\mathcal{E}}{}^{\rm 2s}_x+\,\mathrm{c}z\overline{\mathcal{E}}{}^{\rm 2c}_x)\rangle\\
&= \tfrac{1}{2}\langle B^{ss}(\,\mathrm{c}z\overline{\mathcal{E}}{}^{\rm 1s}_x-\,\mathrm{s}z\overline{\mathcal{E}}{}^{\rm 1c}_x)-B^{sc}(\,\mathrm{s}z\overline{\mathcal{E}}{}^{\rm 2s}_y+\,\mathrm{c}z\overline{\mathcal{E}}{}^{\rm 2c}_y)\rangle\\
\tilde\kappa_\perp &= -\langle B^{ss}(\,\mathrm{c}z\overline{\mathcal{E}}{}^{\rm 1s}_x-\,\mathrm{s}z\overline{\mathcal{E}}{}^{\rm 1c}_x)+B^{cs}(\,\mathrm{s}z\overline{\mathcal{E}}{}^{\rm 2s}_x+\,\mathrm{c}z\overline{\mathcal{E}}{}^{\rm 2c}_x)\rangle\\
&= -\langle B^{ss}(\,\mathrm{c}z\overline{\mathcal{E}}{}^{\rm 1s}_x-\,\mathrm{s}z\overline{\mathcal{E}}{}^{\rm 1c}_x)+B^{sc}(\,\mathrm{s}z\overline{\mathcal{E}}{}^{\rm 2s}_y+\,\mathrm{c}z\overline{\mathcal{E}}{}^{\rm 2c}_y)\rangle\\
\tilde\kappa_\parallel &= -\langle B^{ss}(\,\mathrm{c}z\overline{\mathcal{E}}{}^{\rm 2s}_z-\,\mathrm{s}z\overline{\mathcal{E}}{}^{\rm 2c}_z)\rangle\\
\tilde\mu &= -\langle B^{ss}(\,\mathrm{c}z\overline{\mathcal{E}}{}^{\rm 1s}_y-\,\mathrm{s}z\overline{\mathcal{E}}{}^{\rm 1c}_y)-B^{sc}(\,\mathrm{s}z\overline{\mathcal{E}}{}^{\rm 2s}_x+\,\mathrm{c}z\overline{\mathcal{E}}{}^{\rm 2c}_x)\rangle\\
&= -\langle B^{ss}(\,\mathrm{c}z\overline{\mathcal{E}}{}^{\rm 1s}_y-\,\mathrm{s}z\overline{\mathcal{E}}{}^{\rm 1c}_y)+B^{cs}(\,\mathrm{s}z\overline{\mathcal{E}}{}^{\rm 2s}_y+\,\mathrm{c}z\overline{\mathcal{E}}{}^{\rm 2c}_y)\rangle\,,
\end{aligned}$$

where

$$\begin{aligned}
b^{ss} &= 4\,\mathrm{s}x\,\mathrm{s}y/B_0\,,\quad B^{ss}=h^{ss}/k_z\\
B^{cs} &= 4\,\mathrm{c}x\,\mathrm{s}y/k_xB_0\,,\quad B^{sc}=4\,\mathrm{s}x\,\mathrm{c}y/k_yB_0. \qquad (22)
\end{aligned}$$

The angle brackets indicate averaging over x and y. Although the relations (21) and (22) contain k_x, k_y and k_z as independent variables, the $\tilde\alpha_\perp$, $\tilde\alpha_\parallel$, ..., $\tilde\mu$ should vary only via $k_\perp=(k_x^2+k_y^2)^{1/2}$ with k_x and k_y, and only via $k_\parallel$ with k_z.

4.2. Test-scalar method

In the passive-scalar case the coefficients γ^C, $\beta^C_\perp$, $\beta^C_\parallel$, and δ^C are determined by the test-scalar method with test scalars $\overline{C}^T$ and the corresponding fluxes $\overline{\boldsymbol{\mathcal{F}}}^T$. For the latter, we have $\overline{\boldsymbol{\mathcal{F}}}^T=\overline{\boldsymbol{u}c^T}$, where c^T obeys

$$\frac{\partial c^T}{\partial t}=-\boldsymbol{\nabla}\cdot\left(\overline{\boldsymbol{U}}c^T+\boldsymbol{u}\overline{C}^T+(\boldsymbol{u}c^T)'-D\boldsymbol{\nabla}c^T\right)\,. \qquad (23)$$

Again $\overline{\boldsymbol{U}}$ and $\boldsymbol{u}$ are taken from the solutions of (16).

We define two test-scalars $\overline{C}^{\rm Ts}$ and $\overline{C}^{\rm Tc}$ by

$$\overline{C}^{\rm s}=C_0\,\mathrm{s}x\,\mathrm{s}y\,\mathrm{s}z\,,\quad \overline{C}^{\rm c}=C_0\,\mathrm{s}x\,\mathrm{s}y\,\mathrm{c}z\,, \qquad (24)$$

where C_0 is a constant and the abbreviations (19) are used. From (14) we then have

$$\begin{aligned}
\overline{\mathcal{F}}{}^{\rm s}_x &= -C_0(\tilde\beta^C_\perp k_x\,\mathrm{c}x\,\mathrm{s}y\,\mathrm{s}z-\tilde\delta^C k_y\,\mathrm{s}x\,\mathrm{c}y\,\mathrm{s}z)\\
\overline{\mathcal{F}}{}^{\rm s}_y &= -C_0(\tilde\beta^C_\perp k_y\,\mathrm{s}x\,\mathrm{c}y\,\mathrm{s}z+\tilde\delta^C k_x\,\mathrm{c}x\,\mathrm{s}y\,\mathrm{s}z) \qquad (25)\\
\overline{\mathcal{F}}{}^{\rm s}_z &= -C_0(\tilde\gamma^C_\perp\,\mathrm{s}x\,\mathrm{s}y\,\mathrm{s}z+\tilde\beta^C_\parallel k_z\,\mathrm{s}x\,\mathrm{s}y\,\mathrm{c}z)
\end{aligned}$$

and analogous relations for $\overline{\mathcal{F}}{}^{\rm c}_x,\ldots,\overline{\mathcal{F}}{}^{\rm c}_z$ with sz and cz replaced by cz and $-sz$, respectively.

Analogously to the magnetic case, we assume that γ^C, $\beta^C_\perp$, $\beta^C_\parallel$, and δ^C are independent of x and y but may depend on z. Analogous to (21) we find here

$$\begin{aligned}
\tilde\gamma^C &= -\langle c^{ss}(\,\mathrm{s}z\overline{\mathcal{F}}{}^{\rm s}_z+\,\mathrm{c}z\overline{\mathcal{F}}{}^{\rm c}_z)\rangle\\
\tilde\beta^C_\perp &= -\langle C^{cs}(\,\mathrm{s}z\overline{\mathcal{F}}{}^{\rm s}_x+\,\mathrm{c}z\overline{\mathcal{F}}{}^{\rm c}_x)\rangle=-\langle C^{sc}(\,\mathrm{s}z\overline{\mathcal{F}}{}^{\rm s}_y+\,\mathrm{c}z\overline{\mathcal{F}}{}^{\rm c}_y)\rangle\\
\tilde\beta^C_\parallel &= -\langle C^{ss}(\,\mathrm{c}z\overline{\mathcal{F}}{}^{\rm s}_z-\,\mathrm{s}z\overline{\mathcal{F}}{}^{\rm c}_z)\rangle \qquad (26)\\
\tilde\delta^C &= \langle C^{sc}(\,\mathrm{s}z\overline{\mathcal{F}}{}^{\rm s}_x+\,\mathrm{c}z\overline{\mathcal{F}}{}^{\rm c}_x)\rangle=-\langle C^{cs}(\,\mathrm{s}z\overline{\mathcal{F}}{}^{\rm s}_y+\,\mathrm{c}z\overline{\mathcal{F}}{}^{\rm c}_y)\rangle\,,
\end{aligned}$$

where c^{ss}, C^{ss}, C^{sc}, and C^{cs} are defined like b^{ss}, B^{ss}, B^{sc}, and B^{cs}, with C_0 at the place of B_0. The angle brackets indicate again averaging over x and y. Note that $\tilde\gamma^C$, $\tilde\beta^C_\perp$, $\tilde\beta^C_\parallel$, and $\tilde\delta^C$ should depend only via $k_\perp=(k_x^2+k_y^2)^{1/2}$ on k_x and k_y, and only via $k_\parallel$ on k_z.

4.3. Validation using the Roberts flow

For a validation of our test-field procedure for the determination of the coefficients occurring in (3) we rely on the Roberts flow. We define it here by

$$\boldsymbol{u}=u_0(-\cos k_0x\,\sin k_0y\,,\,\sin k_0x\,\cos k_0y\,,\,2f\cos k_0x\,\cos k_0y\,), \qquad (27)$$

with some wavenumber k_0 and a factor f which characterizes the ratio of the magnitude of u_z to that of u_x and u_y. We further define mean fields as averages over x and y with an averaging scale which is much larger than the period length $2\pi/k_0$ of the flow pattern. When calculating the mean electromotive force $\overline{\boldsymbol{\mathcal{E}}}$ for this flow, we assume that it is a linear homogeneous function of $\overline{\boldsymbol{B}}$ and its first spatial derivatives and adopt the second-order correlation approximation. Although the Roberts flow is far from being axisymmetric, the result for $\overline{\boldsymbol{\mathcal{E}}}$ can be written in the form (3), where we have

$$\begin{aligned}
\alpha_\perp &= \frac{u_0^2 f}{2\eta k_0}\,,\quad \alpha_\parallel=\gamma=0\\
\beta_\perp &= \frac{u_0^2(1+4f^2)}{16\eta k_0^2}\,,\quad \beta_\parallel=\frac{u_0^2}{8\eta k_0^2}\,,\quad \delta=0 \qquad (28)\\
\kappa_\perp &= \kappa_\parallel=0\,,\quad \mu=-\frac{u_0^2(1-4f^2)}{8\eta k_0^2}\,.
\end{aligned}$$

It agrees with and can be deduced from results reported in Rädler et al. (2002a,b). As for the passive scalar case, an analogous analytical calculation of the mean scalar flow $\overline{\mathcal{F}}$ leads to (12) with

$$\gamma^C=0\,,\quad \beta^C_\perp=\frac{u_0^2}{8Dk_0^2}\,,\quad \beta^C_\parallel=\frac{u_0^2f^2}{2Dk_0^2}\,,\quad \delta^C=0\,. \qquad (29)$$

We may proceed from the local connection of $\overline{\boldsymbol{\mathcal{E}}}$ with $\overline{\boldsymbol{B}}$ and its derivatives considered in (3) to the non-local ones given by (6) or (8). As a consequence of the deviation of the flow from axisymmetry, we can then no longer justify that coefficients like $\alpha_\perp(\boldsymbol{\xi})$ depend only via $\xi_x^2+\xi_y^2$ on ξ_x and ξ_y, and coefficients like $\tilde\alpha_\perp(\boldsymbol{k})$ only via $k_\perp$ on k_x and k_y. This applies analogously to the connection of $\overline{\mathcal{F}}$ with $\overline{C}$ and its derivatives and to coefficients like $\beta_\perp(\boldsymbol{\xi})$ and $\tilde\beta_\perp(\boldsymbol{k})$.

A test-field calculation of the coefficients $\tilde\alpha_\perp$, $\tilde\alpha_\parallel$, ..., $\tilde\mu$, as well as $\tilde\gamma^C$, ..., $\tilde\delta^C$ has been carried out under the conditions of the second-order correlation approximation with $\boldsymbol{u}$ given by (27) and $f=1/\sqrt{2}$. Figure 1 shows the

results obtained for $\tilde{\alpha}_\perp$, $\tilde{\beta}_\perp$, $\tilde{\beta}_\parallel$ and $\tilde{\mu}$, as well as $\tilde{\beta}^C_\perp$ and $\tilde{\beta}^C_\parallel$, as functions of $k_\perp/k_\mathrm{f}$, with $k_\mathrm{f} = \sqrt{2}k_0$, for two fixed ratios $k_\parallel/k_\perp$. In the limit $k_\perp/k_\mathrm{f} \ll 1$ these coefficients take just the values of $\alpha_\perp$, $\beta_\perp$, $\beta_\parallel$, μ, $\beta^C_\perp$ and $\beta^C_\parallel$ given in (28) and (29). For larger values of $k_\perp/k_\mathrm{f}$, as to be expected, the $\tilde{\alpha}_\perp$, $\tilde{\beta}_\perp$, $\tilde{\beta}_\parallel$, $\tilde{\mu}$, $\tilde{\beta}^C_\perp$ and $\tilde{\beta}^C_\parallel$ depend also on the ratio of k_x and k_y.

4.4. Dimensionless parameters and related issues

Within the framework of this paper, the coefficients $\alpha_\perp$, $\alpha_\parallel$, ..., μ as well as $\tilde{\alpha}_\perp$, $\tilde{\alpha}_\parallel$, ..., $\tilde{\mu}$, and likewise γ^C, $\beta^C_\perp$, ..., δ^C and $\tilde{\gamma}^C$, $\tilde{\beta}^C_\perp$, ..., $\tilde{\delta}^C$, have to be considered as functions of several dimensionless parameters. In the magnetic case these are the magnetic Reynolds number $R_\mathrm{m} = u_\mathrm{rms}/\eta k_\mathrm{f}$ and the magnetic Prandtl number $P_\mathrm{m} = \nu/\eta$, in the passive scalar case the Péclet number $\mathrm{Pe} = u_\mathrm{rms}/Dk_\mathrm{f}$ and the Schmidt number $\mathrm{Sc} = \nu/D$, further the Mach number $\mathrm{Ma} = u_\mathrm{rms}/c_\mathrm{s}$, the gravity parameter $\mathrm{Gr} = g/c_\mathrm{s}^2 k_\mathrm{f}$, the Coriolis number $\mathrm{Co} = 2\Omega/u_\mathrm{rms}k_\mathrm{f}$, as well as the scale separation ratio k_f/k_1.

Throughout the rest of the paper we give the coefficients $\alpha_\perp$, $\alpha_\parallel$, γ, and γ^C as well as $\tilde{\alpha}_\perp$, $\tilde{\alpha}_\parallel$, $\tilde{\gamma}$, and $\tilde{\gamma}^C$ in units of $u_\mathrm{rms}/3$, the remaining coefficients $\beta_\perp$, ..., δ^C and $\tilde{\beta}_\perp$, ..., $\tilde{\delta}^C$ in units of $u_\mathrm{rms}/3k_\mathrm{f}$. The numerical calculations deliver these coefficients as functions of z and t. To avoid boundary effects, we average these results over $-2 \le k_1 z \le 1$ (see Figure 3 below). The resulting time series are averaged over a range where the results are statistically stationary. Error bars are defined by comparing the maximum departure of an average over any one third of the time series with the full time average.

In the case of isotropic turbulence it has been observed that many of the turbulent transport coefficients enter an asymptotic regime as soon as R_m exceeds unity (Sur et al., 2008). While this should be checked in every new case again (see below), it is important to realize that, according to several earlier results (see also Brandenburg et al., 2009), only values of R_m below unity are characteristic of the diffusively dominated regime, while for R_m exceeding unity the transport coefficients turn out to be nearly independent of the value of R_m.

We are primarily interested in the limit $k_\perp, k_\parallel \to 0$, in which the $\tilde{\alpha}_\perp$, $\tilde{\alpha}_\parallel$, ... $\tilde{\delta}^C$ turn into the $\alpha_\perp$, $\alpha_\parallel$ ... δ^C. To avoid vanishing test fields or test scalars in Equations (18) and (24), we choose $k_x = k_y = k_z = k_1$, unless specified otherwise.

5. Results

5.1. Homogeneous rotating turbulence

Let us first consider homogeneous turbulence in a rotating system, that is, under the influence of the Coriolis force. The angular velocity $\boldsymbol{\Omega}$ responsible for this force defines the preferred direction of the turbulence, $\hat{\boldsymbol{e}} = \boldsymbol{\Omega}/|\boldsymbol{\Omega}|$. In this case we expect only contributions to the mean electromotive force $\overline{\boldsymbol{\mathcal{E}}}$ from a spatially varying mean magnetic field $\overline{\boldsymbol{B}}$, and contributions to the passive scalar flux $\overline{\boldsymbol{\mathcal{F}}}$ from a spatially varying mean passive scalar $\overline{C}$. That is, in (3) we have only the terms with $\beta_\perp$, $\beta_\parallel$, δ, $\kappa_\perp$, $\kappa_\parallel$, and μ,

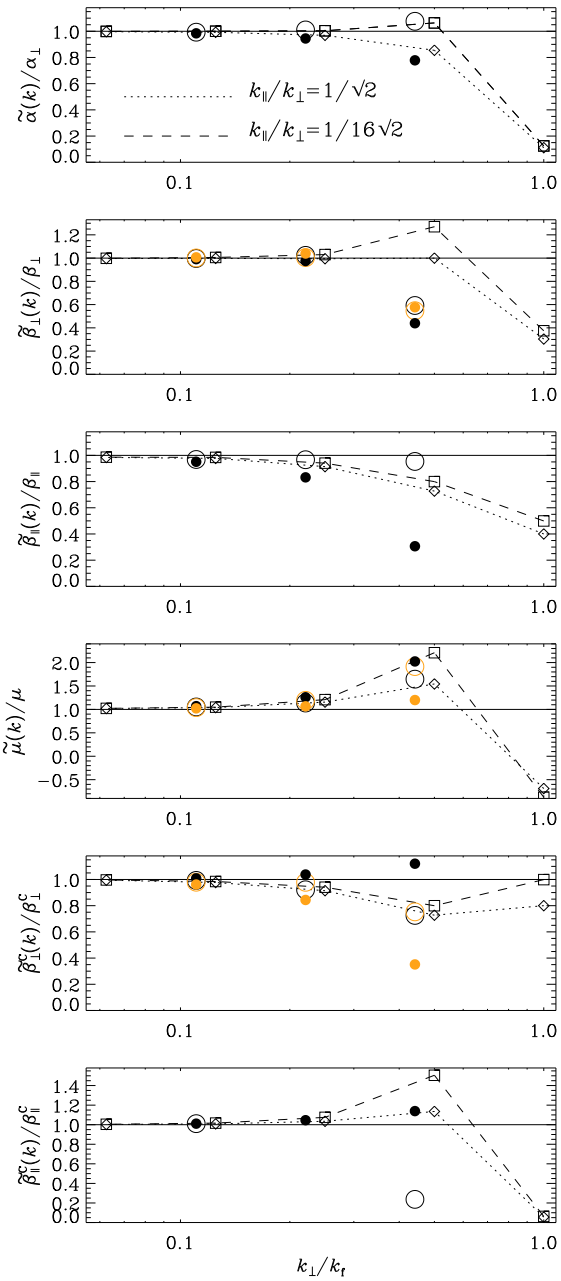

Fig. 1. The coefficients $\tilde{\alpha}_\perp$, $\tilde{\beta}_\perp$, $\tilde{\beta}_\parallel$, and $\tilde{\mu}$, as well as $\tilde{\beta}^C_\perp$ and $\tilde{\beta}^C_\parallel$ for the Roberts flow, calculated in the second-order correlation approximation, as functions of $k_\perp/k_\mathrm{f}$, where $k_\mathrm{f} = \sqrt{2}k_0$ is the effective wavenumber of the flow. Results obtained with $k_x = k_y$ and $k_\parallel/k_\perp = 1/\sqrt{2} \approx 0.7$ or $k_\parallel/k_\perp = 1/16\sqrt{2} \approx 0.004$ are represented by open squares and dotted lines or by open diamonds and dashed lines, respectively. Results with $k_x/k_y = 0.75$ [$\boldsymbol{k}_\perp = (3,4,0)k_1$] or $k_x/k_y = 5$ [$\boldsymbol{k}_\perp = (5,1,0)k_1$] and $k_\parallel/k_\perp = 0.2$ are indicated by open or filled circles, respectively. Orange and grey symbols correspond to the first and second expressions for $\tilde{\beta}_\perp$ and $\tilde{\mu}$ in (21) or for $\tilde{\beta}^C_\parallel$ in (26).

and in (12) only those with $\beta^C_\perp$, $\beta^C_\parallel$, and δ^C. The terms with $\beta_\perp$ and $\beta_\parallel$, as well as those with $\beta^C_\perp$ and $\beta^C_\parallel$, characterize anisotropic mean-field diffusivities, and that with δ

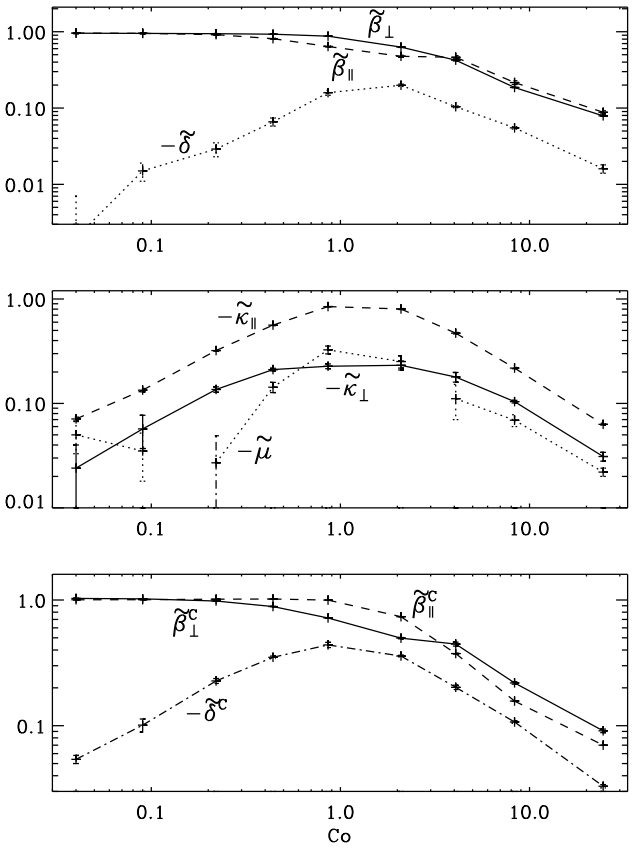

Fig. 2. Co dependence of transport coefficients in a model with rotation and density stratification, $R_\mathrm{m} \approx 9$, $P_\mathrm{m} = \mathrm{Sc} = 1$, $\mathrm{Gr} = 0$, $k_\mathrm{f}/k_1 = 5$.

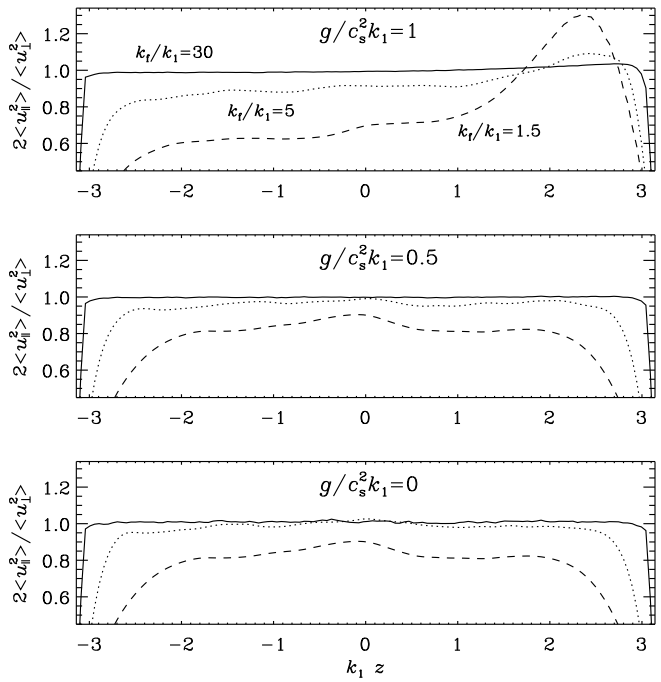

Fig. 3. Anisotropy $2\overline{u_\parallel^2}/\overline{u_\perp^2}$ of the flow for different stratifications $g/c_\mathrm{s}^2 k_1$.

corresponds to the "$\boldsymbol{\Omega} \times \overline{\boldsymbol{J}}$ effect" (Rädler, 1969a,b, 1976; Krause & Rädler, 1971, 1980), while the δ^C term vanishes underneath the divergence and is therefore without interest.

Figure 2 shows the dependence of the aforementioned coefficients on Co for $R_\mathrm{m} \approx \mathrm{Pe} \approx 9$ and $k_\mathrm{f}/k_1 = 5$. In the limit of slow rotation we have $\beta_\perp \approx \beta_\parallel \approx \beta_\perp^C \approx \beta_\parallel^C$. The other four coefficients vary linearly with Co as long as Co is small. Specifically, we find $\tilde{\delta} \approx -0.1\,\mathrm{Co}$, $\tilde{\delta}^C \approx -\mathrm{Co}$, as well as $\tilde{\kappa}_\perp \approx -0.3\,\mathrm{Co}$ and $\tilde{\kappa}_\parallel \approx -\mathrm{Co}$. These coefficients reach maxima at $\mathrm{Co} \approx 1$. For rapid rotation, $|\mathrm{Co}| \gg 1$, all coefficients approach zero like $1/\mathrm{Co}$. In particular, we have $\beta_\perp \approx 1.2/\mathrm{Co}$ and the same for $\beta_\parallel$, $\beta_\perp^C$, and $\beta_\parallel^C$, further $\tilde{\kappa}_\perp \approx -0.5/\mathrm{Co}$, $\tilde{\kappa}_\parallel \approx -1.2/\mathrm{Co}$, $\tilde{\delta} \approx -0.3/\mathrm{Co}$, and $\tilde{\delta}^C \approx -0.6/\mathrm{Co}$. Furthermore, we find that, within error bars, $\alpha_\perp$, $\alpha_\parallel$, γ, and γ^C are indeed zero.

5.2. Stratified turbulence

Owing to the presence of boundary conditions at the top and bottom of our domain and the lack of scale separation for our default choice of $k_\mathrm{f}/k_1 = 5$, the turbulence is in all cases anisotropic, even if gravity is negligible. The ratio of the vertical and horizontal velocity components, $2\overline{u_\parallel^2}/\overline{u_\perp^2}$, is no longer, as in the isotropic case, equal to unity. For moderate stratification ($g/c_\mathrm{s}^2 k_1 \approx 1$), not too large $|z|$, and $k_\mathrm{f}/k_1 = 5$, it takes a value of about 0.9. It decreases when the ratio k_f/k_1 is decreased; see Table 1. Figure 3 shows the z dependence of $2\overline{u_\parallel^2}/\overline{u_\perp^2}$. For strong stratification and a high degree of scale separation, e.g. $k_\mathrm{f}/k_1 = 30$, the mentioned ratio comes close to unity.

5.3. Stratified nonrotating turbulence

For axisymmetric turbulence in a nonrotating system showing any kind of stratification in the representation (3) of $\overline{\boldsymbol{\mathcal{E}}}$ only the four coefficients γ, $\beta_\perp$, $\beta_\parallel$, and μ can be non-zero. Likewise, in the representation (12) of $\overline{\boldsymbol{\mathcal{F}}}$ only the three coefficients γ^C, $\beta_\perp^C$, and $\beta_\parallel^C$ can be non-zero. Figure 4 shows their dependence on Gr. It appears that γ is always close to zero, while γ^C shows a linear increase for not too strong gravity. At the same time, $\beta_\perp$, $\beta_\parallel$, $\beta_\perp^C$, and $\beta_\parallel^C$ remain approximately constant. We find that μ is negative and mildly increasing with increasing stratification, but the error bars are large.

Table 1. Dependence of the density contrast and the degree of anisotropy on the density stratification for turbulence and 3 different values of k_f/k_1. The values of $2\overline{u_\parallel^2}/\overline{u_\perp^2}$ have been obtained as averages over the range $-2 \le k_1 z \le 1$.

$g/c_\mathrm{s}^2 k_1$	$\rho_\mathrm{bot}/\rho_\mathrm{top}$	Gr	$2\overline{u_\parallel^2}/\overline{u_\perp^2}$		
			$k_\mathrm{f} = 1.5k_1$	$k_\mathrm{f} = 5k_1$	$k_\mathrm{f} = 30k_1$
0	0	0	0.84	0.99	1.00
0.5	23	0.1	0.84	0.97	1.00
1	540	0.2	0.66	0.90	0.99

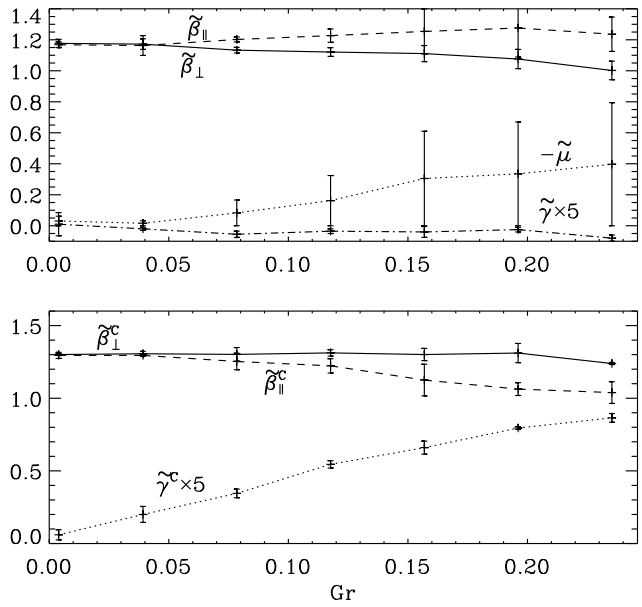

Fig. 4. Gr dependence of the transport coefficients in a model with density stratification, $R_{\rm m} \approx 22$, $P_{\rm m} = {\rm Sc} = 1$, ${\rm Co} = 0$, $k_{\rm f}/k_1 = 5$.

5.4. Stratified rotating turbulence

For turbulence under the influence of gravity and rotation, all nine coefficients $\alpha_\perp$, ..., μ are in general non-zero, as well as all four coefficients γ^C, ..., δ^C. If both gravity and rotation are so small that $\overline{\boldsymbol{\mathcal{E}}}$ is linear in g and Ω, more precisely $\overline{\boldsymbol{\mathcal{E}}}$ contains $g^m\Omega^n$, where n and m mean integers, only with $n+m \leq 1$, $\alpha_\perp$ and $\alpha_\parallel$ vanish but γ, $\beta_\perp$, δ and $\kappa_\perp$ may well be unequal to zero. If $n+m \leq 2$, all nine coefficients may indeed be non-zero.

The result is shown in Figure 5. The error bars are now bigger than either with just rotation or just stratification. For ${\rm Co} \to 0$, all parameters are finite, because gravity is still finite. As Co is increased, $\beta_\perp$ and $\beta_\parallel$, as well as $\beta_\perp^C$ and $\beta_\parallel^C$ show a weak decline. On the other hand $|\alpha_\perp|$ and $|\alpha_\parallel|$ increase with Co for ${\rm Co} < 1$, but most other quantities still show a mild increase until they all decrease again when ${\rm Co} > 1$. Both $\alpha_\perp$ and $\alpha_\parallel$ are negative, which is expected for $\boldsymbol{g}$ and $\boldsymbol{\Omega}$ being antiparallel to each other. Interestingly, μ is finite for small values of Co, in agreement with the result when there is only stratification (Figure 4), but with a modest amount of rotation, μ is suppressed and grows only when Co has reached values around unity.

5.5. Wavenumber dependence

Although we are primarily interested in the limit $k_\perp \to 0$ and $k_\parallel \to 0$, the values of all coefficients are of interest for k close to $k_{\rm f}$, especially if those numbers are not small. Most quantities decrease proportional to k^{-2} and can be fitted to a Lorentzian profile, as has been found in earlier calculation using the test-field method; see Brandenburg et al. (2008a), who considered the dependence on $k_\parallel$. Even earlier work that was not based on the test-field method showed a declining trend (Miesch et al., 2000; Brandenburg & Sokoloff, 2002). Nevertheless, as is shown in Figure 6, there are also some coefficients that first increase with $k_\parallel$, have a maximum near $k_{\rm f}$, and only then decrease with growing $k_\parallel$. Examples for such a behavior are $\tilde{\alpha}_\parallel$, $\tilde{\delta}$, and $\tilde{\kappa}_\perp$, while $\tilde{\kappa}_\parallel$ peaks slightly below $0.5k_{\rm f}$. The dependence on $k_\perp$ is shown in Figure 7. Note that our test fields vanish for $k_\perp = 0$, so no values are shown in this case. Note also that $-\tilde{\alpha}_\parallel$, $-\tilde{\delta}$, $-\tilde{\kappa}_\parallel$, and $-\tilde{\beta}_\perp$, which all have maxima for $k_\parallel/k_{\rm f} \approx 1$, show a clear monotonic decline with $k_\perp$. Only $-\tilde{\kappa}_\perp$ has a maximum for intermediate values of both $k_\parallel/k_{\rm f}$ and $k_\perp/k_{\rm f}$.

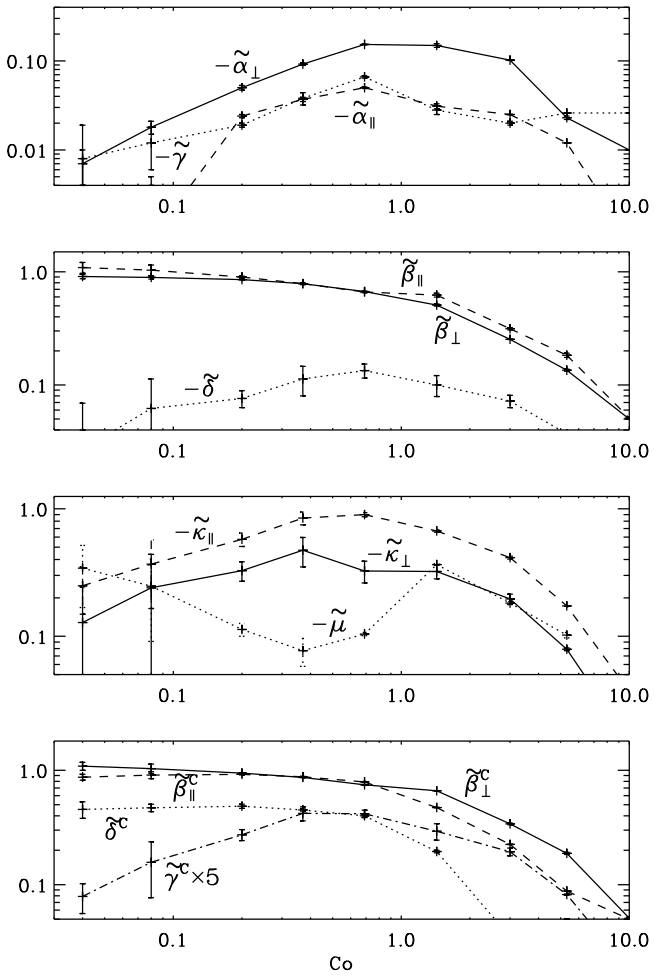

Fig. 5. Co dependence of transport coefficients in a model with rotation and density stratification, $R_{\rm m} \approx 10$, $P_{\rm m} = {\rm Sc} = 1$, ${\rm Gr} \approx 0.16$, $k_{\rm f}/k_1 = 5$.

Most of the results presented in Figure 7 have been calculated with $k_x = k_y$, a few single ones for $\tilde{\alpha}_\perp$, $\tilde{\beta}_\perp$, $\tilde{\kappa}_\perp$ and $\tilde{\beta}_\perp^C$ also with $k_x/k_y = 0.75$ and $k_x/k_y = 0.2$. While the results for $\tilde{\beta}_\perp$ and $\tilde{\beta}_\perp^C$ agree well for all these values of k_x/k_y, there are significant discrepancies with $\tilde{\alpha}_\perp$ and $\tilde{\kappa}_\perp$.

5.6. Dependencies on $R_{\rm m}$ and Pe

Let us finally consider the dependence of all 13 transport coefficients on $R_{\rm m}$ or Pe for a case where they are all expected to be finite. Therefore we choose again the case ${\rm Gr} = 0.16$ and ${\rm Co} = 1$, which was also considered in Figures 5–7. We keep $P_{\rm m} = {\rm Sc} = 1$.

The result are shown in Figure 8. As expected, all quantities increase approximately linearly for $R_{\rm m} \leq 1$ and seem

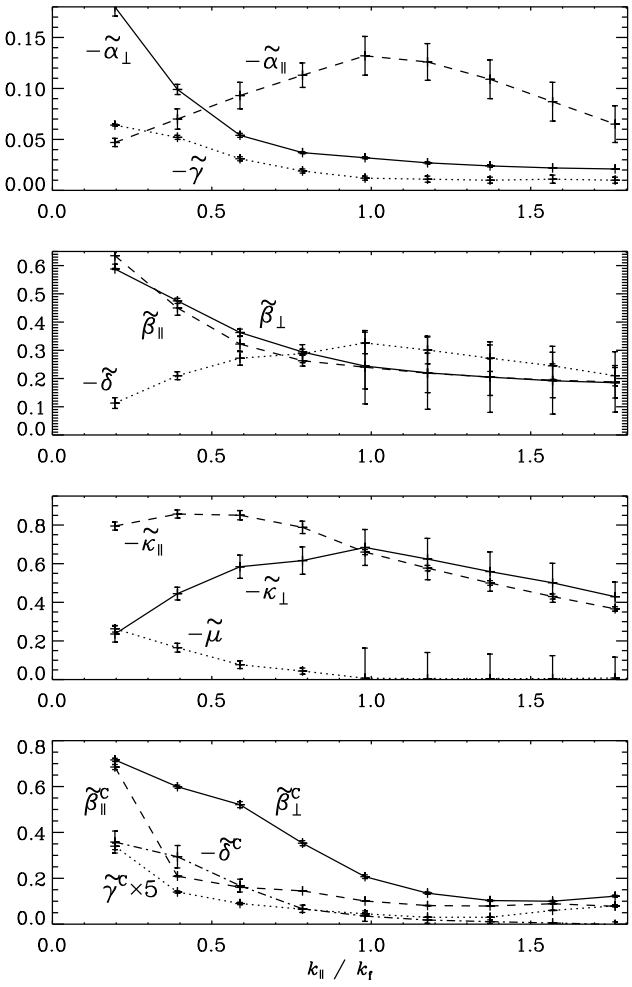

Fig. 6. $k_\parallel$ dependence of transport coefficients in a model with rotation and density stratification, $R_{\rm m}=12$, ${\rm Co}=1.0$, $k_{\rm f}/k_1=5$.

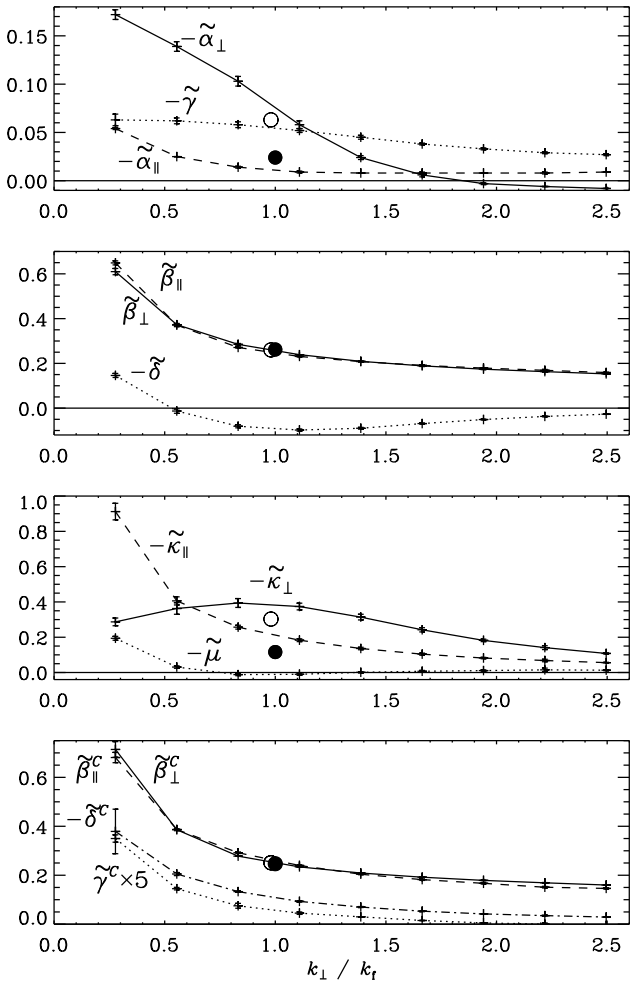

Fig. 7. Same as Figure 6, but $k_\perp$ dependence. The filled and open symbols denote results for $\alpha_\perp$, $\beta_\perp$, $\kappa_\perp$, and $\beta^C_\perp$ obtained with $k_x/k_y=0.75$ [$\boldsymbol{k}_\perp=(3,4,0)k_1$] and $k_x/k_y=0.2$ [$\boldsymbol{k}_\perp=(1,5,0)k_1$], respectively.

to level off to constant values for larger values of $R_{\rm m}$, although the uncertainty tends to increase significantly.

6. Conclusions

In this paper we have dealt with the mean electromotive force and the mean passive scalar flux in axisymmetric turbulence and calculated, at relatively little computational cost, the transport coefficients which define these quantities. Unlike most of the earlier work, we have no longer assumed that mean fields are defined as planar averages but admit a dependence on all three space coordinates.

We may conclude from general symmetry considerations that the mean electromotive force $\overline{\boldsymbol{\mathcal{E}}}$ has three contributions defined by the mean magnetic field $\overline{\boldsymbol{B}}$, three defined by the mean current density $\overline{\boldsymbol{J}}$, and three defined by the vector $\overline{\boldsymbol{K}}$, the projection of the symmetric part of the gradient tensor $\boldsymbol{\nabla}\overline{\boldsymbol{B}}$ of the magnetic field on the preferred direction. In many representations of $\overline{\boldsymbol{\mathcal{E}}}$ the last three contributions have been ignored. Our results underline that this simplification is in general not justified. The corresponding coefficients $\kappa_\perp$, $\kappa_\parallel$ and μ are in general not small compared with $\beta_\perp$, $\beta_\parallel$ and δ.

It has been known since long that a stratification of the turbulence intensity, that is, a gradient of $\overline{\boldsymbol{u}^2}$, causes a pumping of magnetic flux (Rädler, 1969a). It remained however uncertain whether the same effect occurs if a preferred direction is given by a gradient of the mean mass density $\overline{\varrho}$ while the turbulence intensity is spatially constant. In our calculations, which correspond to this assumption, the value of γ is not clearly different from zero. This suggests that a gradient of the mass density alone is not sufficient for pumping, what is also in agreement with results of Brandenburg et al. (2011). This is even more remarkable as the corresponding coefficient γ^C which describes the transport of a mean passive scalar is noticeably different from zero. Pumping down the density gradient is indeed expected (Elperin et al., 1995). An explanation of these results would be very desirable.

In homogeneous rotating turbulence, apart from an anisotropy of the mean-field conductivity, the $\boldsymbol{\Omega}\times\overline{\boldsymbol{J}}$ effect occurs (Rädler, 1969b). In the passive scalar case again an anisotropy of the mean diffusivity is possible. Even if the flux proportional to $\boldsymbol{\Omega}\times\boldsymbol{\nabla}\overline{C}$ is non-zero, it cannot influence $\overline{C}$.

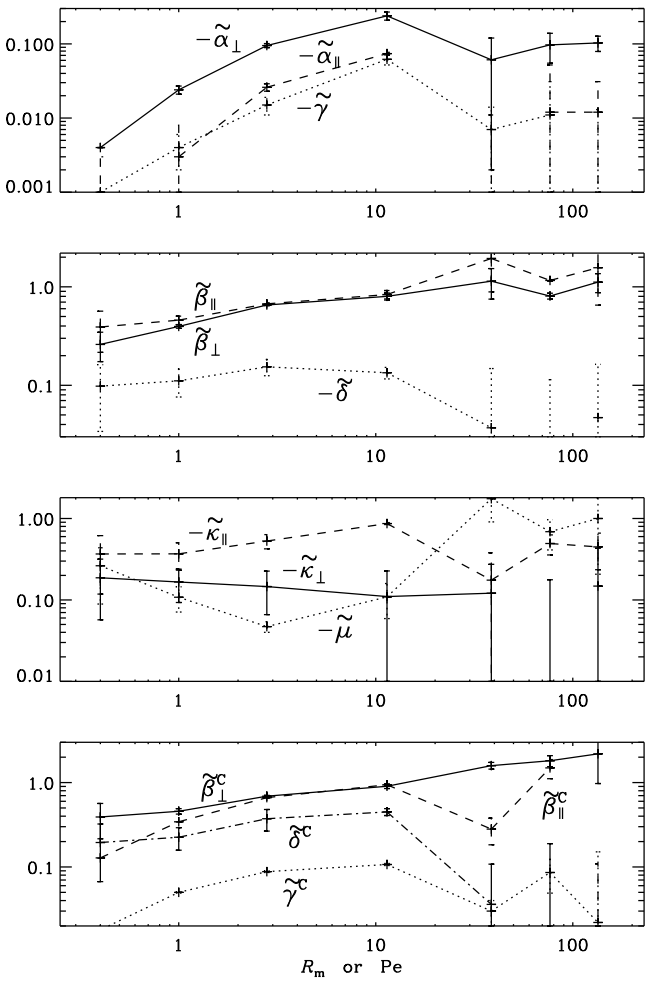

Fig. 8. Dependencies of the transport coefficients on $R_{\rm m}$ or Pe in a model with rotation and density stratification, Co = 1.0, Gr = 0.16, $k_{\rm f}/k_1 = 5$.

Let us turn to the induction effects described by $\overline{\boldsymbol{K}}$. If the preferred direction is given by a polar vector, the corresponding contribution to the mean electromotive force can only be proportional to $\hat{\boldsymbol{e}} \times \overline{\boldsymbol{K}}$. We found such a contribution in the case of the Roberts flow and also, for turbulence subject the Coriolis force, in the results presented in Figures 2–7

Contributions to the mean electromotive force described here by $\overline{\boldsymbol{K}}$ occur also in earlier calculations, e.g. Kitchatinov et al. (1994) or Rüdiger & Brandenburg (1995). As a consequence of other notations, however, this is not always obvious. For example, Rüdiger & Brandenburg (1995) consider a mean electromotive force of the form

$$\overline{\boldsymbol{\mathcal{E}}} = -\eta_\parallel \overline{\boldsymbol{J}} + (\eta_\parallel - \eta_{\rm T})(\hat{\boldsymbol{z}}\overline{J}_z - \hat{\boldsymbol{z}} \times \boldsymbol{\nabla}\overline{B}_z) \tag{30}$$

with two coefficients $\eta_\parallel$ and $\eta_{\rm T}$ (equation (18) of their paper with $\mu_0\overline{\boldsymbol{J}}$, in the sense of the definition introduced here, replaced by $\overline{\boldsymbol{J}}$; $\hat{\boldsymbol{z}}$ is our $\hat{\boldsymbol{e}}$). It is equivalent to our representations (3) or (4) of $\overline{\boldsymbol{\mathcal{E}}}$ if we put there $\beta_\perp = \frac{1}{2}(\eta_\parallel + \eta_{\rm T})$, $\beta_\parallel = \eta_{\rm T}$, $\mu = \eta_\parallel - \eta_{\rm T}$ and all other coefficients equal to zero.

If both rotation and density stratification are present, there is also the α effect, which is necessarily anisotropic. For strong rotation $\alpha_\parallel$ is only half as big as $\alpha_\perp$. By contrast, magnetic diffusivity is, within error bars, found to be isotropic, that is, $\beta_\perp \approx \beta_\parallel$. In view of earlier results showing that turbulent diffusion should occur preferentially along the rotation axis (Kitchatinov et al., 1994; Rüdiger & Brandenburg, 1995), this result is surprising. In the presence of rotation and density stratification all three contributions to the mean electromotive fore described by $\overline{\boldsymbol{K}}$ are in general non-zero. Here, $|\kappa_\perp|$ is smaller than $|\kappa_\parallel|$.

The present work is applicable to investigations of stellar convection either with or without rotation, and it would provide a more comprehensive description of turbulent transport properties than what has been available so far (Käpylä et al., 2009). The method utilized in this paper can be extended to a large class of phenomena in which turbulence with just one preferred direction plays an important role. Examples for that include turbulence under the influence of a strong magnetic field and/or an externally applied electric field leading to a current permeating the system. Turbulence generated by the Bell (2004) instability is an example (Rogachevskii et al., 2011). Other examples include all types of inhomogeneous turbulence with only one preferred direction. In addition to density stratification, there can be a systematic variation of the turbulence intensity in one direction. A further example is entropy inhomogeneity combined with gravity giving rise to Brunt-Väisälä oscillations. Pumping effects also exist in homogeneous flows if the turbulence is helical (Mitra et al., 2009). By contrast, shear problems or other types of problem with two or more preferred directions that are inclined to each other (e.g., turbulence in a local domain of a rotating stratified shell at latitudes different from the two poles) are not amenable to such a study. Of course, although we refer here to axisymmetric turbulence, problems in axisymmetric cylindrical geometry are also not amenable to this method, because the turbulence must be homogeneous in one plane.

Acknowledgements. A.B. and K.-H.R. are grateful for the opportunity to work on this paper while participating in the program "The Nature of Turbulence" at the Kavli Institute for Theoretical Physics in Santa Barbara, CA. This work was supported in part by the European Research Council under the AstroDyn Research Project No. 227952 and the National Science Foundation under Grant No. NSF PHY05-51164. We acknowledge the allocation of computing resources provided by the Swedish National Allocations Committee at the Center for Parallel Computers at the Royal Institute of Technology in Stockholm and the National Supercomputer Centers in Linköping.

Appendix A: Derivation of relation (3)

We start from the aforementioned assumption according to which $\overline{\boldsymbol{\mathcal{E}}}$ is linear and homogeneous in $\overline{\boldsymbol{B}}$ and its first spatial derivatives,

$$\overline{\mathcal{E}}_i = a_{ij}\overline{B}_j + b_{ijk}(\boldsymbol{\nabla}\overline{\boldsymbol{B}})_{jk}\,. \tag{A.1}$$

Here a_{ij} and b_{ijk} are tensors determined by the fluid flow. The gradient tensor $(\boldsymbol{\nabla}\overline{\boldsymbol{B}})_{jk}$ can be split into a antisymmetric part, which can be expressed by $\overline{\boldsymbol{J}}$, and a symmetric part $(\boldsymbol{\nabla}\overline{\boldsymbol{B}})^{\rm S}_{jk}$. Therefore we may also write

$$\overline{\mathcal{E}}_i = a_{ij}\overline{B}_j - b_{ij}\overline{J}_j - c_{ijk}(\boldsymbol{\nabla}\overline{\boldsymbol{B}})^{\rm S}_{jk} \tag{A.2}$$

with new tensors b_{ij} and c_{ijk} with $c_{ijk} = c_{ikj}$. From the further assumption that the flow constitutes an axisymmetric

turbulence we may conclude that a_{ij}, b_{ij} and c_{ijjk} are axisymmetric tensors. Defining the preferred direction by the unit vector $\hat{\boldsymbol{e}}$ we then have

$$\begin{aligned} a_{ij} &= a_1\delta_{ij} + a_2\epsilon_{ijl}\hat{e}_l + a_3\hat{e}_i\hat{e}_j\,, \\ b_{ij} &= b_1\delta_{ij} + b_2\epsilon_{ijl}\hat{e}_l + b_3\hat{e}_i\hat{e}_j\,, \\ c_{ijk} &= c_1\delta_{jk}\hat{e}_i + c_2(\delta_{ij}\hat{e}_k + \delta_{ik}\hat{e}_j) \\ &\quad + c_3(\epsilon_{ijl}\hat{e}_l\hat{e}_k + \epsilon_{ikl}\hat{e}_l\hat{e}_j) + c_4\hat{e}_i\hat{e}_j\hat{e}_k\,, \end{aligned} \tag{A.3}$$

with coefficients a_1, a_2, …, c_4 determined by the fluid flow. Taking (A.2) and (A.3) together and considering that

$$\begin{aligned} (\delta_{ij}\hat{e}_k + \delta_{ik}\hat{e}_j)(\boldsymbol{\nabla}\overline{\boldsymbol{B}})^{\rm S}_{jk} &= 2\overline{K}_i\,, \\ (\epsilon_{ijl}\hat{e}_l\hat{e}_k + \epsilon_{ikl}\hat{e}_l\hat{e}_j)(\boldsymbol{\nabla}\overline{\boldsymbol{B}})^{\rm S}_{jk} &= -2(\hat{\boldsymbol{e}}\times\overline{\boldsymbol{K}})_i\,, \\ \hat{e}_i\hat{e}_j\hat{e}_k(\boldsymbol{\nabla}\overline{\boldsymbol{B}})^{\rm S}_{jk} &= (\hat{\boldsymbol{e}}\cdot\overline{\boldsymbol{K}})\hat{e}_i\,, \end{aligned} \tag{A.4}$$

we find

$$\begin{aligned} \overline{\boldsymbol{\mathcal{E}}} &= a_1\overline{\boldsymbol{B}} - a_2\hat{\boldsymbol{e}}\times\overline{\boldsymbol{B}} - a_3(\hat{\boldsymbol{e}}\cdot\overline{\boldsymbol{B}})\hat{\boldsymbol{e}} \\ &\quad + b_1\overline{\boldsymbol{J}} - b_2\hat{\boldsymbol{e}}\times\overline{\boldsymbol{J}} - b_3(\hat{\boldsymbol{e}}\cdot\overline{\boldsymbol{J}})\hat{\boldsymbol{e}} \\ &\quad + 2c_2\overline{\boldsymbol{K}} - 2c_3\hat{\boldsymbol{e}}\times\overline{\boldsymbol{K}} + c_4(\hat{\boldsymbol{e}}\cdot\overline{\boldsymbol{K}})\hat{\boldsymbol{e}}\,. \end{aligned} \tag{A.5}$$

Since $(\boldsymbol{\nabla}\overline{\boldsymbol{B}})_{ii} = 0$ there is no contribution with c_1. With a proper renaming of the coefficients (A.5) turns into (3).

References

Bell, A. R. 2004, MNRAS, 353, 550
Brandenburg, A., & Sokoloff, D. 2002, Geophys. Astrophys. Fluid Dyn., 96, 319
Brandenburg, A., Rädler, K.-H., & Schrinner, M. 2008a, A&A, 482, 739
Brandenburg, A., Rädler, K.-H., Rheinhardt, M., & Käpylä, P. J. 2008b, ApJ, 676, 740
Brandenburg, A., Svedin, A., & Vasil, G. M. 2009, MNRAS, 395, 1599
Brandenburg, A., Kemel, K., Kleeorin, N., & Rogachevskii, I. 2011, ApJ, submitted
Chatterjee, P., Mitra, D., Rheinhardt, & M. Brandenburg, A. 2011, A&A, to be published arXiv:1011.1218
Elperin, T., Kleeorin, N., Rogachevskii, I. 1995, Phys. Rev. Lett., 52, 2617
Elperin, T., Kleeorin, N., Rogachevskii, I. 1996, Phys. Rev. Lett., 76, 224
Haugen, N.E.L., Brandenburg, A., Dobler, W. 2004, Phys. Rev. E, 70, 016308
Käpylä, P. J., Korpi, M. J., & Brandenburg, A. 2009, A&A, 500, 633
Kitchatinov, L. L., Rüdiger, G., Pipin, V. V. & Rüdiger, G. 1994, Astron. Nachr., 315, 157
Krause, F., & Rädler, K.-H., 1971, In R. Rompe and M. Steenbeck, *Ergebnisse der Plasmaphysik und der Gaselektronik* Band 2, Akademie-Verlag Berlin, pp. 6–154
Krause, F., & Rädler, K.-H., 1980, *Mean-Field Magnetohydrodynamics and Dynamo Theory*, Akademie-Verlag Berlin and Pergamon Press Cambridge
Madarassy, E. J. M., & Brandenburg, A. 2010, Phys. Rev. E, 82, 016304
Miesch, M. S., Brandenburg, A., & Zweibel, E. G. 2000, Phys. Rev., E61, 457
Mitra, D., Käpylä, P. J., Tavakol, R., & Brandenburg, A. 2009, A&A, 495, 1
Prandtl, L. 1925, Zeitschr. Angewandt. Math. Mech., 5, 136
Rädler, K.-H. 1966, Thesis Univ. Jena
Rädler, K.-H. 1968, Z.Naturforschg. 23a, 1851
Rädler, K.-H. 1969a, Mber. Dt. Akad. Wiss 11, 194
Rädler, K.-H. 1969b, Geod. Geophys. Veröffentlichungen Reihe II Heft 13, 131
Rädler, K.-H. 1976, In V. Bumba and J. Kleczek, *Basic Mechanisms of Solar Activity*, D. Reidel Publishing Company Dordrecht, pp. 323–344
Rädler, K.-H., Rheinhardt, M., Apstein, E., & Fuchs, H., Magnetohydrodynamics 38, 39, 2002a
Rädler, K.-H., Rheinhardt, M., Apstein, E., & Fuchs, H., Nonlinear Processes in Geophysics 9, 171, 2002b
Rädler, K.-H., Kleeorin, N., & Rogachevskii, I. 2003, Geophys. Astrophys. Fluid Dyn., 97, 249
Rädler, K.-H., Brandenburg, A., Del Sordo, F., & Rheinhardt, M., submitted to PRE, arXiv.1104.1613
Roberts, P. H., & Soward, A. M. 1975, Astron. Nachr., 296, 49
Rogachevskii, I., Kleeorin, N., Brandenburg, A., & Eichler, D.: 2011, in preparation
Rüdiger, G. & Brandenburg, A. 1995, A&A, 296, 557
Schrinner, M., Rädler, K.-H., Schmitt, D., Rheinhardt, M., Christensen, U. 2005, Astron. Nachr., 326, 245
Schrinner, M., Rädler, K.-H., Schmitt, D., Rheinhardt, M., Christensen, U. R. 2007, Geophys. Astrophys. Fluid Dyn., 101, 81
Steenbeck, M., Krause, F., & Rädler, K.-H. 1966, Z. Naturforsch., 21a, 369
Sur, S., Brandenburg, A., & Subramanian, K. 2008, MNRAS, 385, L15
Vitense, E. 1953, Z. Astrophys., 32, 135

$Header: /var/cvs/brandenb/tex/koen/rotstrat/paper.tex,v 1.125 2011-

IV

A model of driven and decaying magnetic turbulence in a cylinder

Koen Kemel,[1,2] Axel Brandenburg,[1,2] and Hantao Ji[3]

[1]*NORDITA, AlbaNova University Center, Roslagstullsbacken 23, SE-10691 Stockholm, Sweden*
[2]*Department of Astronomy, Stockholm University, SE 10691 Stockholm, Sweden*
[3]*Center for Magnetic Self-Organization in Laboratory and Astrophysical Plasmas, Princeton Plasma Physics Laboratory, Princeton University, Princeton, New Jersey 08543, USA*

(Dated: June 7, 2011, Revision: 1.59)

Using mean-field theory, we compute the evolution of the magnetic field in a cylinder with outer perfectly conducting boundaries, an imposed axial magnetic and electric field. The thus injected magnetic helicity in the system can be redistributed by magnetic helicity fluxes down the gradient of the local current helicity of the small-scale magnetic field. A weak reversal of the axial magnetic field is found to be a consequence of the magnetic helicity flux in the system. Such fluxes are known to alleviate so-called catastrophic quenching of the α effect in astrophysical applications. Application to the reversed field pinch in plasma confinement devices is discussed.

PACS numbers: 52.55.Lf, 52.55.Wq, 52.65.Kj, 96.60.qd

I. INTRODUCTION

The interaction between a conducting medium moving at speed $\boldsymbol{U}$ through a magnetic field $\boldsymbol{B}$ is generally referred to as a dynamo effect. This effect plays important roles in astrophysics [1, 2], magnetospheric physics [3], as well as laboratory plasma physics [4]. It modifies the electric field in the rest frame, so that Ohm's law takes the form $\boldsymbol{J} = \sigma\left(\boldsymbol{E}+\boldsymbol{U}\times\boldsymbol{B}\right)$, where $\boldsymbol{J}$ is the current density, $\boldsymbol{E}$ is the electric field, and σ is the conductivity. Of particular interest for the present paper is the case where an external electric field $\boldsymbol{E}^{\rm ext}$ is induced through a transformer with a time-varying magnetic field, as is the case in many plasma confinement experiments. With the external electric field included, Ohm's law becomes

$$\boldsymbol{J} = \sigma\left(\boldsymbol{E}+\boldsymbol{E}^{\rm ext}+\boldsymbol{U}\times\boldsymbol{B}\right). \tag{1}$$

In a turbulent medium, often only averaged quantities (indicated below by overbars) are accessible. The averaged form of Ohm's law reads

$$\overline{\boldsymbol{J}} = \sigma\left(\overline{\boldsymbol{E}}+\overline{\boldsymbol{E}}^{\rm ext}+\overline{\boldsymbol{U}}\times\overline{\boldsymbol{B}}+\overline{\boldsymbol{\mathcal{E}}}\right), \tag{2}$$

where $\overline{\boldsymbol{\mathcal{E}}} = \overline{\boldsymbol{u}\times\boldsymbol{b}}$ is referred to as the mean $\overline{\boldsymbol{\mathcal{E}}} = \overline{\boldsymbol{u}\times\boldsymbol{b}}$ is referred to as the mean turbulent electromotive force, and $\boldsymbol{u} = \boldsymbol{U}-\overline{\boldsymbol{U}}$ and $\boldsymbol{b} = \boldsymbol{B}-\overline{\boldsymbol{B}}$ are fluctuations of velocity and magnetic field, respectively. It has been known for some time that the averaged profiles, $\overline{\boldsymbol{J}}$ and $\sigma\overline{\boldsymbol{E}}^{\rm ext}$ do not agree in actual experiments. This disagreement cannot be explained by the $\overline{\boldsymbol{U}}\times\overline{\boldsymbol{B}}$ term either, leaving therefore $\overline{\boldsymbol{\mathcal{E}}}$ as the only remaining term. Examples include the recent dynamo experiment in Cadarache [5] and in particular the reversed field pinch (RFP) [4, 6, 7], which is one of the configurations studied in connection with fusion plasmas. The name of this device derives from the fact that the toroidal (or axial, in a cylindrical geometry) magnetic field reverses sign near the periphery. Indeed, in the astrophysical context it is well-known that the $\overline{\boldsymbol{\mathcal{E}}}$ is responsible for the amplification and maintenance of large-scale magnetic fields [1, 2].

The analogy among the various examples of the $\overline{\boldsymbol{\mathcal{E}}}$ term has motivated comparative research between astrophysics and plasma physics applications [8]. In these cases, $\overline{\boldsymbol{\mathcal{E}}}$ is found to have a component proportional to the mean field ($\alpha\overline{\boldsymbol{B}}$, referred to as the α effect) and a component proportional to the mean current density ($\eta_{\rm t}\overline{\boldsymbol{J}}$, where $\eta_{\rm t}$ is the turbulent diffusivity). Since α is a pseudoscalar, one expects it to depend on the helicity of the flow, which is also a pseudoscalar. Decisive in developing the analogy between the α effects in astrophysics and laboratory plasma physics is the realization that α is caused not only by helicity in the flow (kinetic α effect), but also by that of the magnetic field itself [9]. This magnetic contribution to the α effect has received increased astrophysical interest, because there are strong indications that such dynamos saturate by building up small-scale helical fields that lead to a magnetic α effect which, in turn, counteracts the kinetic α effect [10–12]. This process can be described quantitatively by taking magnetic helicity evolution into account, which leads to what is known as the dynamical quenching formalism that goes back to early work of Kleeorin & Ruzmaikin [13]. However, it is now also believed that such quenching would lead to a catastrophically low saturation field strength [14], unless there are magnetic helicity fluxes out of the domain that would limit the excessive build-up of small-scale helical fields [15]. This would reduce the magnetic α effect and thus allow the production of mean fields whose energy density is comparable to that of the kinetic energy of the turbulence [16].

These recent developments are purely theoretical, so the hope is that more can be learnt by applying the recently gained knowledge to experiments like the RFP [6, 7]. Unlike tokamaks, the RFP is a relatively slender torus, so it makes sense to study its properties in a local model where one ignores curvature effects and considers a cylindrical piece of the torus. Along the axis of this cylinder there is a field-aligned current that makes the field helical. This field is susceptible to kink and tearing instabilities that lead to turbulence. It is generally believed that the resulting mean turbulent electromotive force $\overline{\boldsymbol{\mathcal{E}}}$ is responsible for the field reversal [4, 17]. The turbulence is also believed to help driving the system toward a minimum

energy state [18]. This state is nearly force-free and maintained by $\overline{\boldsymbol{E}}^{\rm ext}$. This adds to the notion that the RFP must be sustained by some kind of dynamo process [19]. In Cartesian geometry such a slow-down has previously already been modeled using the dynamical quenching formalism [20].

The RFP has been studied extensively using three-dimensional simulations [19, 21–23], which confirm the conjecture of J. B. Taylor [18] that the system approaches a minimum energy state. Additional understanding has been obtained using mean-field considerations [24, 25]. Both, here and in astrophysical dynamos there is an α effect that quantifies the correlation of the fluctuating parts of velocity and magnetic field. However, a major difference lies in the fact that in the RFP the α effect is caused by instabilities of the initially large-scale magnetic field while in the astrophysical case one is concerned with the problem of explaining the origin of large-scale fields by the α effect [1, 2]. However, this distinction may be too simplistic and there is indeed evidence that in the RFP the α effect exists in close relation with a finite magnetic helicity flux [26], supporting the idea that so-called catastrophic quenching is avoided by helicity transport.

The purpose of this paper is to apply modern mean-field dynamo theory with dynamical quenching to a cylindrical configuration to allow a more meaningful comparison between the α effect in astrophysics and the one occurring in RFP experiments.

II. THE MODEL

To model the evolution of the magnetic field in a cylinder with imposed axial magnetic and electric fields, we employ mean-field theory, where the evolution of the mean field $\overline{\boldsymbol{B}}$ is governed by turbulent magnetic diffusivity and an α effect. Unlike the astrophysical case where α depends primarily on the kinetic helicity of the plasma, in turbulence from current-driven instabilities the α effect is likely to depend primarily on the current helicity of the small-scale field [9]. The current density is given by $\boldsymbol{J}=\boldsymbol{\nabla}\times\boldsymbol{B}/\mu_0$, where μ_0 is the vacuum permeability and $\boldsymbol{j}=\boldsymbol{\nabla}\times\boldsymbol{b}/\mu_0$ is the fluctuating current density. The mean current helicity density of the small-scale field is then given by $\overline{\boldsymbol{j}\cdot\boldsymbol{b}}$. To a good approximation, the $\overline{\boldsymbol{j}\cdot\boldsymbol{b}}$ term is proportional to the small-scale magnetic helicity density, $\overline{\boldsymbol{a}\cdot\boldsymbol{b}}$, where $\boldsymbol{a}=\boldsymbol{A}-\overline{\boldsymbol{A}}$ is the vector potential of the fluctuating field. The generation of $\overline{\boldsymbol{a}\cdot\boldsymbol{b}}$ is coupled to the decay of $\overline{\boldsymbol{A}}\cdot\overline{\boldsymbol{B}}$ through the magnetic helicity evolution equation [10, 11, 13, 27] such that $\overline{\boldsymbol{A}}\cdot\overline{\boldsymbol{B}}+\overline{\boldsymbol{a}\cdot\boldsymbol{b}}$ evolves only resistively in the absence of magnetic helicity fluxes.

Note that $\overline{\boldsymbol{a}\cdot\boldsymbol{b}}$ is in general gauge-dependent and might therefore not be a physically meaningful quantity. However, if there is sufficient scale separation, the mean magnetic helicity density of the fluctuating field can be expressed in terms of the density of field line linkages, which does not involve the magnetic vector potential and is therefore gauge-independent [28]. For the large-scale field, on the other hand, the magnetic helicity density does remain in general gauge-dependent [29], but our final model will not be affected by this, because the magnetic helicity of the large-scale magnetic field does not enter in the mean-field model.

We model an induced electric field by an externally applied electric field $\boldsymbol{E}^{\rm ext}$. In the absence of any other induction effects this leads to a current density $\boldsymbol{J}=\sigma\boldsymbol{E}^{\rm ext}$. Furthermore, we ignore a mean flow ($\overline{\boldsymbol{U}}=\boldsymbol{0}$), and assume that the velocity field has only a turbulent component $\boldsymbol{u}$. For simplicity we assume that $\overline{\boldsymbol{E}}^{\rm ext}$ has no fluctuating part, i.e. $\boldsymbol{E}^{\rm ext}=\overline{\boldsymbol{E}}^{\rm ext}$. The decay of $\overline{\boldsymbol{B}}$ is accelerated by turbulent magnetic diffusivity $\eta_{\rm t}$, which is expected to occur as a result of the turbulence connected with kink and tearing instabilities inherent to the RFP. This mean turbulent electromotive force has two components corresponding to the α effect and turbulent diffusion with

$$\overline{\boldsymbol{\mathcal{E}}}=\alpha\overline{\boldsymbol{B}}-\eta_{\rm t}\mu_0\overline{\boldsymbol{J}}, \tag{3}$$

where we have ignored the fact that α effect and turbulent diffusion are really tensors. The evolution equation for $\overline{\boldsymbol{B}}$ is then given by the mean-field induction equation,

$$\frac{\partial\overline{\boldsymbol{B}}}{\partial t}=\boldsymbol{\nabla}\times\left(\alpha\overline{\boldsymbol{B}}-\eta_{\rm T}\mu_0\overline{\boldsymbol{J}}+\overline{\boldsymbol{E}}^{\rm ext}\right), \tag{4}$$

where $\eta_{\rm T}=\eta_{\rm t}+\eta$ is the sum of turbulent and microscopic (Spitzer) magnetic diffusivities (not to be confused with the resistivity $\eta\mu_0$, which is also often called η). Note that only non-uniform and non-potential contributions to $\overline{\boldsymbol{E}}^{\rm ext}$ can have an effect.

As a starting point, we assume that the rms velocity $u_{\rm rms}$ and the typical wavenumber $k_{\rm f}$ of the turbulence are constant, although it is clear that these values should really depend on the level of the actual magnetic field. We estimate the value of $\eta_{\rm t}$ using a standard formula for isotropic turbulence,

$$\eta_{\rm t}=\tfrac{1}{3}\tau\overline{\boldsymbol{u}^2}, \tag{5}$$

where $\tau=(u_{\rm rms}k_{\rm f})^{-1}$ is the correlation time of the turbulence and $u_{\rm rms}=(\overline{\boldsymbol{u}^2})^{1/2}$ is its rms velocity. Thus, we can also write $\eta_{\rm t}=u_{\rm rms}/3k_{\rm f}$. The turbulent velocity results from kink and tearing mode instabilities and will simply be treated as a constant in our model. For the α effect we assume that the kinetic helicity is negligible It would be much smaller than the current helicity, but of the same sign [9], so it would contribute to quenching the α effect, and so we just take

$$\alpha=\tfrac{1}{3}\tau\overline{\boldsymbol{j}\cdot\boldsymbol{b}}/\rho_0, \tag{6}$$

and use the fact that $\overline{\boldsymbol{j}\cdot\boldsymbol{b}}$ and $\overline{\boldsymbol{a}\cdot\boldsymbol{b}}$ are proportional to each other. Here, ρ_0 is the mean density of the plasma. For homogeneous turbulence we have $\overline{\boldsymbol{j}\cdot\boldsymbol{b}}=k_{\rm f}^2\overline{\boldsymbol{a}\cdot\boldsymbol{b}}/\mu_0$, although for inhomogeneous turbulence, $k_{\rm f}^2\overline{\boldsymbol{a}\cdot\boldsymbol{b}}/\mu_0$ has been found to be smaller than $\overline{\boldsymbol{j}\cdot\boldsymbol{b}}$ by a factor of two [30]. We compute the evolution of $\overline{\boldsymbol{a}\cdot\boldsymbol{b}}$ by considering first the evolution equation for $\overline{\boldsymbol{A}\cdot\boldsymbol{B}}$. Note that $\overline{\boldsymbol{A}\cdot\boldsymbol{B}}$ evolves only resistively, unless there is material motion through the domain boundaries [29], so we have

$$\frac{\rm d}{{\rm d}t}\overline{\boldsymbol{A}\cdot\boldsymbol{B}}=2\overline{\boldsymbol{E}}^{\rm ext}\cdot\overline{\boldsymbol{B}}-2\eta\mu_0\overline{\boldsymbol{J}\cdot\boldsymbol{B}}-\boldsymbol{\nabla}\cdot\overline{\boldsymbol{\mathcal{F}}}, \tag{7}$$

where $\overline{\boldsymbol{\mathcal{F}}}$ is the mean magnetic helicity flux. While $\overline{\boldsymbol{B}}$ evolves subject to the mean field equation (4), the magnetic helicity of the mean field will change subject to the equation

$$\frac{\mathrm{d}}{\mathrm{d}t}\left(\overline{\boldsymbol{A}}\cdot\overline{\boldsymbol{B}}\right)=2\overline{\boldsymbol{\mathcal{E}}}^{\mathrm{tot}}\cdot\overline{\boldsymbol{B}}-2\eta\mu_0\overline{\boldsymbol{J}}\cdot\overline{\boldsymbol{B}}-\boldsymbol{\nabla}\cdot\overline{\boldsymbol{\mathcal{F}}}_{\mathrm{m}}, \tag{8}$$

where $\overline{\boldsymbol{\mathcal{E}}}^{\mathrm{tot}}=\overline{\boldsymbol{\mathcal{E}}}+\overline{\boldsymbol{E}}^{\mathrm{ext}}$ and $\overline{\boldsymbol{\mathcal{F}}}_{\mathrm{m}}=\overline{\boldsymbol{E}}\times\overline{\boldsymbol{A}}+\overline{\Phi}\,\overline{\boldsymbol{B}}$ is the mean magnetic helicity flux from the mean magnetic field, and $\overline{\Phi}$ is the mean electrostatic potential. Here, $\overline{\boldsymbol{E}}=\eta\mu_0\overline{\boldsymbol{J}}-\overline{\boldsymbol{\mathcal{E}}}^{\mathrm{tot}}$ is the mean electric field. Subtracting (8) from (7), we find a similar evolution equation for $\overline{\boldsymbol{a}\cdot\boldsymbol{b}}$,

$$\frac{\mathrm{d}}{\mathrm{d}t}\overline{\boldsymbol{a}\cdot\boldsymbol{b}}=-2\overline{\boldsymbol{\mathcal{E}}}\cdot\overline{\boldsymbol{B}}-2\eta\mu_0\overline{\boldsymbol{j}\cdot\boldsymbol{b}}-\boldsymbol{\nabla}\cdot\overline{\boldsymbol{\mathcal{F}}}_{\mathrm{f}}, \tag{9}$$

where $\overline{\boldsymbol{\mathcal{F}}}_{\mathrm{f}}=\overline{\boldsymbol{\mathcal{F}}}-\overline{\boldsymbol{\mathcal{F}}}_{\mathrm{m}}$ is the mean magnetic helicity flux from the fluctuating magnetic field. Note that $\boldsymbol{E}^{\mathrm{ext}}$ does not enter in Eq. (9), because $\boldsymbol{E}^{\mathrm{ext}}=\overline{\boldsymbol{E}}^{\mathrm{ext}}$ has no fluctuations. This equation can readily be formulated as an evolution equation for α by writing $\alpha=(\tau k_{\mathrm{f}}^2/3\rho_0\mu_0)\overline{\boldsymbol{a}\cdot\boldsymbol{b}}$, i.e.,

$$\frac{\partial\alpha}{\partial t}=-2\eta_{\mathrm{t}}k_{\mathrm{f}}^2\overline{\boldsymbol{\mathcal{E}}}\cdot\overline{\boldsymbol{B}}/B_{\mathrm{eq}}^2-2\eta k_{\mathrm{f}}^2\alpha-\boldsymbol{\nabla}\cdot\overline{\boldsymbol{\mathcal{F}}}_{\alpha}, \tag{10}$$

where $\overline{\boldsymbol{\mathcal{F}}}_{\alpha}=(\tau k_{\mathrm{f}}^2/3\rho_0\mu_0)\overline{\boldsymbol{\mathcal{F}}}_{\mathrm{f}}$, which is a rescaled magnetic helicity flux of the small-scale field and B_{eq} is the field strength for which magnetic and kinetic energy densities are equal, i.e.,

$$B_{\mathrm{eq}}^2=\mu_0\rho_0u_{\mathrm{rms}}^2=(3\rho_0\mu_0/\tau)\,\eta_{\mathrm{t}}. \tag{11}$$

We recall that in the astrophysical context, equation (10) is referred to as the dynamical quenching model [13, 27]. In a first set of models we assume $\overline{\boldsymbol{\mathcal{F}}}_{\alpha}=\boldsymbol{0}$, but later we shall allow for the fluxes to obey a Fickian diffusion law,

$$\overline{\boldsymbol{\mathcal{F}}}_{\alpha}=-\kappa_{\alpha}\boldsymbol{\nabla}\alpha, \tag{12}$$

where κ_{α} is a diffusion coefficient that is known to be comparable to or somewhat below the value of η_{t} [29, 30].

We solve the governing one-dimensional equations (4) and (10) using the PENCIL CODE in cylindrical coordinates, (r,ϕ,z), assuming axisymmetry and homogeneity along the z direction, $\partial/\partial\phi=\partial/\partial z=0$, in a one-dimensional domain $0\leq r\leq R$. On $r=0$ regularity of all functions is obeyed, while on $r=R$ we assume perfect conductor boundary conditions, which implies that $\hat{\boldsymbol{n}}\times\overline{\boldsymbol{E}}=\hat{\boldsymbol{n}}\times\overline{\boldsymbol{J}}=\boldsymbol{0}$, and thus $\hat{\boldsymbol{n}}\times\partial\overline{\boldsymbol{A}}/\partial t=\boldsymbol{0}$, i.e., $\hat{\boldsymbol{n}}\times\overline{\boldsymbol{A}}=\mathrm{const}$.

As initial condition, we choose a uniform magnetic field B_0 in the z direction. In terms of the vector potential, this implies

$$\boldsymbol{A}(r,0)=(0,B_0r/2,0) \tag{13}$$

for the initial value of $\boldsymbol{A}(r,t)$.

We drive the system though the externally applied mean electromotive force in the z direction. We choose

$$\overline{E}_z^{\mathrm{ext}}(r)=\overline{E}_0^{\mathrm{ext}}J_0(k_1r), \tag{14}$$

where $\overline{E}_0^{\mathrm{ext}}$ is the value of the mean electromotive force on the axis and $k_1R\approx2.4048256$ is the rescaled cylindrical wavenumber for which $\overline{E}_z^{\mathrm{ext}}(R)=0$, which corresponds to the first zero of the Bessel function of order zero, and thus satisfies the perfect conductor boundary condition on $r=R$. An important control parameter of our model is the nondimensional ratio

$$\mathcal{Q}=\overline{E}_0^{\mathrm{ext}}/\eta_{\mathrm{t}}k_{\mathrm{f}}B_0, \tag{15}$$

which determines the degree of magnetic helicity injection. Other control parameters include the normalized strength of the imposed field,

$$\mathcal{B}=B_0/B_{\mathrm{eq}} \tag{16}$$

and the value of Lundquist number,

$$\mathcal{L}=v_{\mathrm{A}}/\eta k_{\mathrm{f}}, \tag{17}$$

which is a nondimensional measure of the inverse microscopic magnetic diffusivity, where $v_{\mathrm{A}}=B_0/\sqrt{\mu_0\rho_0}$ is the Alfvén speed associated with the imposed field. The Lundquist number also characterizes the ratio of turbulent to microscopic magnetic diffusivity, i.e.,

$$\mathcal{R}\equiv\eta_{\mathrm{t}}/\eta=u_{\mathrm{rms}}/3\eta k_{\mathrm{f}}=\mathcal{L}/3\mathcal{B}, \tag{18}$$

which we refer to as the magnetic Reynolds number. Note that, if we were to define the magnetic Reynolds number as $R_{\mathrm{m}}=u_{\mathrm{rms}}/\eta k_{\mathrm{f}}$, as is often done, then $\mathcal{R}=R_{\mathrm{m}}/3$ would be three times smaller. Finally, the wavenumber of the energy-carrying turbulent eddies is expressed in terms of the dimensionless value of $k_{\mathrm{f}}R$. We treat k_{f} here as an adjustable parameter that characterizes the degree of scale separation, i.e., the ratio of the scale of the domain to the characteristic scale of the turbulence. In most of the cases we consider $k_{\mathrm{f}}R=10$. In summary, our model is characterized by four parameters: $\mathcal{Q}$, $\mathcal{B}$, $\mathcal{L}$, and $k_{\mathrm{f}}R$. In models with magnetic helicity flux we also have the parameter $\kappa_{\alpha}/\eta_{\mathrm{t}}$.

In addition to plotting the resulting profiles of magnetic field and current density, we also determine mean-field magnetic energy and helicity, as well as mean-field current helicity, i.e.,

$$M_{\mathrm{m}}=\langle\overline{\boldsymbol{B}}^2/2\mu_0\rangle,\quad H_{\mathrm{m}}=\langle\overline{\boldsymbol{A}}\cdot\overline{\boldsymbol{B}}\rangle,\quad C_{\mathrm{m}}=\langle\overline{\boldsymbol{J}}\cdot\overline{\boldsymbol{B}}\rangle, \tag{19}$$

where $\langle.\rangle=\int_0^R.\,r\,\mathrm{d}r/(\frac{1}{2}R^2)$ denotes a volume average and the subscript m refers to mean-field quantities. Following similar practice of earlier work [11, 31], we characterize the solutions further by computing the effective wavenumber of the mean field, k_{m}, and the degree ϵ_{m} to which it is helical, via

$$k_{\mathrm{m}}^2=\mu_0C_{\mathrm{m}}/H_{\mathrm{m}},\quad \epsilon_{\mathrm{m}}=C_{\mathrm{m}}/2k_{\mathrm{m}}M_{\mathrm{m}}. \tag{20}$$

In the following we shall refer to ϵ_{m} as the relative magnetic helicity. We recall that, even though $\overline{\boldsymbol{A}}\cdot\overline{\boldsymbol{B}}$ is gauge-dependent, for perfect conductor boundary conditions, the integral $\int\overline{\boldsymbol{A}}\cdot\overline{\boldsymbol{B}}\,\mathrm{d}V$ is gauge-invariant, and so is then k_{m}. Similar definitions also apply to the fluctuating field, whose current helicity is given by

$$C_{\mathrm{f}}=\langle\alpha\rangle B_{\mathrm{eq}}^2/\mu_0\eta_{\mathrm{t}}. \tag{21}$$

The magnetic helicity of the fluctuating field is then $H_{\rm f} = \mu_0 C_{\rm f}/k_{\rm f}^2$. The magnetic energy of the fluctuating field can be estimated under the assumption that the field is fully helical, i.e., $\langle \boldsymbol{b}^2 \rangle = k_{\rm f} |\langle \boldsymbol{a} \cdot \boldsymbol{b} \rangle|$, so that $M_{\rm f} = |C_{\rm f}|/2k_{\rm f}$. We study both the steady state case where $\mathcal{Q}$ and $\mathcal{B}$ are non-vanishing, and the decaying case where $\mathcal{Q} = \mathcal{B} = 0$. In the latter case, we monitor the decay rates of the magnetic field.

III. RESULTS

A. Driven field-aligned currents

We begin by considering the case without magnetic helicity fluxes and take $\mathcal{B} = 1$, $\mathcal{L} = 1000$ (corresponding to $\mathcal{R} = 333$) and $k_{\rm f} R = 10$. The resulting values of $k_{\rm m}$ and $\epsilon_{\rm m}$ are given in Table I and the mean magnetic field profiles are compared in Fig. 1 for different values of $\mathcal{Q}$. It turns out that, as we increase the value of $\mathcal{Q}$, the magnetic helicity of the mean field increases, i.e. the product $\epsilon_{\rm m} k_{\rm m}$ increases, but the *relative* helicity of the mean magnetic field decreases slightly, i.e., $\epsilon_{\rm m}$ decreases. The value of $k_{\rm m}$ increases with $\mathcal{Q}$, which means that the mean field will be confined to a progressively thinner core around the axis. Furthermore, the anti-correlation between $\epsilon_{\rm m}$ and $k_{\rm m}$ is also found when varying $\mathcal{B}$ (see Table II), $\mathcal{L}$, or $\mathcal{R}$. This is demonstrated in Fig. 2, where we show that $\epsilon_{\rm m}$ is in fact proportional to $(k_{\rm m}/k_1)^{-1/4}$ and that the product $\epsilon_{\rm m}(k_{\rm m}/k_1)^{1/4}$ is approximately constant, even though $\mathcal{Q}$, $\mathcal{B}$, or $\mathcal{L}$ are varied. This scaling is unexpected and there is currently no theoretical interpretation for this behavior.

It is interesting to note that $k_{\rm m}$ does not vary significantly with $\mathcal{B}$, provided $\mathcal{R}$ is held fixed. However, for weak fields, e.g., for $\mathcal{B} = 0.1$, the dynamics of the mean field is no longer controlled by magnetic helicity evolution, and the value of $k_{\rm m} R$ has then dropped suddenly by nearly a factor of 2, and $\epsilon_{\rm m}$ is in that case no longer anti-correlated with $k_{\rm m}$. This data point falls outside the plot range of Fig. 2, and is therefore not included. Also, if only $\mathcal{L}$ is held fixed, so that $\mathcal{R}$ varies with $\mathcal{B}$, then $k_{\rm m}$ is no longer weakly varying with $\mathcal{B}$, and varies more strongly in that case.

TABLE I: $\mathcal{Q}$ dependence of $k_{\rm m}$ and $\epsilon_{\rm m}$ for $\mathcal{B} = 1$, $\mathcal{L} = 1000$, and $k_{\rm f} R = 10$.

$\mathcal{Q}$	0.01	0.03	0.10	0.20	0.50	1.00
$k_{\rm m} R$	2.76	3.44	4.63	5.26	6.49	7.20
$\epsilon_{\rm m}$	0.95	0.91	0.84	0.82	0.78	0.73

TABLE II: $\mathcal{B}$ dependence of $k_{\rm m}$ and $\epsilon_{\rm m}$ for $\mathcal{Q} = 0.1$, $\mathcal{R} = 100$, and $k_{\rm f} R = 10$.

$\mathcal{B}$	0.1	0.2	0.5	1	2	5	10
$k_{\rm m} R$	1.80	3.33	3.50	3.99	3.42	3.31	3.25
$\epsilon_{\rm m}$	0.51	0.91	0.89	0.84	0.89	0.89	0.89

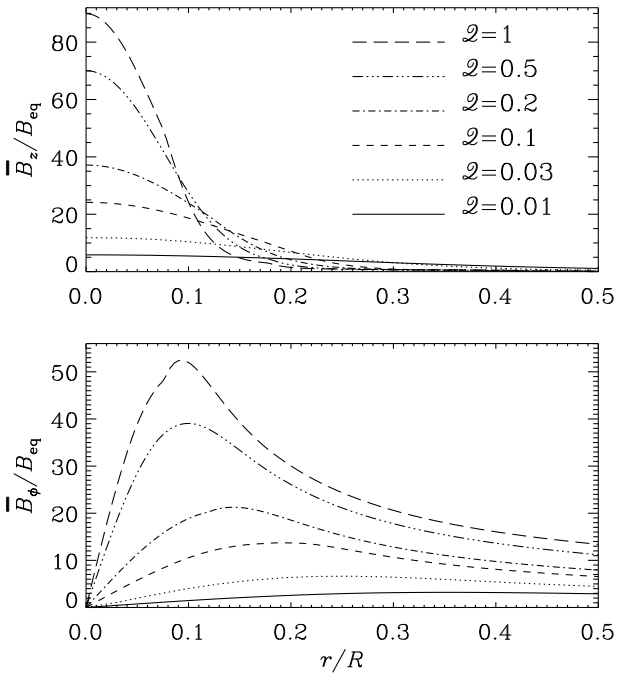

FIG. 1: Equilibrium profiles for three different driving strengths for $\mathcal{B} = 1$, $\mathcal{L} = 1000$, and $k_{\rm f} R = 10$.

We must ask ourselves why the axial field component does not show a reversal in radius, as is the case in the RFP. Experimental studies of the RFP provide direct evidence for a reversal. By comparing radial profiles of the axial current, $\overline{J}_\parallel/\sigma$, with those of the axial electric field, $\overline{E}_\parallel$, one concludes that the mismatch between the two must come from the $\overline{\mathcal{E}}_\parallel$ term [17, 32]. These studies show that $\overline{E}_\parallel < \overline{J}_\parallel/\sigma$ near the axis and $\overline{E}_\parallel > \overline{J}_\parallel/\sigma$ away from it (assuming $\overline{B}_\parallel > 0$ on the axis). Comparing with Eq. (2), it is therefore clear that $\overline{\mathcal{E}}_\parallel$ must then be negative near the axis and positive near the outer rim. Turning now to dynamo theory, it should be emphasized that there are two contributions to $\overline{\mathcal{E}}_\parallel$, one from $\alpha \overline{\boldsymbol{B}}$ and one from $-\eta_{\rm t} \mu_0 \overline{\boldsymbol{J}}$; see Eq. (3). Let us therefore discuss in the following the expected sign of $\overline{\mathcal{E}}_\parallel$. Given that $\mathcal{Q}$ is positive, $\overline{\boldsymbol{J}} \cdot \overline{\boldsymbol{B}}$ must also be positive, and therefore we expect α to be positive. If the mean magnetic field was really sustained by a dynamo, the α term would dominate over the $\eta_{\rm t}$ term, but this is likely not the case here. Indeed, by manipulating Eq. (10) we see that, in the steady state without magnetic helicity fluxes, the equation for α takes the form

$$\alpha = \frac{\mathcal{R} \eta_{\rm t} \mu_0 \overline{\boldsymbol{J}} \cdot \overline{\boldsymbol{B}} / B_{\rm eq}^2}{1 + \mathcal{R} \overline{\boldsymbol{B}}^2 / B_{\rm eq}^2}; \tag{22}$$

see, e.g., Ref. [11]. However, as alluded to above, the relevant term entering $\overline{\boldsymbol{\mathcal{E}}}$ is the combination $\alpha_{\rm red} = \alpha - \eta_{\rm t} \mu_0 \overline{\boldsymbol{J}} \cdot \overline{\boldsymbol{B}} / \overline{\boldsymbol{B}}^2$,

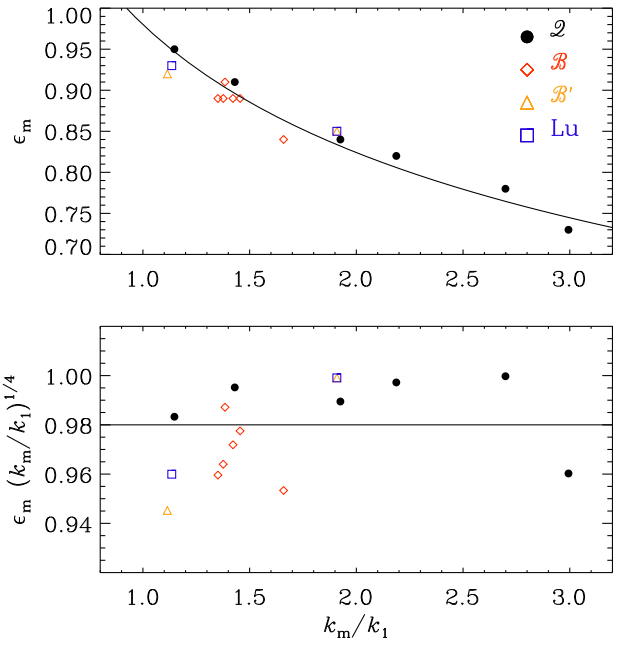

FIG. 2: (Color online) Dependence of ϵ_m on k_m for different sets of runs where either $\mathcal{Q}$ is varied (filled symbols), $\mathcal{B}$ is varied while keeping $\mathcal{R} = 100$ (red diamonds), $\mathcal{B}$ is varied while keeping $\mathcal{L} = 100$ (orange triangles), or $\mathcal{L}$ is varied (blue squares).

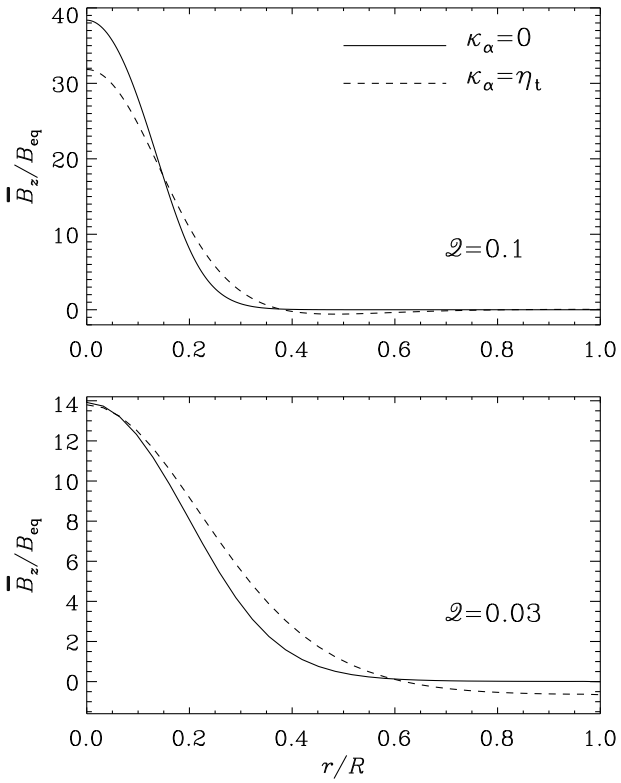

FIG. 3: Effect of magnetic helicity flux on equilibrium profiles of $\overline{B}_z$ for $\mathcal{Q} = 0.1$ (upper panel) and $\mathcal{Q} = 0.03$ (lower panel). Note the field reversal at the outer rim in the latter case.

which is the reduced α. Inserting Eq. (22) yields

$$\alpha_{\rm red} = -\frac{\eta_t \mu_0 \overline{\boldsymbol{J}} \cdot \overline{\boldsymbol{B}} / \overline{\boldsymbol{B}}^2}{1 + \mathcal{R} \overline{\boldsymbol{B}}^2 / B_{\rm eq}^2}, \tag{23}$$

with a minus sign in front. The important point here is that $\alpha_{\rm red}$ is indeed negative if $\overline{\boldsymbol{J}} \cdot \overline{\boldsymbol{B}}$ is positive. This means that we can only expect $\overline{E}_\parallel < \overline{J}_\parallel/\sigma$, which is the situation in the RFP near the axis [32]. In order to reverse the ordering and to produce a reversal of the axial field, one would need to have an α effect that dominates over turbulent diffusion. Note also that for strong mean fields, $\alpha_{\rm red}$ is of the order of the microscopic magnetic diffusivity. (This situation is well-known for nonlinear dynamos, because there $\alpha_{\rm red}$ and the microscopic diffusion term ηk_m have to balance each other in a steady state [33].)

We note in passing that k_m enters neither in Eq. (22) nor in Eq. (23). However, k_m does enter if there is a magnetic helicity flux and it affects the time-dependent case, as is also clear from Eq. (10). Both cases will be considered below.

B. Effect of magnetic helicity flux

Next, we study cases where a diffusive magnetic helicity flux is included. In our model with perfectly conducting boundaries, the magnetic helicity flux vanishes on the boundaries, so no magnetic helicity is exported from the domain, but the divergence of the flux is finite and can thus modify the magnetic α effect. The same is true of periodic boundaries, where no magnetic helicity is exported, but the flux divergence is finite and can alleviate catastrophic quenching in dynamos driven by the kinetic α effect [34].

In Fig. 3 we compare profiles of $\overline{B}_z$ with and without magnetic helicity flux. It turns out that the κ_α term has the effect of smoothing out the resulting profile of $\overline{B}_z$. More interestingly, it can lead to a reversal of $\overline{B}_z$ at intermediate radii. For our reference run with $\mathcal{Q} = 0.1$ (upper panel), the reversal is virtually absent at the rim of the cylinder. This is mainly because the pinch is so narrow; see Table III. However, when decreasing $\mathcal{Q}$ to 0.03, there is a clear reversal also at the outer rim (lower panel). However, decreasing $\mathcal{Q}$ to 0.01 does not increase the extent of the reversal. In none of these cases the field reversal is connected with a change of sign of $\alpha_{\rm red}$. Instead, $\alpha_{\rm red}$ is always found to be negative, even in the presence of a magnetic helicity flux. Thus, the sign reversal of $\overline{B}_z$ is therefore associated with a sign reversal of $\overline{J}_z$ at the same radius. Nevertheless, the reversal is still not very strong with $\min(\overline{B}_z)/\max(\overline{B}_z) \approx -0.07$, while in laboratory RFPs this ratio is typically -0.2 [32].

C. Decay calculations

Next, we consider the case of a decaying magnetic field in the absence of an external electric field. In that case all components of $\overline{\boldsymbol{B}}$ must eventually decay to zero. The evolution of the magnetic energy of the resulting mean and fluctuating fields is shown in Fig. 4, together with the evolution of $k_{\rm m}$ and $\epsilon_{\rm m}$. At early times, when $\langle\overline{\boldsymbol{B}}^2\rangle \gg B_{\rm eq}^2$, the energy of the large-scale magnetic field decays at the resistive rate $\lambda = -2\eta k_{\rm m}^2$. During that time, the energy of the small-scale field stays approximately constant: the magnetically generated α effect almost exactly balances turbulent diffusion and the magnetic field can only decay at the resistive rate. However, at later times, when $\langle\overline{\boldsymbol{B}}^2\rangle \ll B_{\rm eq}^2$, the energy of the small-scale field decays with a negative growth rate $\lambda = -2\eta k_{\rm f}^2$, which then speeds up the decay of the energy of the large-scale magnetic field to a rate that is about $1.3\times\eta_{\rm t}k_{\rm m}^2$, where we have used the value $k_{\rm m}R = 3.1$ that is relevant for the late-time decay. This value is also that obeying Taylor's [18] postulated minimum energy state. Again, no reversal of the magnetic field is found, except in cases where there is an internal magnetic helicity flux in the system.

IV. CONCLUSIONS

The present work is an application of the dynamical quenching model of modern mean-field dynamo theory to magnetically driven and decaying turbulence in cylindrical geometry. In the driven case, an external electric field is applied, which leads to magnetic helicity injection at large scales. Such a situation has not yet been considered in the framework of mean-field theory. It turns out that in such a case there is a weak anti-correlation between the actual value of magnetic helicity of the mean field, $\epsilon_{\rm m}k_{\rm m}$, and the relative magnetic helicity $\epsilon_{\rm m}$ with $\epsilon_{\rm m}\sim k_{\rm m}^{-1/4}$. This weak anti-correlation is found to be independent of whether $\mathcal{Q}$, $\mathcal{B}$, or $\mathcal{L}$ are varied. No theoretical interpretation of this behavior has yet been offered. In the decaying case, we find that the decay rate is close to the resistive value when the field is strong, i.e., $\overline{B} > B_{\rm eq}$, and drops to the turbulent resistive value when the mean field becomes weaker. This behavior has also been found in earlier calculation of the decay of helical magnetic fields in Cartesian geometry [20].

The original anticipation was that our model reproduces some features of the RFP that is studied in connection with fusion plasma confinement. It turns out that the expected field reversal that gives the RFP its name is found to require the presence of magnetic helicity fluxes. Without such fluxes, there is no reversal; see Fig. 3. Nevertheless, the reversal is rather weak compared with laboratory RFPs. This discrepancy can have several reasons. On the one hand, we have been working here with a model that has previously only been tested under simplifying circumstances in which there is turbulent dynamo action driven by kinetic helicity supply. It is therefore possible that the model has shortcomings that have not yet been fully understood. A related possibility is that the model is still basically valid, but our application to the RFP has been too crude. For example, the assumption of fixed values of $\eta_{\rm t}$ and $B_{\rm eq}$ is certainly quite simplistic. On the other hand, it is not clear that this simplification would really affect

TABLE III: Values of $k_{\rm m}$ and $\epsilon_{\rm m}$ with and without magnetic helicity flux.

$\mathcal{Q}$	0.03		0.1	
$\kappa_\alpha/\eta_{\rm t}$	0	1	0	1
$k_{\rm m}R$	4.63	4.50	3.51	3.32
$\epsilon_{\rm m}$	0.84	0.83	0.91	0.92

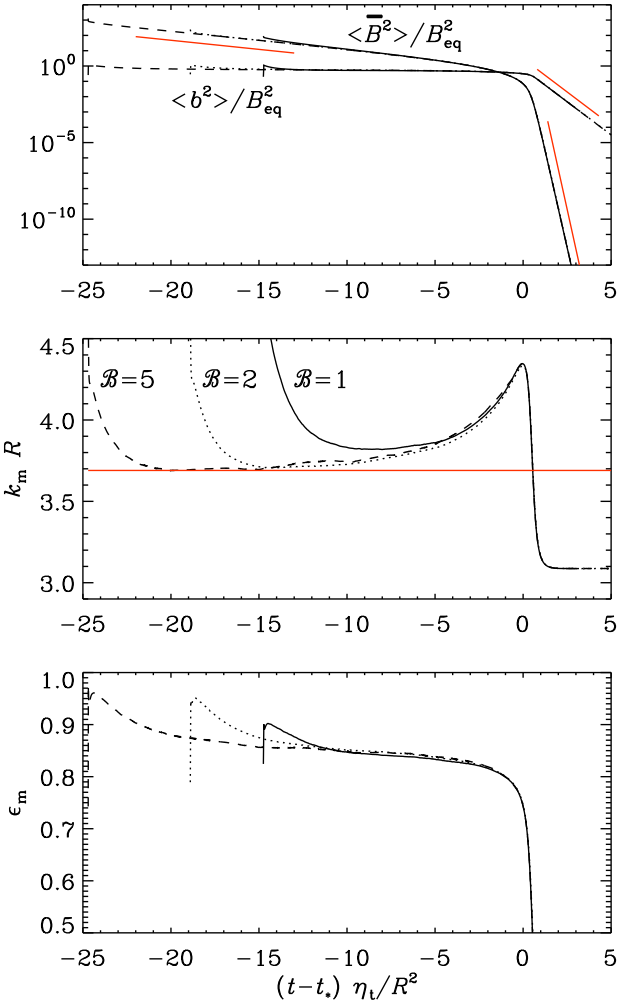

FIG. 4: (Color online) Evolution of $\langle\overline{\boldsymbol{B}}^2\rangle/B_{\rm eq}^2$, $k_{\rm m}/k_1$, and $\epsilon_{\rm m}$ for different values of $\mathcal{B}$. Note that time is shifted by t_*, which is the time when $k_{\rm m}$ attains its second maximum. In the top panel, the red lines indicate resistive decay rate of the large-scale field at early times, resistive decay rate of the small-scale field at late times, and the turbulent decay rate of the large-scale field at late times.

the outcome of the model in any decisive way. A different possibility is that the application of an external electric field is not representative of the RFP. However, an important basic idea behind the present setup has been to establish a model as simple as possible, that could be tested by performing corresponding three-dimensional simulations of a similar setup. This has not yet been attempted, but this would clearly constitute a natural next step to take.

Acknowledgments

This work was supported in part by the Swedish Research Council, grant 621-2007-4064, the European Research Council under the AstroDyn Research Project 227952, and the National Science Foundation under Grant No. NSF PHY05-51164. HJ acknowledges support from the U.S. Department of Energy's Office of Science – Fusion Energy Sciences Program.

[1] H. K. Moffatt, *Magnetic field generation in electrically conducting fluids*. Cambridge University Press, Cambridge (1978).
[2] F. Krause and K.-H. Rädler, *Mean-field magnetohydrodynamics and dynamo theory*. Pergamon Press, Oxford (1980).
[3] T. Ogino, J. Geophys. Res. **91**, 6791 (1986).
[4] H. Ji, S. C. Prager, A. F. Almagri, J. S. Sarff, and H. Toyama, Phys. Plasmas **3**, 1935 (1996).
[5] R. Monchaux, M. Berhanu, M. Bourgoin, et al., Phys. Rev. Lett. **98**, 044502 (2007).
[6] H. A. B. Bodin and A. A. Newton, Nuclear Fusion **20**, 1255 (1980).
[7] J. B. Taylor, Phys. Rev. Lett. **58**, 741 (1986).
[8] E. G. Blackman and H. Ji, Mon. Not. R. Astron. Soc. **369**, 1837 (2006).
[9] A. Pouquet, U. Frisch, and J. Léorat, J. Fluid Mech. **77**, 321 (1976).
[10] G. B. Field and E. G. Blackman, Astrophys. J. **572**, 685 (2002).
[11] E. G. Blackman and A. Brandenburg, Astrophys. J. **579**, 359 (2002).
[12] K. Subramanian, Bull. Astr. Soc. India **30**, 715 (2002).
[13] N. I. Kleeorin and A. A. Ruzmaikin, Magnetohydrodynamics **18**, 116 (1982).
[14] A. Brandenburg and K. Subramanian, Astron. Nachr. **326**, 400 (2005).
[15] A. Brandenburg and C. Sandin, Astron. Astrophys. **427**, 13 (2004).
[16] A. Brandenburg, Astrophys. J. **625**, 539 (2005).
[17] H. Ji and S. C. Prager, Magnetohydrodynamics **38**, 191 (2002). astro-ph/0110352
[18] J. B. Taylor, Phys. Rev. Lett. **33**, 1139 (1974).
[19] A. Y. Aydemir and D. C. Barnes, Phys. Rev. Lett. **52**, 930 (1984).
[20] T. A. Yousef, A. Brandenburg, and G. Rüdiger, Astron. Astrophys. **411**, 321 (2003).
[21] D. D. Schnack, E. J. Caramana, and R. A. Nebel, Phys. Fluids **28**, 321 (1985).
[22] H.-E. Sätherblom, S. Mazur, and P. Nordlund, Plasmas Phys. Contr. Fusion **38**, 2205 (1996).
[23] S. Cappello, D. Bonfiglio, and D. F. Escande, Phys. Plasmas **13**, 056102 (2006).
[24] H. R. Strauss, Phys. Fluids **28**, 2786 (1985).
[25] A. Bhattacharjee and E. Hameiri, Phys. Rev. Lett. **57**, 206 (1986).
[26] H. Ji, Phys. Rev. Lett. **83**, 3198 (1999).
[27] N. Kleeorin, I. Rogachevskii, and A. Ruzmaikin, Astron. Astrophys. **297**, 159 (1995).
[28] K. Subramanian and A. Brandenburg, Astrophys. J. **648**, L71 (2006).
[29] A. Hubbard and A. Brandenburg, Geophys. Astrophys. Fluid Dynam. **104**, 577 (2010).
[30] D. Mitra, S. Candelaresi, P. Chatterjee, R. Tavakol, and A. Brandenburg, Astron. Nachr. **331**, 130 (2010).
[31] A. Brandenburg, W. Dobler, and K. Subramanian, Astron. Nachr. **323**, 99 (2002).
[32] Y. L. Ho, S. C. Prager, D. D.Schnack, Phys. Rev. Lett. **62**, 1504 (1989).
[33] A. Brandenburg, K.-H. Rädler, M. Rheinhardt, and K. Subramanian, Astrophys. J. **676**, 740 (2008).
[34] A. Hubbard and A. Brandenburg, Astrophys. J. **727**, 11 (2011).